Modeling and Simulation of a Linear Motor System

by

Joseph Abraham

B.S., Mechanical Engineering, Cornell University, 1980
M.S., Mechanical Engineering, University of New Haven, 1989

Submitted to the Department of Mechanical Engineering
in Partial Fulfillment of the Requirements for the Degree of

Master of Science in Mechanical Engineering

at the

Massachusetts Institute of Technology

June 1997

Signature of Author .....
Department of Mechanical Engineering
May 9, 1997

Certified by .....
Kamal Youcef-Toumi
Associate Professor of Mechanical Engineering
Thesis Supervisor

Accepted by .....
Ain A. Sonin
Chairman, Department Committee on Graduate Students

Modeling and Simulation of a Linear Motor System

by

Joseph Abraham

Submitted to the Department of Mechanical Engineering
on May 9, 1997 in partial fulfillment of the requirements for the Degree of
Master of Science in Mechanical Engineering

ABSTRACT

The design of a model for a hybrid permanent magnet linear stepper motor is described. The bond graph method was used to analyze the motor system and extract the operative equations. First, a simulation which demonstrates the basic validity of the model without magnetic losses or non-linearities was run . Next, the magnetic loss mechanisms, eddy currents and hysteresis (including saturation non-linearity), are analyzed and modeled using theoretical and empirical methods. Models of simple ferromagnetic elements were validated against published data. Finally, the relevant losses were incorporated into the motor system model and a simulation of the system was executed. The simulation can be used to predict such system parameters as force output, power consumption, and system instability.

Thesis Supervisor: Kamal Youcef-Toumi

Title: Associate Professor of Mechanical Engineering

Acknowledgments

My sincere appreciation to all those who provided assistance and smiles through the years. I would like to express special gratitude and thanks to Jane and Carrie Abraham, Leslie Regan, Anne Schwartz, and Kamal Youcef-Toumi.

Contents

List of Figures

List of Tables

Chapter 1

Introduction

The development of an electrical motor system may use a variety of different methods to arrive at a system ready for prototype testing. Beginning with an existing design, the designer typically analyzes the performance and modifies the system to suit the intended application. This analysis can utilize testing, handbook calculations, linear modeling, finite element analysis, or other tools to help predict the effect of changing system parameters. Software modeling of the system can provide the designer a way to automate system simulation and the flexibility to vary parameters. A modeling method based on power flow provides an intuitive and useful way of representing an electrical motor system which converts power between electrical, magnetic, and mechanical domains. The *bond graph* technique [12] is such a method.

As an example of an electrical motor system, a linear motor (the Sawyer motor) is being evaluated for use in a flexible material handling application [33]. In this application, the motor is expected to perform at near peak performance through a wide variety of tasks. These include low and high speed operation, acceleration, braking, and holding, all with inertial loads ranging from relatively low to high. The preliminary design of the control system and the tailoring of the motor design can be aided by a computer model of the system. After a prototype is built, the computer model can be adjusted to match the real system and further improvements can be made.

The Sawyer linear stepper motor is considered a candidate for high speed material handling systems and industrial automation. As a one- or two-dimensional linear positioning motor, the Sawyer motor has the incremental motion characteristic of a stepper motor and is suitable for open loop computer control. It does not require rotary to linear motion conversion by mechanisms such as lead screws. Configuration of a two dimensional X-Y system is relatively simple. The Sawyer motor is capable of high speeds and combines the flexibility of direct drive positioning capability with long life and low maintenance requirements. These attributes allow the use of one system to serve in multiple applications (flexible automation) without major physical re-design. In order to maximize the performance of these systems, the motor can be run in a closed loop mode with a combination of position, velocity, or acceleration feedback.

For design and optimization purposes it is desirable to accurately model the dynamic characteristics of the motor system. To date, models of the system have not accurately incorporated ferromagnetic behavior. In this project, the electromagnetic-mechanical system is modeled using energy-based bond graph techniques. A detailed model of the nonlinear and hysteretic behavior of ferromagnetic materials is developed. A computer dynamic simulation is run to test the model against known motor behavior. Design parameters such as flux path and material properties can be changed and the effect on motor performance simulated.

Chapter two describes a basic model of the Sawyer linear motor which is derived from the bond graph representation. This model simplifies the loss mechanisms and non-linear effects. Basic motor behavior is predicted.

In Chapter three details the modeling of a ferromagnetic element including non-linear magnetic behavior (saturation and hysteresis) and eddy current losses. This element model is verified against published loss data.

Chapter four adds the detailed ferromagnetic element to the motor model of Chapter two. The model demonstrates the capability to predict magnetic losses and motor behavior with a non-linear time domain model.

1.1 Description of the Sawyer motor

The Sawyer motor is classified as a linear (versus rotary) machine of the hybrid stepping motor type. As a stepping motor, it may also function as a synchronous reluctance machine. The literature [15, 16, 29, 30] describes the Sawyer motor, so only a brief overview is presented here.

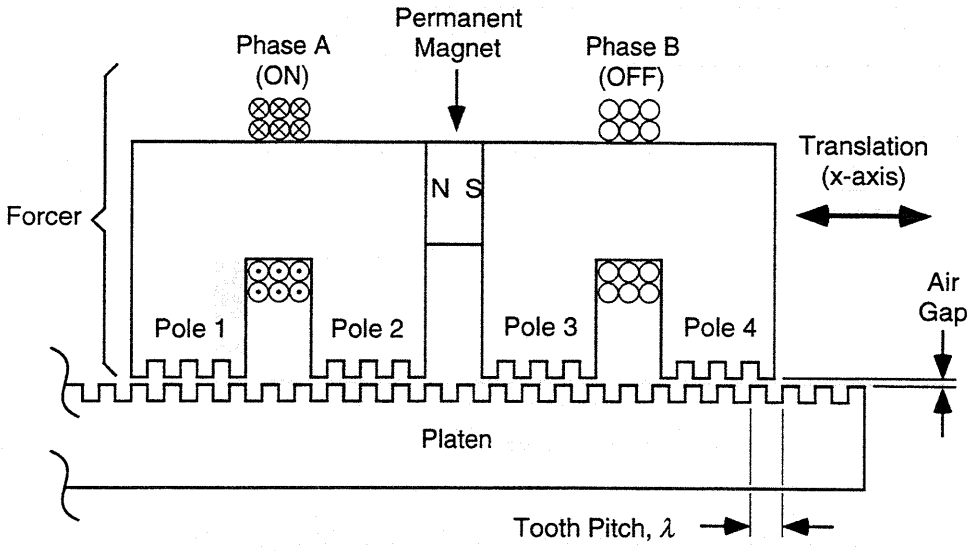

Figure 1.1. Sawyer linear motor, single forcer. Cardinal state corresponding to phase A energized with polarity shown and phase B de-energized.
(Air gap shown larger than scale for clarity)

One form of the Sawyer linear motor is shown in Figure 1.1. The moving part of the motor (the armature) is called a "forcer". The fixed part, the stator, is a simple toothed rail called a "platen". A fixed spacing is maintained between the forcer and platen by a low friction bearing. This bearing can be a rolling element bearing or an air bearing. The air gap clearance between the two parts is typically 15 μm. The platen can be as long as necessary for the required motion. The teeth on the platen are spaced at a pitch of λ, typically about 1 millimeter. The forcer has four poles, each pole also has a toothed structure with a pitch of λ. The teeth on each pole, however, are spaced in quadrature to the teeth on the other poles so that only one pole can be aligned (at minimum reluctance) with the platen teeth at any one time.

The forcer is wound with two coils, labeled phase A and phase B. These phases are separated by a rare earth permanent magnet. When a phase is energized, the coil field aids the permanent magnet field at one pole and opposes it at the other. This action results in a cancellation of the magnetic field at one pole and a reinforcement at another. No current in a winding allows approximately equal fields at the poles on that winding. By appropriately phasing the currents to the two phases, a selected single pole will attempt to align its teeth with the platen teeth. This establishes one of the four "cardinal states" identified by one pole in alignment with the platen teeth.

In Figure 1.1, the phase A winding is energized so as to aid the permanent magnet flux at pole 1 and cancel the permanent magnet at pole 2. Since the phase B winding is not energized, poles 3 and 4 are at roughly the same relative mmf as the south pole of the magnet. These poles serve as the return path for the flux from pole 1. Thus, pole 1 will try to align with the platen teeth, pole 2 will have no effect, and the forces due to flux through poles 3 and 4 will cancel. This stable situation corresponds to one of the four possible cardinal states.

By appropriate sequencing of the winding currents through phases for each of the cardinal states, the motor will move left or right by steps of $\lambda/4$. This mode of operation is called "single stepping". By proportioning currents to the two phases ("microstepping"), the forcer can assume positions between the cardinal states. Continuous synchronous motion occurs if appropriately phased sine currents are applied to each winding.

Although the motor establishes a stable equilibrium at the commanded position, this is only relative to the platen teeth. If sufficient force is applied to the motor, it may slip to another position an integer number of tooth pitches away from the desired position. This will also occur if the forcer is translating and acceleration or force beyond its capacity is attempted. When the motor is pulled out of synchronous position this way, the motor is said to have stalled and its "pull-out force" has been reached. Pull-out force as a function of velocity is a convenient way to specify motor force output. It is measured by setting a motor at specific stepping rate or velocity, and gradually increasing load force until it slips out of synchronous motion.

Two other considerations are pertinent in the modeling this motor. First, the Sawyer motor must carry umbilical connections to its power source. At the same time, consideration must be given to supply of pressurized air for the air bearing and forcer cooling, when needed. These connections limit the range of motion of the forcer. They also impose additional inertial loads, so the load carried by the motor is increased by these connections. Second, there is very little mechanical damping in this type of motor with an air bearing. The air gap dimension may spontaneously oscillate with certain values of bearing air pressure or when the motor is driven at certain velocities. Thus, a critical function of the electromagnetic system is to provide adequate damping to assure stable operation. Interaction of the air bearing with the translation of the motor system was not considered in this study.

1.2 Approach to modeling the Sawyer hybrid linear motor system

The motor system includes the motor, its electric drive power source, and the external loads imposed. The approach followed here is to start with a simple model and gradually add complexity leading to more physically realistic system models.

Initially, following on work previously done [1], a simple model of a Sawyer motor is developed and demonstrated. The bond graph technique [12] is used to develop the model. The model assumes an ideal power source, and that all magnetic elements are linear. Specifically, a perfect current source drives the motor, and the non-linearities (saturation, hysteresis) of the ferromagnetic materials are ignored. All of the losses are lumped into an empirical mechanical damping term. The model leads to a set of state equations defining the system dynamics.

The equations are evaluated using the SIMULINK® [19] dynamic modeling program. Physical parameters of the motor are based on a commercially available product, the Parker Compumotor model L20. Using the advertised characteristics of the L20 motor allows the model to be evaluated for realistic behavior. A summary of L20 motor parameters is shown in Appendix A. The linear model simulation is fast, stable and gives reasonable motor simulation results without detailed loss partitioning.

The next level of detail addresses the power source. An amplifier model with limited output voltage and frequency response is added to the system model. The amplifier has a voltage output which regulates current by means of simple feedback control. The change in the amplifier model forces additional states in the motor model because of a change in causality. The revised equations are simulated and the results are compared with those obtained on the initial model.

Next, the non-linear magnetic effects and losses judged most important are modeled. Detailed time domain models of eddy current effects and hysteresis are produced and validated against published and measured data. The saturation response of ferromagnetic materials is modeled in conjunction with the model for hysteresis. All of these characteristics are assembled in a SIMULINK® program for a detailed ferromagnetic element simulation. The total "iron losses" are measured during the simulation and compare favorably with published test data.

Finally, the ferromagnetic element model is combined with the motor system model. Additional refinements to the original system model including amplifier current limiting and indirect solution of initial flux conditions are incorporated. The modeled motor system is generally reasonable when compared to the published performance. Losses calculated by the simulation are similar to those predicted by traditional methods.

Chapter 2

Analysis with linear magnetic elements

For the initial modeling attempt, state equations will be developed for the motor shown in Figure 1.1. The model will omit the non-linear elements of magnetic energy storage. Only the air gaps between the forcer poles and the platen will be considered. This model will serve as the baseline for comparison as more complex component descriptions are added. A simple model also provides a easily simulated system for fast analysis and motor performance evaluation. The assumptions made to simplify the analysis are discussed first.

2.1 Assumptions

As a first approximation, the permeability of the flux path in the iron will be assumed high such that the only significant reluctance is in the air gaps and in the permanent magnet. This assumption removes the most significant non-linearity, the ferromagnetic material. Saturation and hysteresis are therefore neglected. For low flux densities and low loss materials, this may be a reasonable assumption. The next chapter will investigate these effects further.

A simple flux path, which neglects flux leakage around the pole gaps is assumed. The reluctance at each pole is assumed to vary sinusoidally between a maximum and minimum value as the motor translates. This is approximately correct and permits simplified numerical analysis. A discussion of the assumed reluctance function can be found in Appendix B.

The permanent magnet is assumed to operate with constant reluctance. That is, the flux versus magneto-motive force relationship is assumed linear. This is not unreasonable for rare earth magnets which have a very linear operating curve or "recoil line", even in the presence of large demagnetizing fields [6]. The NdFeB (Neodymium-Iron-Boron) permanent magnets used in the physical motor specimen fits this assumption very closely. Figure 2.1 shows a typical rare earth operating curve.

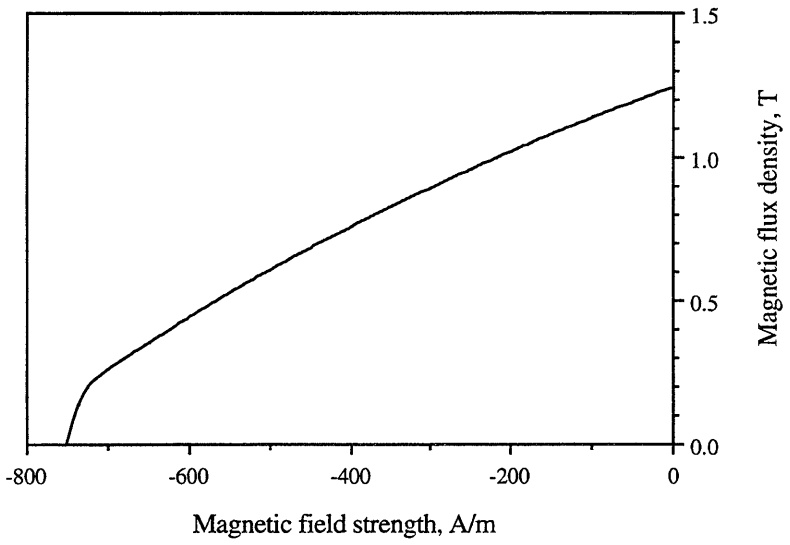

Figure 2.1. Typical NdFeB magnet "Demagnetization Curve" showing the flux density to magnetizing force relationship. Reference [6]

The coils are assumed to link all flux in the iron they are wrapped around. All coils are assumed active at all flux densities. Flux leakage is neglected.

The air bearing which supports the forcer away from the platen is actually a dynamically complex system of its own. Although the gap between the motor poles and the platen has a very significant effect on the performance of the motor, the gap is assumed constant. This assumption is approximately valid, as the air bearings which support the motor are extremely stiff.

Dynamic conditions are observed to occur where there is interaction between the translation axis, x and the support axis, y. The air bearing is a pneumatic system with resonances which can be excited by variation in the magnetic attraction between the platen and the forcer. Careful control of the air pressure to the bearings can minimize the chance of the two systems interacting. These effects are not considered here, but could be important in some applications.

It is initially assumed that the motor drive circuit, which is a PWM (pulse width modulated) motor-current controlled amplifier, can be modeled as an ideal current source. This should be a reasonable assumption for low frequencies and low coil excitation, up to the voltage limit of the amplifiers. To simulate higher frequencies and drive currents, the model will be improved by changing it to a voltage driven system, with current feedback to an amplifier modeled with a transfer function. The Parker Compumotor amplifiers, which can be used to drive the L20 motor, have a 2500 Hz bandwidth and a 170 volt peak output. In an earlier work [30], the amplifiers driving the motor were characterized by a transfer function. In theory, an amplifier system could be designed to provide performance levels as required to achieve the level of current control desired.

2.2 Bond graph development

Reference [12] describes a general approach to developing a dynamic model of an electromagnetic-mechanical system using bond graphs. This approach will be used here on the two phase single forcer depicted in Figure 1.1.

For modeling the magnetic path, the flux path in the forcer and the coil and permanent magnet fields determine the junction structure. The bond graph convention of -0- and -1- junctions is determined by conservation of power. Power is the product of effort and flow. If the common variable is effort, the junction is a -0- type. If the common variable is flow, the junction is a -1- type. In a magnetic circuit the effort variable is magneto-motive force, $M = \int \mathbf{H} \cdot d\mathbf{l}$. The flow variable is flux rate, $d\phi/dt$. Magnetic flux, ϕ, (despite its name) is the *displacement* variable, not the flow variable.

Generally, the procedure for developing a bond graph requires the use of the flow variable to properly define the junction structure. However, in the case of magnetic variables it will be shown that it is correct to use the conservation of *either* flux or flux rate when developing the bond graph structure. The following explanation shows how this is a consequence of Gauss's law. Electrical and mechanical systems do not have an exact analog of Gauss's law, and the initial conditions must be treated more generally.

Consider the case of a -1- junction, where the flow is common to i connected elements,

$$\dot{\phi}_1 = \dot{\phi}_2 = \dot{\phi}_3 \ldots = \dot{\phi}_i .$$

Integrating over time,

$$\int_{t_0}^{\tau} \dot{\phi}_i dt = \int_{\phi_i(0)}^{\phi_i(\tau)} d\phi_i = \phi_i(\tau) - \phi_i(0),$$

and

$$\phi_1(\tau) - \phi_1(0) = \phi_2(\tau) - \phi_2(0) \ldots = \phi_i(\tau) - \phi_i(0).$$

The fluxes at any time are only equal if and only if the initial fluxes are equal.

By Gauss's Law, $\nabla \cdot \mathbf{B} = 0$. Therefore, all flux lines must be closed and the net magnetic *flux* must be identically zero through any closed volume (including magnetic paths described by -1- or -0- junctions). This is true initially and also at all times, τ. Thus, for a -1- junction the initial fluxes are equal and

$$\phi_1 = \phi_2 = \phi_3 \ldots = \phi_i .$$

For a -0- junction,

$$\sum_i \dot{\phi}_i = 0,$$

and since the sum of the initial fluxes must be zero by Gauss's Law,

$$\sum_i \phi_i = 0.$$

Thus, the flux may be used interchangeably with the flux rate in the constitutive equations for the magnetic -0- and -1- junctions. Note that in the case of electrical (charge) or mechanical (position) displacements, the initial net displacement is not necessarily zero. There may be a non-zero constant of integration which will be present at all times, although the net flow must be conserved.

(Note that flux ϕ will be used interchangeably with flux rate $d\phi/dt$ in the bond graph figures that follow. As explained above, it is understood that either one applies.)

In deriving a model for the motor, the air gap reluctances which represent the storage of magnetic potential energy are represented as three-port capacitances. The energy stored is a function of the flux at the pole, ϕ and the gap reluctance, R. The gap reluctance is determined by gap geometry for a fixed pole shape by the gap height, y and the motor position, x. Using the bond graph notation, the gap capacitance is represented as

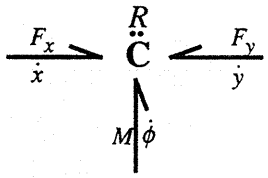

The constitutive equation of the capacitance,

$$E(x, y, \phi) = \frac{R(x, y)}{2}\phi^2,$$

expresses the stored energy as a function of the three gap displacements, x, y, and ϕ. For this analysis, the gap height, y is assumed fixed, so the above equation reduces to two variables

$$E(x,\phi) = \frac{R(x)}{2}\phi^2.$$

Motor windings A and B are seen as gyrators with modulus N, the number of turns. The winding resistance is in series with the current (flow) source. In this case, the flux through winding A all passes through the gap at pole 1.

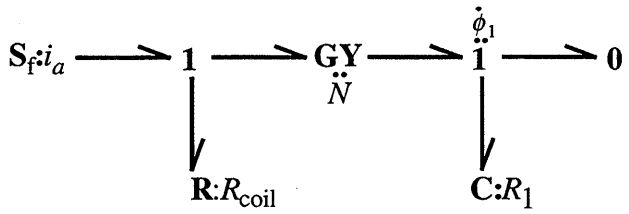

Similarly, the flux in pole 4 equals the flux in coil B.

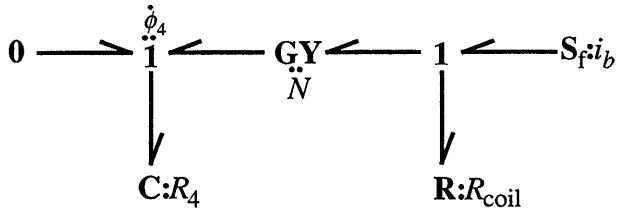

The permanent magnet flux is determined by the magnet apparent reluctance, the zero flux ("open circuit") mmf and the applied external magneto-motive forces. Referring to Figure 2.1, the zero flux mmf of the magnet is approximately equal to its coercive field strength (H_c) times the magnet length (l_m). The magnet apparent reluctance (R_m) is the slope of the mmf versus flux curve. This slope is approximately the ratio of the zero flux mmf ($H_c l_m$) to the zero mmf flux ($B_r A_m$), where B_r is the remanent flux density and A_m is the magnet cross section area. The permanent magnet behavior can thus be represented on the bond graph as a series combination of an effort (mmf) source and a capacitance (reluctance). The electrical analogous construction is the case of a battery in series with a capacitor.

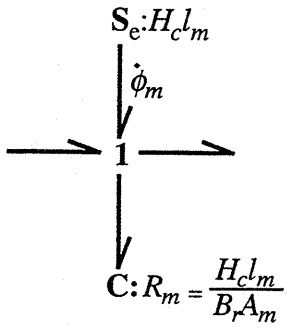

It is worth noting that this idealized linear representation is energetically consistent. The magnet can provide no net power as in the analogous case of a battery in series with a capacitor. The effort source (mmf) merely serves to establish a steady state displacement (flux) as in the electrical analogy the effort source (emf) serves to establish a steady state displacement (charge). The traditional resistance-reluctance analogy fails to produce this result.

The mmf at pole 2 is the same as the mmf at the north end of the permanent magnet. At pole 3 the mmf is the same as at the south end of the magnet. The flux through these poles is equal to the difference between the flux from the magnet and the flux from the associated coil.

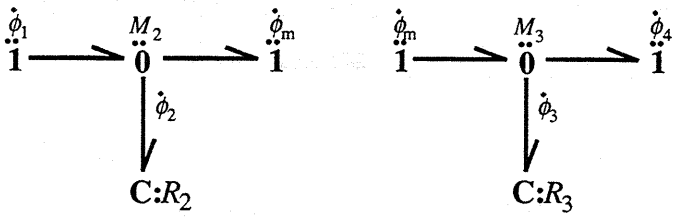

Since the mechanical ports of the capacitances have a common velocity, they are linked together at a -1- junction to the mass, m of the forcer. The major losses associated with this motor include air resistance (windage), hysteresis and eddy currents. It is well-known [4, 6] that eddy current and hysteresis losses increase with speed (frequency). As a first order approximation, these are lumped together with the air resistance as mechanical losses directly proportional to velocity. Therefore, a resistance r, representing a viscous-type loss proportional to forcer velocity, is added to complete the x-axis bond graph segment.

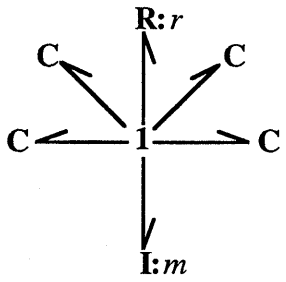

Causality is assigned to the bond graph based on the assumption of current source inputs. The completely assembled and augmented bond graph is shown in Figure 2.2. An external mechanical force, F_{ext} has been added to represent an external load.

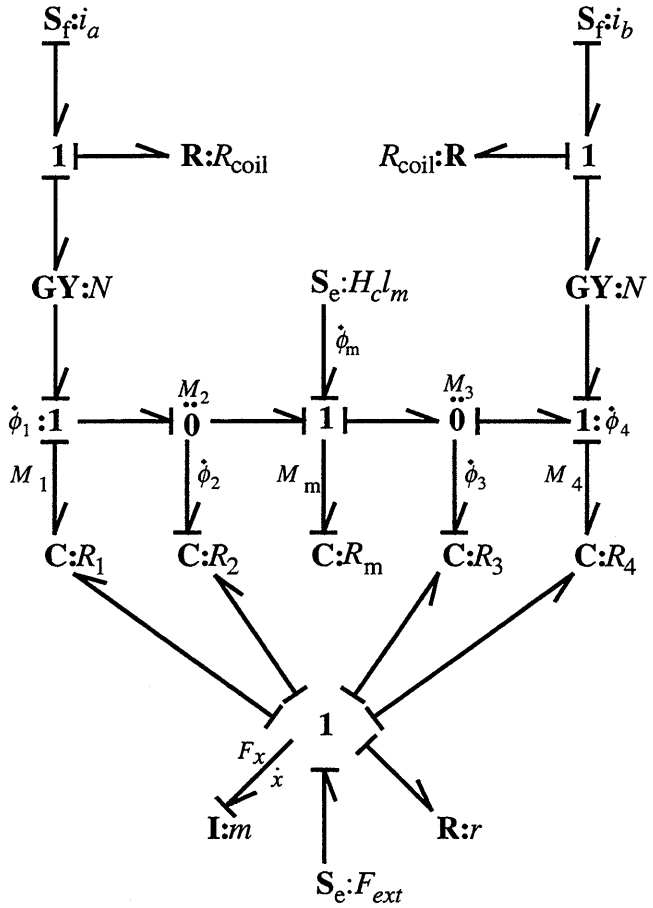

Figure 2.2. *X*-axis bond graph for a simplified Sawyer motor model.

2.3 Derivation of state equations

Working from the bond graph of Figure 2.2, first the possible state variables are identified. State variables may be produced only by elements in integral causality. For this analysis, the so-called "energy variables" are selected. The energy variables are the displacements associated with capacitances and the momenta associated with inertial elements. They are

ϕ_1, ϕ_4	magnetic flux in poles 1 and 4,
x	tangential forcer displacement, and
p	tangential forcer momentum.

The inputs are motor winding excitation currents i_a and i_b.

The junction structure yields

$$\dot{\phi}_1 = \dot{\phi}_m + \dot{\phi}_2, \tag{2.1}$$

$$\dot{\phi}_4 = \dot{\phi}_m - \dot{\phi}_3, \tag{2.2}$$

$$M_2 = Ni_a - M_1, \tag{2.3}$$

$$M_3 = M_4 - Ni_b, \tag{2.4}$$

$$M_m = M_2 + H_c l_m - M_3, \tag{2.5}$$

where M are mmf and N is the number of turns in the windings.

The constitutive equations associated with the capacitive elements are derived from the energy equation. For a general potential energy function of k displacements

$$E = E(q_1, q_2 \ldots q_k),$$

there are k associated efforts

$$e_k = \frac{\partial E}{\partial q_k}.$$

Recall

$$E(x,\phi) = \frac{R(x)}{2}\phi^2.$$

Therefore,

$$M_1 = \frac{\partial E(x,\phi_1)}{\partial \phi_1} = R_1(x)\phi_1, \tag{2.6}$$

$$M_4 = \frac{\partial E(x,\phi_4)}{\partial \phi_4} = R_4(x)\phi_4, \tag{2.7}$$

and the force produced by the *i*th pole is

$$F_i = \frac{\partial E(x,\phi_i)}{\partial x} = \frac{1}{2}\phi_i^2 \frac{\partial R_i}{\partial x}.$$

The dependent variables (because they are in derivative causality) are

$$\phi_2 = \frac{M_2}{R_2(x)}, \tag{2.8}$$

$$\phi_3 = \frac{M_3}{R_3(x)}, \tag{2.9}$$

and

$$\phi_m = \frac{M_m}{R_m}, \tag{2.10}$$

where the magnet reluctance is

$$R_m = \frac{H_c l_m}{B_r A_m}.$$

The quantities $R_1 ... R_4$ are the gap reluctances further described in the next section.

At the mechanical -1- junction the forces from all of the magnetic poles are summed with the viscous drag force

$$-F_x + F_{ext} - r\dot{x} - \sum_{i=1}^{4} F_i = 0.$$

The total force on the mass is equal to the rate of change of momentum

$$F_x = \dot{p} = -\frac{1}{2}\sum_{i=1}^{4} \phi_i^2 \frac{\partial R_i}{\partial x} - r\dot{x} + F_{ext}, \tag{2.11}$$

where r is a damping coefficient corresponding to velocity proportional drag forces (an estimate of eddy current and windage losses). The constitutive relation for the mass yields the state equation

$$\dot{x} = \frac{p}{m}. \tag{2.12}$$

Equations (2.1) and (2.2) are directly integrated, as shown earlier, into

$$\phi_1 = \phi_m + \phi_2, \tag{2.13}$$

and

$$\phi_4 = \phi_m - \phi_3. \tag{2.14}$$

Starting with (2.13) and substituting (2.10) and (2.8), (2.5), (2.3) and (2.4), then (2.6) and (2.7) yields

$$\phi_1 = \frac{Ni_a - \phi_1 R_1 + H_c l_m + Ni_b - \phi_4 R_4}{R_m} + \frac{Ni_a - \phi_1 R_1}{R_2}. \tag{2.15}$$

Similarly, using (2.14) and substituting (2.10), (2.9), (2.5), (2.4), (2.6), (2.3) and (2.7) yields

$$\phi_4 = \frac{Ni_a - \phi_1 R_1 + H_c l_m + Ni_b - \phi_4 R_4}{R_m} + \frac{Ni_b - \phi_4 R_4}{R_3}. \tag{2.16}$$

Solving (2.15) and (2.16) for ϕ_1 and ϕ_4 explicitly, the results are

$$\phi_1 = \frac{(R_m + R_2)Ni_a + R_2 Ni_b + R_2 H_c l_m - R_2 R_4 \phi_4}{R_m R_2 + R_m R_1 + R_2 R_1}, \tag{2.17}$$

and

$$\phi_4 = \frac{(R_m + R_3)Ni_b + R_3 Ni_a + R_3 H_c l_m - R_1 R_3 \phi_1}{R_m R_3 + R_m R_4 + R_3 R_4}. \tag{2.18}$$

The flux at poles 2 and 3 are derived from equations (2.8), (2.9), (2.3), (2.4), (2.6), and (2.7) as

$$\phi_2 = \frac{Ni_a - \phi_1 R_1}{R_2}, \tag{2.19}$$

and

$$\phi_3 = \frac{\phi_4 R_4 - Ni_b}{R_3}. \tag{2.20}$$

These four equations are of the form

$$\begin{bmatrix}\phi_1\\ \phi_2\\ \phi_3\\ \phi_4\end{bmatrix} = \mathbf{A}\begin{bmatrix}\phi_1\\ \phi_2\\ \phi_3\\ \phi_4\end{bmatrix} + \mathbf{B}\begin{bmatrix}i_a\\ i_b\end{bmatrix} + \mathbf{C}, \tag{2.21}$$

where

$$\mathbf{A} = \begin{bmatrix} 0 & 0 & 0 & \dfrac{-R_2R_4}{R_mR_2 + R_mR_1 + R_2R_1} \\ \dfrac{-R_1}{R_2} & 0 & 0 & 0 \\ 0 & 0 & 0 & \dfrac{R_4}{R_3} \\ \dfrac{-R_1R_3}{R_mR_3 + R_mR_4 + R_3R_4} & 0 & 0 & 0 \end{bmatrix}, \tag{2.22}$$

$$\mathbf{B} = N\begin{bmatrix} \dfrac{R_m + R_2}{R_mR_2 + R_mR_1 + R_1R_2} & \dfrac{R_2}{R_mR_2 + R_mR_1 + R_1R_2} \\ R_2^{-1} & 0 \\ 0 & -R_3^{-1} \\ \dfrac{R_3}{R_mR_3 + R_mR_4 + R_3R_4} & \dfrac{R_m + R_3}{R_mR_3 + R_mR_4 + R_3R_4} \end{bmatrix}, \tag{2.23}$$

and

$$\mathbf{C} = H_c l_m \begin{bmatrix} \dfrac{R_2}{R_mR_2 + R_mR_1 + R_2R_1} \\ 0 \\ 0 \\ \dfrac{R_3}{R_mR_3 + R_mR_4 + R_3R_4} \end{bmatrix}. \tag{2.24}$$

Solving for the flux, (2.21) becomes

$$\Phi = [\mathbf{I} - \mathbf{A}]^{-1}(\mathbf{Bi} + \mathbf{C}), \tag{2.25}$$

where,

$$\Phi(\mathbf{i}, x) = \begin{bmatrix} \phi_1 \\ \phi_2 \\ \phi_3 \\ \phi_4 \end{bmatrix}, \quad \mathbf{i} = \begin{bmatrix} i_a \\ i_b \end{bmatrix}.$$

Note that the flux is only a function of the input currents, the permanent magnet, and the various gap reluctances which are functions of the motor position, x. Although magnetic flux represents a displacement, it does not add state variables to this system. How can this be? Review of the bond graph of Figure 2.2, reveals that the entire motor can be represented as a 4-port *implicit* capacitor field.

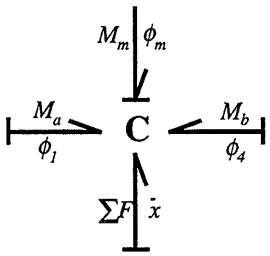

The magnetic inputs to this field are applied efforts (M=Ni). In the magnetic domain the capacitor is forced to be in derivative causality. The fluxes must therefore be dependent variables, and do not contribute a state variable.

The complete state equations are formed when (2.25) is combined with (2.11) and (2.12). Equation (2.11) can be restated as a matrix equation

$$\dot{p} = -\frac{1}{2}\Phi^T \frac{\partial}{\partial x}\mathbf{R}(x)\Phi - r\frac{p}{m} + F_{ext}, \tag{2.26}$$

and

$$\dot{x} = \frac{p}{m}, \tag{2.12}$$

where,

$$\mathbf{R}(x) = \begin{bmatrix} R_1 & 0 & 0 & 0 \\ 0 & R_2 & 0 & 0 \\ 0 & 0 & R_3 & 0 \\ 0 & 0 & 0 & R_4 \end{bmatrix}.$$

2.4 Evaluation of reluctance functions

As is clear from equation (2.26) the change in gap reluctance as the motor moves is essential to the production of useful force. As a practical matter, reluctance in an air gap of arbitrary geometry is only approximated. One reason is that the closed form evaluation of Maxwell's equations to define the magnetic field is, generally speaking, not possible to do. Finite element approximations can be calculated by computer and may be tabulated. For this analysis, the accuracy gained by use of numerical methods is unlikely to be significant when compared to the errors generated by the other simplifying assumptions (e.g. neglecting flux leakage and iron reluctance). A reluctance function was selected which is approximately correct, simple to compute, and adequate for evaluation of qualitative behavior.

Qualitative measurements of air gap reluctance variation as a motor pole moves across a platen are shown in Appendix B. A curve fitted to the data can be modeled as a cosine function

$$R = \tfrac{1}{2}(R_{\max} + R_{\min}) - \tfrac{1}{2}(R_{\max} - R_{\min})\cos\left(\frac{2\pi x}{\lambda} + \alpha\right), \tag{2.27}$$

where $R_{\max}$ and $R_{\min}$ are the calculated limits of the reluctance variation (see Appendix B), λ is the platen pitch, and α is the relative phase of the poles. If x=0 is fixed at a point on the platen, then the poles will have reluctance functions phase shifted 90° each. Thus,

$$R_1 = \tfrac{1}{2}(R_{\max} + R_{\min}) - \tfrac{1}{2}(R_{\max} - R_{\min})\cos\left(\frac{2\pi x}{\lambda}\right), \tag{2.28}$$

$$R_2 = \tfrac{1}{2}(R_{\max} + R_{\min}) + \tfrac{1}{2}(R_{\max} - R_{\min})\cos\left(\frac{2\pi x}{\lambda}\right), \tag{2.29}$$

$$R_3 = \tfrac{1}{2}(R_{\max} + R_{\min}) - \tfrac{1}{2}(R_{\max} - R_{\min})\sin\left(\frac{2\pi x}{\lambda}\right), \tag{2.30}$$

$$R_4 = \tfrac{1}{2}(R_{\max} + R_{\min}) + \tfrac{1}{2}(R_{\max} - R_{\min})\sin\left(\frac{2\pi x}{\lambda}\right). \tag{2.31}$$

2.5 Summary of the state equations

The state equations are non-linear and of the form

$$\dot{\mathbf{X}} = \mathbf{f}(\mathbf{X}, \mathbf{U}),$$

where $\mathbf{X}$ is the vector of state variables p and x and $\mathbf{U}$ is a vector of the input currents i_a and i_b. (Φ is a function of x, i_a and i_b; it does not add any independent state variables.)

The equations required to model the system with linear magnetic elements are

$$\dot{p} = -\frac{1}{2}\Phi^T \frac{\partial}{\partial x}\mathbf{R}(x)\Phi - r\frac{p}{m} + F_{ext}, \tag{2.26}$$

$$\dot{x} = \frac{p}{m}, \tag{2.12}$$

where,

$$\Phi = [\mathbf{I} - \mathbf{A}]^{-1}(\mathbf{Bi} + \mathbf{C}), \tag{2.25}$$

and:

A, **B**, **C**, and **R** are matrices of reluctance functions of x as defined above.

Matrix **i** is a vector of the input currents.

I is the identity matrix.

r is a coefficient of damping.

m is the mass of the moving system.

2.6 Simulation of the simplified motor model

Simulation of the model can be handled in many different ways, depending on the software available and the intended use of the model. In this project, the MATLAB® and SIMULINK® software packages from the Mathworks, Inc. were selected. The equations of the last section are readily encoded as a SIMULINK® block diagram. This system block diagram, which is a graphical representation of the mathematical model is shown in Figures 2.3a through 2.3e. Figure 2.3a shows the overall flow of the calculations. The inputs are velocity command and external force. The output labeled Yout is a flag which is set whenever the motor position slips out of synchronization. Internal states, such as position and velocity, are readily monitored. The overall control of the simulation is done by means of a MATLAB® program file called a "script". In this case, the script file will set the initial conditions, the simulation parameters, and the other conditions and constants specific to the problem at hand. The script file for this simulation is called '`smotl20.m`' and is shown in Appendix C.

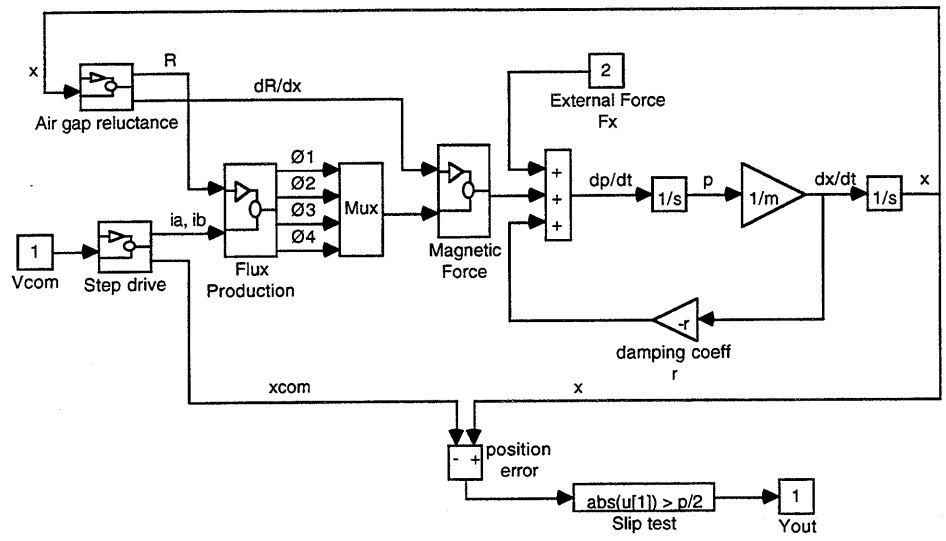

Figure 2.3a. SIMULINK® block diagram of the simplified motor model.

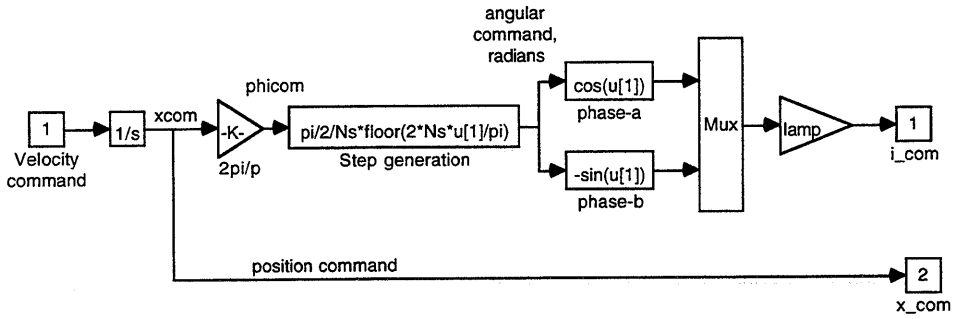

Figure 2.3b. SIMULINK® block diagram of the block "Step drive". This block generates command currents in quadrature for the two phases.

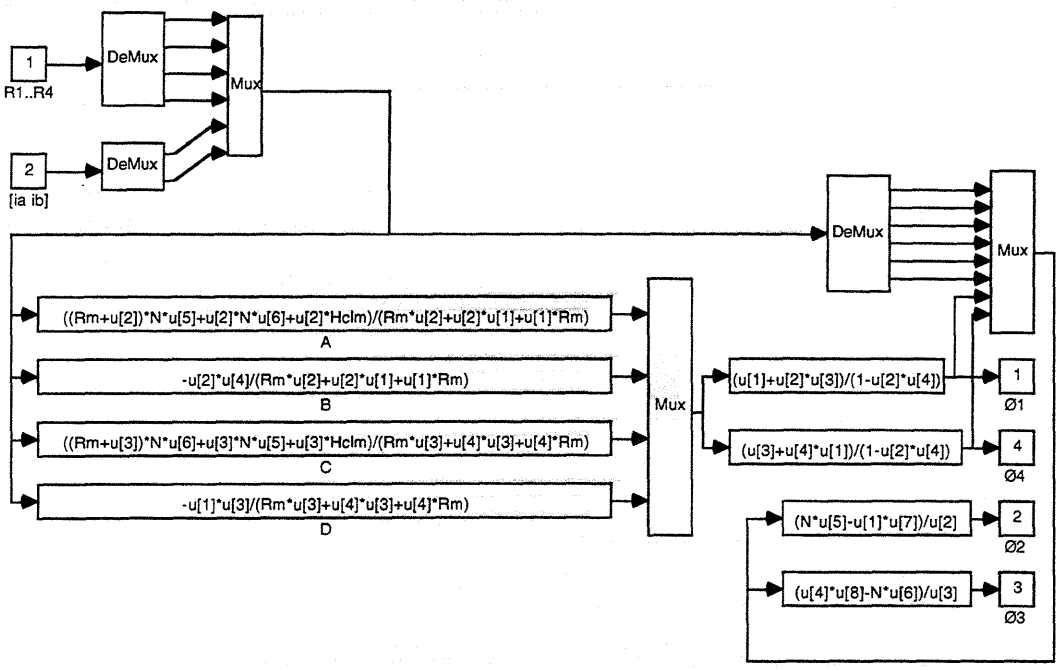

Figure 2.3c. SIMULINK® block diagram of the block "Flux production". Flux at each pole is computed.

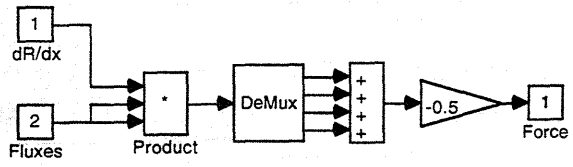

Figure 2.3d. SIMULINK® block diagram of the block "Magnetic force".

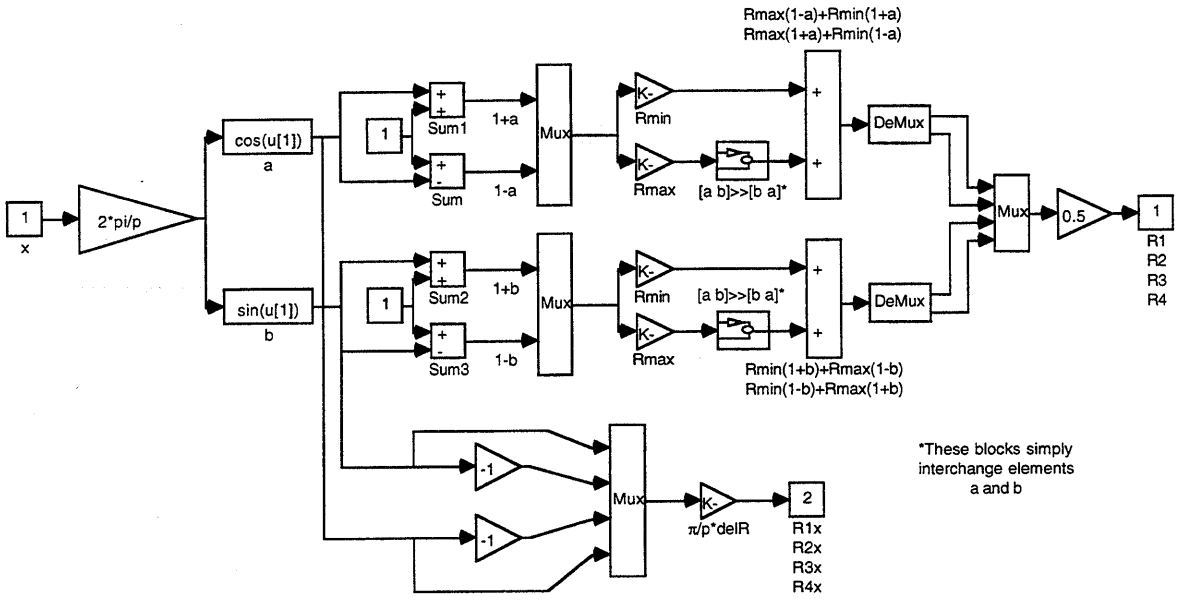

Figure 2.3e. SIMULINK® block diagram of the block "Air gap reluctance".

Solution of the differential equations is obtained by integrating with the 'RK45' routine provided in the software package. The simulation can be run with a simulated 2-phase sinusoidal drive current (as in a synchronous motor), or with a simulated discretized sinusoidal current (simulating the traditional stepper motor driver). The results below show that the performance of the model is similar in form to classic step motor characteristics and, as expected, exceeds the advertised characteristics of the L20 motor (Appendix A).

The simulation parameters require some discussion. They are denoted here using `courier` font and per the nomenclature in the controlling script file '`smotl20.m`' (Appendix C). First, consider the physical parameters. For convenience, the pitch will be represented by `lambda` rather than λ and momentum will be denoted `p`. The total moving mass `m`, is the sum of `mf`, the forcer mass and `mp`, the mass of the payload. The damping coefficient, `r`, was determined by test and its value is discussed in Appendix D.

Calculation of minimum and maximum pole reluctances `Rmax` and `Rmin` is discussed in Appendix B. The user-defined function file '`rmaxmin`' accomplishes the calculation of the reluctances for a given gap, `y`, using the method described by [31]. The gap will be taken as 0.0005 inches nominal, per the manufacturer of the test motor.

The electrical parameters are inputs which can be varied to achieve the desired performance. The input current amplitude is `Iamp`. The current can be changed, but an initial value to use is selected based on the manufacturer's continuous rating (2.7 amp/phase). For a stepping drive, the number of microsteps per cardinal state will be denoted `Ns`. The commercially manufactured driver has an `Ns` of 125, which gives a position resolution of 2 microns.

As discussed above, flux is a dependent variable in this current source driven model; it is therefore unnecessary to calculate the initial fluxes. Earlier models [1, 29] required this calculation to eliminate the initial transients caused by inconsistent initial flux values.

2.6.1 Linear magnetic element model: simulation results

Figure 2.4 shows the response of this lightly damped system to an initial displacement of $\lambda/4$. The applied current is 2.7 amps and the commanded velocity is zero. The natural frequency of the oscillation is approximately 282 Hz. By observing that the decay of the oscillations is nearly exponential, the viscous damping factor $\zeta = 0.043$ can be calculated.

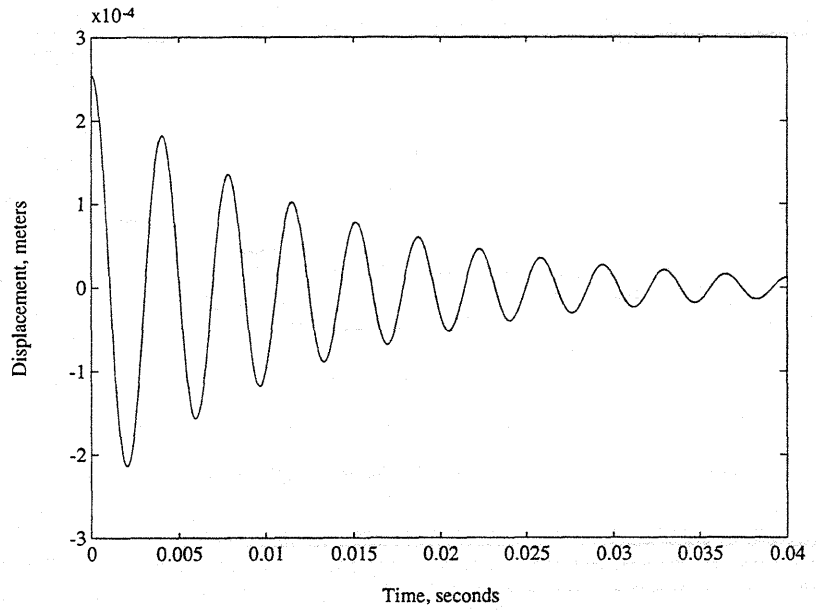

Figure 2.4. Response of system to initial displacement and zero commanded velocity.

Figure 2.5 plots the response of the system to a velocity command of 0.005 meters/second. The motor simulation is run with Ns = 1 step/quarter-pitch (a "conventional" stepper drive) and Ns = 125 (approximating a sinusoidal drive waveform). Notice the step action as the motor moves each cardinal step in the case of the conventional stepper. The microstepping drive, by contrast has a very smooth translation curve; only a small oscillation occurs at the beginning of motion due to the sudden initial acceleration.

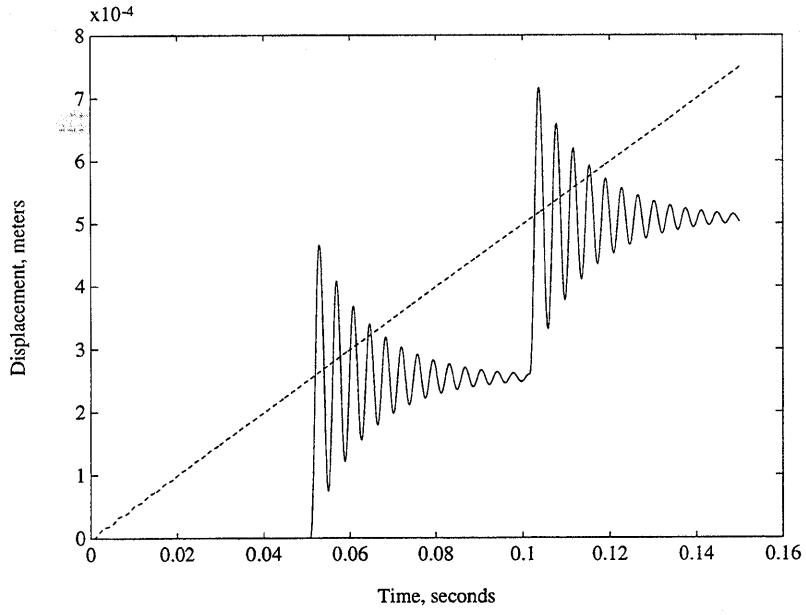

Figure 2.5. System response to velocity command of 0.005 m/s. Single stepping (solid line) and microstepping (dashed line) responses are shown.

Figure 2.6 shows the motor velocity as a function of time as the motor is accelerated at 20 m/s^2 to a commanded velocity of 3 meters/second. The microstepping drive smoothly accelerates the motor to 3 meters/second. Observe the significant velocity ripple present with the single stepping drive. This variation in acceleration resulting from the discontinuous application of current causes the motor to slip out of synchronization. The drive is unable to produce enough force to overcome the sum of the mean acceleration of 20 m/s^2, the drag resistance, and the instantaneous negative acceleration due to the "ringing" at each step.

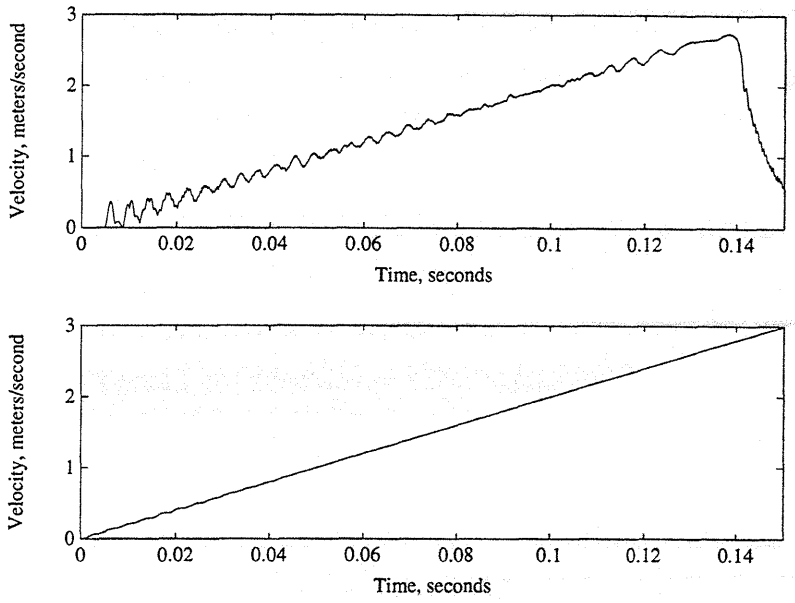

Figure 2.6. Motor velocity during an uniform acceleration to 3 m/s. Upper plot: single steps, lower plot: microstepping.

A program in Appendix C, "`smot120.m`", generates the "pull-out" curve of maximum force versus velocity shown in the plots of Figure 2.7. These curves represent the theoretical force output for this current source driven motor with the single-stepping drive and the microstepping drive. The single-stepping plot shows that the motor will not produce force at the low stepping speeds corresponding to the system resonance shown in Figure 2.4 (and its harmonics). The 282 Hz natural frequency corresponds to 0.072 m/s at the given pitch length. The microstepped motor does not excite these resonances, the velocity ripple is less, and thus the force output is much more stable. This is a common reason that stepper motor users invest in microstepping drives.

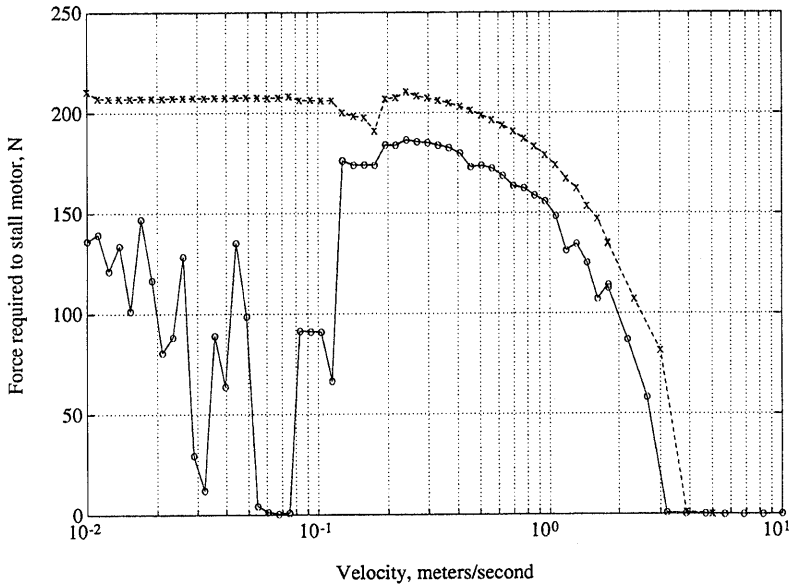

Figure 2.7. Pull-out (maximum) force versus motor velocity. Dashed line: microstepping, solid line: single stepping.

Static force production of the motor varies with position as the rate of reluctance change varies. Figure 2.8 shows the force output as a function of position.

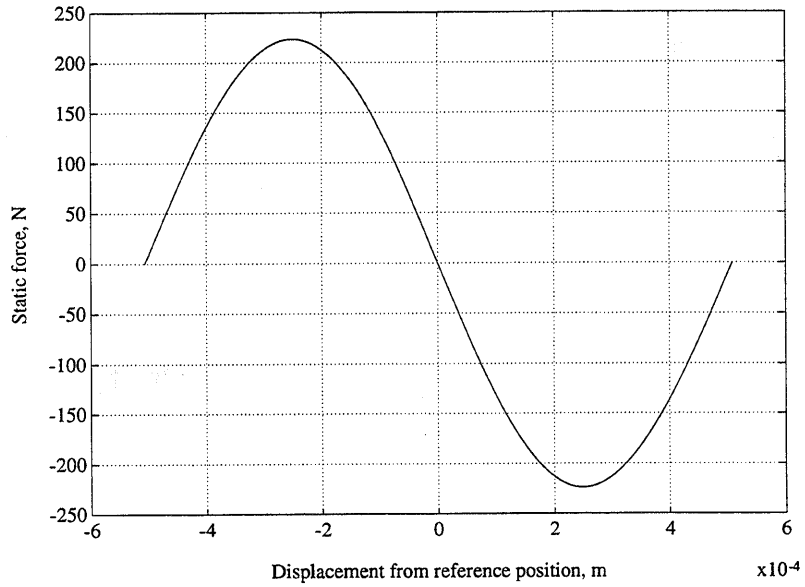

Figure 2.8. Static force production of the simplified motor.

The maximum force occurs at 1/4 pitch displacement from the commanded position. Since the simulation does not account for magnetic saturation of the motor teeth, the form of this curve is exactly sinusoidal

$$F_{static} = F_{max} \sin(\frac{2\pi x}{\lambda}).$$

Utilizing this fact, the stiffness of the motor around its equilibrium point can be calculated as

$$k = \frac{dF_{static}}{dx}\bigg|_{x=0} = \frac{2\pi F_{max}}{\lambda} \cos(\frac{2\pi x}{\lambda})\bigg|_{x=0} = \frac{2\pi F_{max}}{\lambda},$$

and the undamped natural frequency as

$$f = \frac{1}{2\pi}\sqrt{\frac{k}{m}} = \sqrt{\frac{F_{max}}{2\pi\lambda m}}. \qquad (2.32)$$

Applying the assumed motor parameters to relation (2.32) yields a natural frequency of 279 Hz, matching the result of Figure 2.4. Since this simulation has linear magnetic elements, an arbitrarily large force can be generated by simply increasing the drive current, which would not be the case with a real motor. Also, as the teeth saturate according to a non-linear relation, some distortion of the sinusoidal wave shape would be expected.

Assuming that the motor driver is an ideal current source implies that the amplifier will supply as much voltage as is required. Figure 2.9 shows a plot of the voltage (sampled) at the windings as a function of velocity for the microstepping acceleration of Figure 2.6. The voltage at 3 m/s is approximately 400 volts. This is theoretically possible. However, there is an actual limit of 170 volts from the amplifier supplied by the motor manufacturer. From the plot, a reduction of performance above about 0.7 m/s is therefore expected. The next section will address the amplifier limitations.

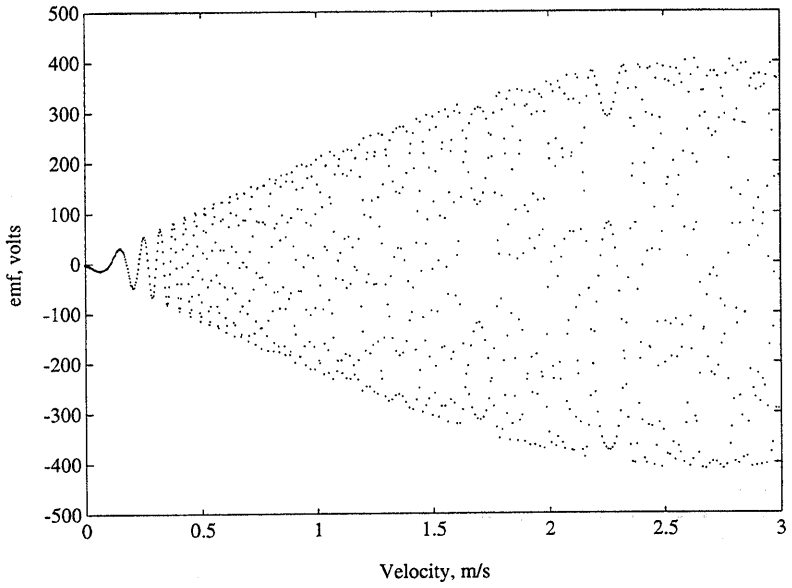

Figure 2.9. Power supply emf output during motor acceleration. (Simulation data sampled at 0.15 millisecond intervals)

2.7 Modification of the model to incorporate a non-ideal driver circuit.

The assumption of the driver electronics acting as an ideal current source is a significant simplifying assumption for two reasons. One, the voltage required to maintain the desired current in the windings is a function of the rate of flux change, which is also related to motor velocity. Therefore, as shown earlier, at some velocity the motor will have significant back emf to limit the current (and power) available from the power source. This back emf will also depend on the motor acceleration and mass which is crucial to the purpose of this study. The second reason for concern about this assumption is the frequency response of the current source amplifier. The electronics must have sufficient bandwidth to maintain commanded current under all dynamics of the motor including higher order harmonics generated by the non-linearity inherent in the device. In the regime where the current source assumption is not valid, the state equations change and the system is higher order.

With the causality assigned as shown in Figure 2.2, the presence of winding resistance does not affect the state equations. The resistance does add to the voltage required at the terminals of the amplifier to achieve the commanded current. If the causality of the system changes because the source is not a current source, but a voltage source, the resistance of the coil is relevant to determining the flux and the force at the poles.

If the motor is assumed to be driven by an ideal *voltage* source, the model can be made to more accurately account for the non-ideal characteristics of the driver circuit. Modification of the motor model only requires changing the sources, and redefining the causality in accordance with the bond graph formalism. The resulting bond graph is shown in Figure 2.10.

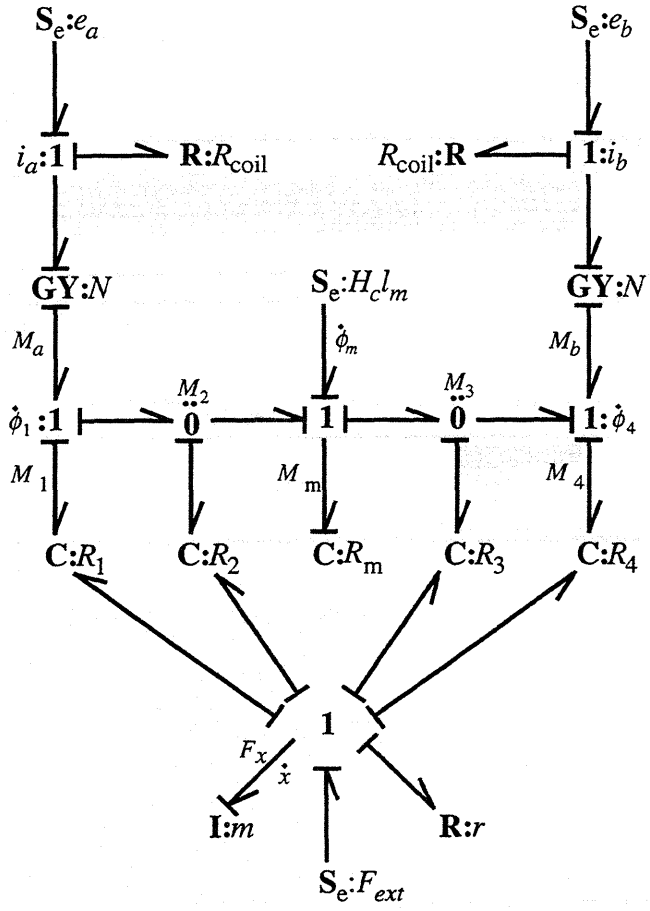

Figure 2.10. Motor system bond graph, modified to show voltage-driven causality.

As before, the system of 1-port capacitances and junction elements can be reduced to a capacitor field.

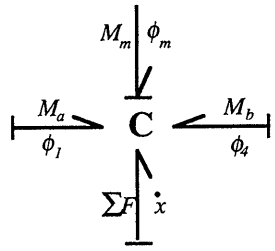

Now it is clear that the field has three bonds in integral causality, and there are now two additional state variables ϕ_1 and ϕ_4.

The derivation of state equations is similar to that above, all of the elements retain their constitutive relations, all of the junction structure is intact, and the mechanical system is unchanged. However, the change in causality forces some of the equations to be written differently, since the state variables and inputs have been revised. The inputs are now e_a and e_b, the voltages applied to the two windings.

The mmf at each coil is determined from the junction structure and the fluxes

$$M_a = (R_1 + R_2)\phi_1 - R_2\phi_m, \tag{2.33}$$

$$M_b = (R_3 + R_4)\phi_4 - R_3\phi_m. \tag{2.34}$$

Similarly, the permanent magnet flux can be determined algebraically

$$\phi_m = \frac{R_2\phi_1 + R_3\phi_4 + H_c l_m}{R_m + R_2 + R_3}. \tag{2.35}$$

The rates of flux change in the coils are equal to the coil voltage divided by the number of turns, where the coil voltage has been reduced by a loss across the coil resistance.

$$\dot{\phi}_1 = \frac{e_a - R_{coil} i_a}{N} = \frac{e_a}{N} - R_{coil}\frac{M_a}{N^2}, \tag{2.36}$$

$$\dot{\phi}_4 = \frac{e_b - R_{coil} i_b}{N} = \frac{e_b}{N} - R_{coil} \frac{M_b}{N^2}. \tag{2.37}$$

Equations (2.36) and (2.37), together with (2.33), (2.34), and (2.35), form the state equations for ϕ_1 and ϕ_4. The fluxes at the other two poles are dependent and calculated directly

$$\phi_2 = \phi_1 - \phi_m, \quad \phi_3 = \phi_m - \phi_4. \tag{2.38}$$

The other state equations are exactly as before,

$$\dot{p} = -\frac{1}{2}\Phi^T \frac{\partial}{\partial x}\mathbf{R}(x)\Phi - r\frac{p}{m} + F_{ext}, \text{ and} \tag{2.26}$$

$$\dot{x} = \frac{p}{m}. \tag{2.12}$$

There is now a need to calculate the initial conditions on the fluxes. These initial conditions are a function of pole reluctance at the initial motor position, $x(t_0)$, and the permanent magnet mmf. The steady state initial fluxes can be calculated directly by apportioning the permanent magnet flux between the poles. This is easily done using the resistance-reluctance analogy applied to the network of reluctances in Figure 2.10.

$$\phi_1(t_0) = \frac{B_r A_m}{\left(1 + R_{gap}(t_0)/R_m\right)\left(1 + R_1(t_0)/R_2(t_0)\right)},$$

$$\phi_4(t_0) = \frac{B_r A_m}{\left(1 + R_{gap}(t_0)/R_m\right)\left(1 + R_4(t_0)/R_3(t_0)\right)},$$

where,

$$R_{gap}(t_0) = \frac{1}{1/R_1(t_0) + 1/R_2(t_0)} + \frac{1}{1/R_3(t_0) + 1/R_4(t_0)}.$$

This calculation must be performed at the start of any simulation to avoid a large startup transient.

Now that the state equations are in the form to accept a voltage input, the power source model is redefined as a voltage source. The system monitors the winding currents and adjusts the voltage to maintain a constant current, within the voltage and response limitations of the amplifier. To do this, it is necessary to add a current feedback loop, a voltage limiter, and a transfer function to the model described in Figure 2.2. The modified diagram is shown in Figure 2.11. The air gap reluctance and magnetic force blocks not detailed below are the same as in Figure 2.2.

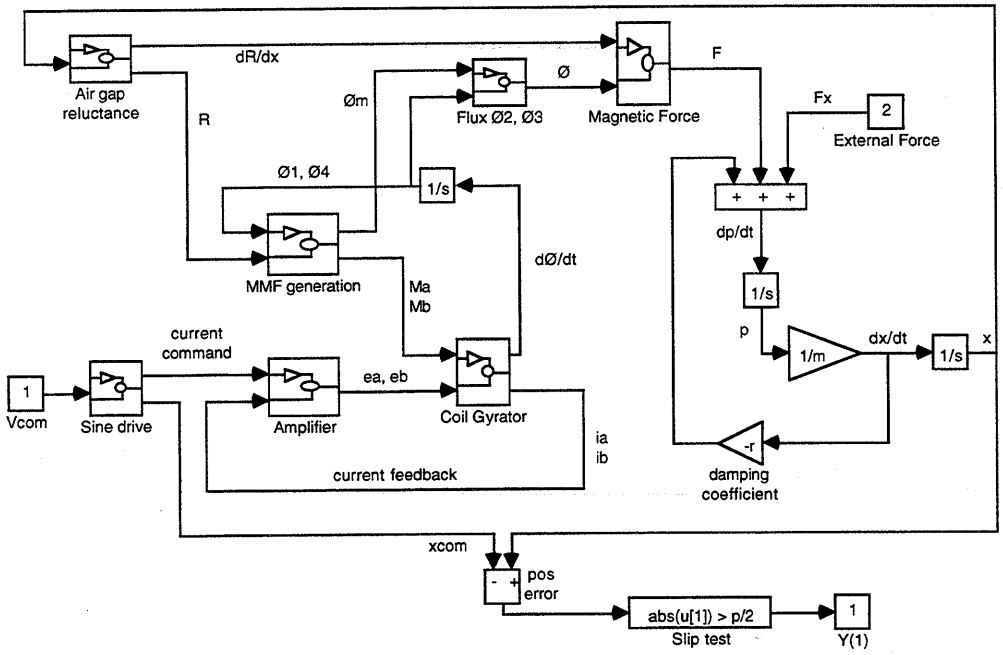

Figure 2.11a. SIMULINK® block diagram of the motor incorporating amplifier model.

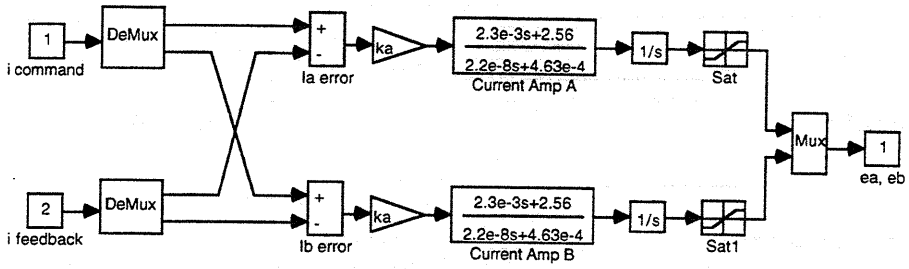

Figure 2.11b. Details of "amplifier" block.

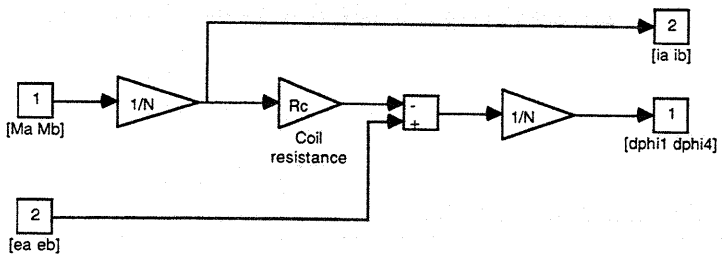

Figure 2.11c. "Coil gyrator" block diagram.

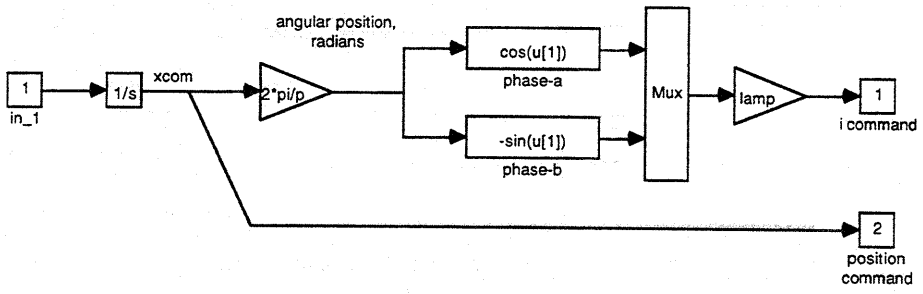

Figure 2.11d. "Sine drive" phased current indexer.

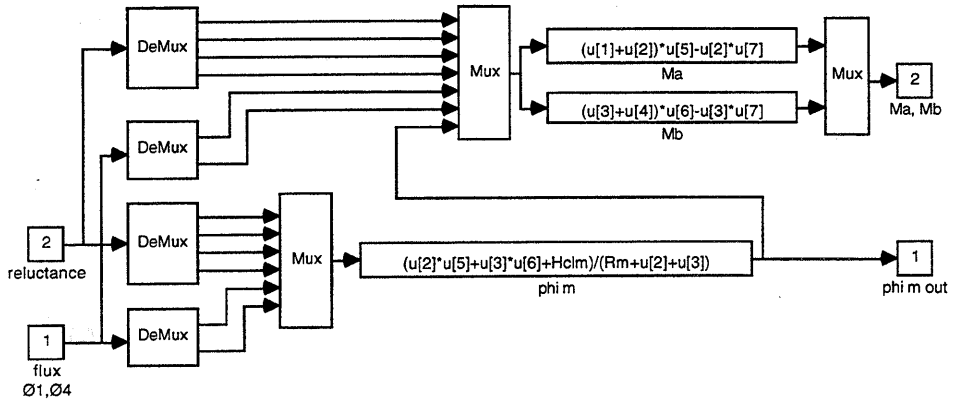

Figure 2.11e. "MMF generation" block. This block calculates permanent magnet flux and coil MMF from the equations above.

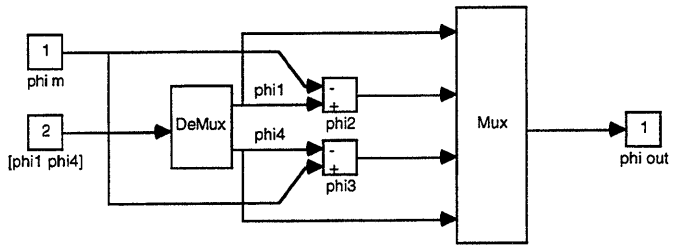

Figure 2.11f. "Flux calculation" block derives ϕ_2 and ϕ_3 from ϕ_m , ϕ_1 and ϕ_4.

A voltage limit of 170 volts (L20 driver voltage limit) is included in the amplifier model. The transfer function for the amplifier was reported from experimental data in [30]. Here, the gain of the transfer function (`ka`) was left as an adjustable parameter. For this motor simulation, the maximum velocity was attainable with the gain tuned to `ka` = 20. This is the setting used in all of the simulations in this chapter.

A new script "`emotl20.m`" (Appendix C) was prepared to calculate the initial conditions and control all of the system parameters for the simulations of the voltage driven motor with the amplifier.

2.7.1 Linear magnetic element model with amplifier: simulation results

Simulation of the above system confirms the expected effects on the behavior of the model. The amplifier response (impedance) effectively adds damping to the motor response.

Figure 2.12 shows the response of this system to an initial displacement of $\lambda/4$. The commanded current is 2.7 amps and the commanded velocity is zero. The natural frequency of the oscillation is approximately 275 Hz. By observing that the decay of the oscillations is roughly exponential, the viscous damping factor $\zeta = 0.078$ can be calculated. There is a noticeable increase in damping as compared with Figure 2.4. The drive is no longer infinitely "stiff", and the electrical elements now dissipate power.

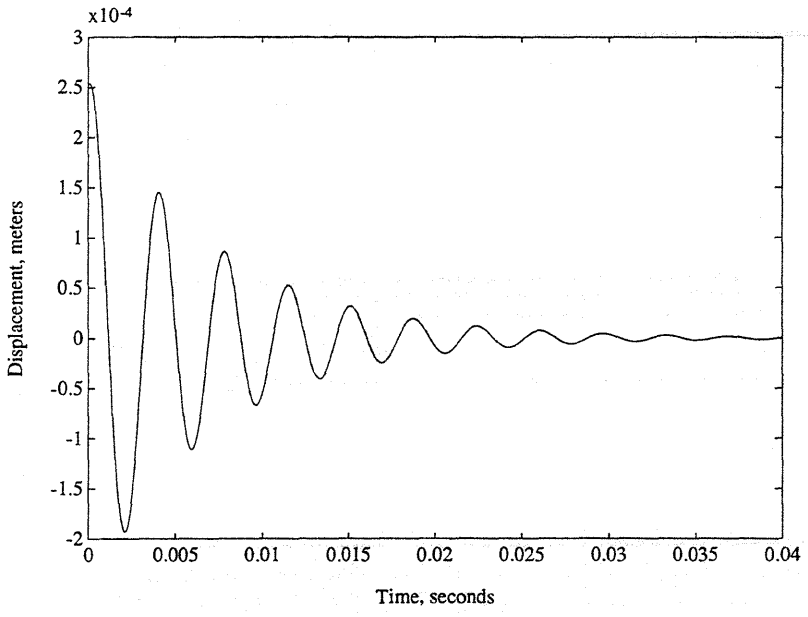

Figure 2.12. Response of system to initial displacement and zero commanded velocity.

Figure 2.13 plots the response of the system to a velocity command of 0.005 meters/second. The motor simulation is run with `Ns` = 1 step/quarter-pitch (a "conventional" stepper drive) and `Ns` = 125 (approximating a sinusoidal drive waveform). This should be compared to the response shown in Figure 2.5.

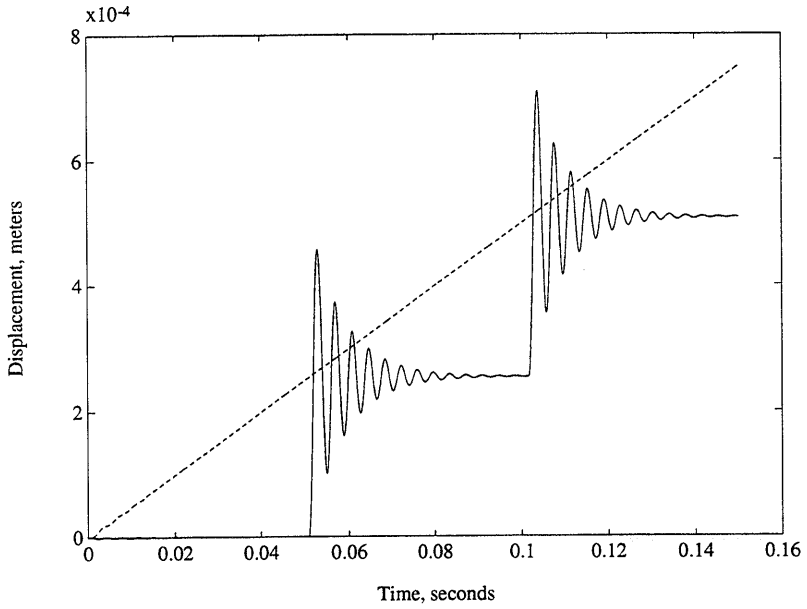

Figure 2.13. System response to velocity command of 0.005 m/s. Single stepping (solid line) and microstepping (dashed line) responses are shown.

Figure 2.14 shows the motor velocity as a function of time as the motor is accelerated at 20 m/s^2. The microstepping drive smoothly accelerates the motor to nearly 1.7 meters/second. Although there is still velocity ripple present with the single stepping drive, comparison with Figure 2.6 shows that it is reduced significantly as a result of the additional damping and reduced bandwidth of the electronics. Both drives lose synchronization (velocity drops to zero) at much lower speeds than achieved with the ideal drive. This is a reflection of the reduced voltage available and the ability of the amplifier to control winding current.

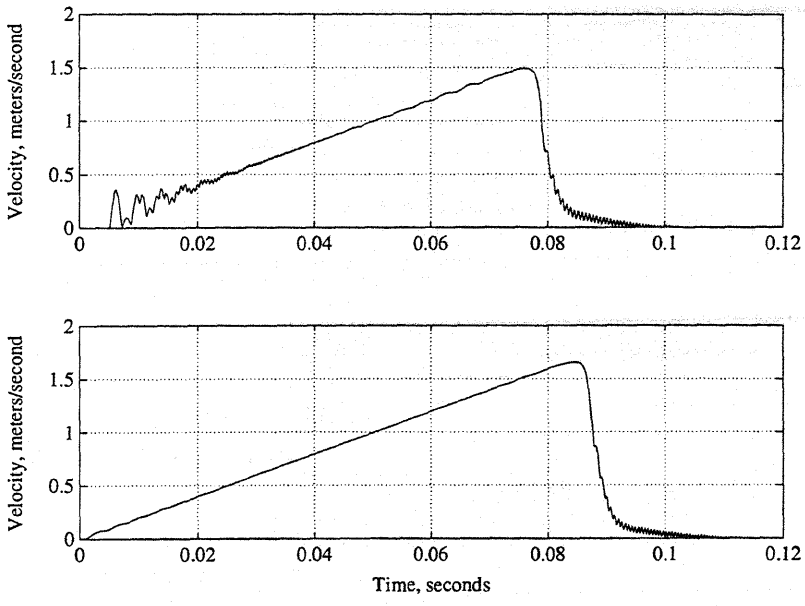

Figure 2.14. Motor velocity during an uniform acceleration to 3 m/s. Upper plot: single steps, lower plot: microstepping.

Simulation of the "pull-out" characteristic of maximum force versus velocity results in the plots of Figure 2.15. These results show similarity to the plots of Figure 2.7. Again, the microstepped drive eliminates much of the velocity ripple which tends to pull the motor out of synchronization at low force when single-stepping. Note the expected reduction in force produced at velocities over 0.7 m/s where the amplifier becomes voltage limited. The single-stepped motor with a non-ideal drive shows some additional force capability at low speed in Figure 2.15, when compared to the ideal drive (refer to Figure 2.7). This appears to be the result of the additional damping, which reduces the oscillations that tend to kick the motor out of synchronization.

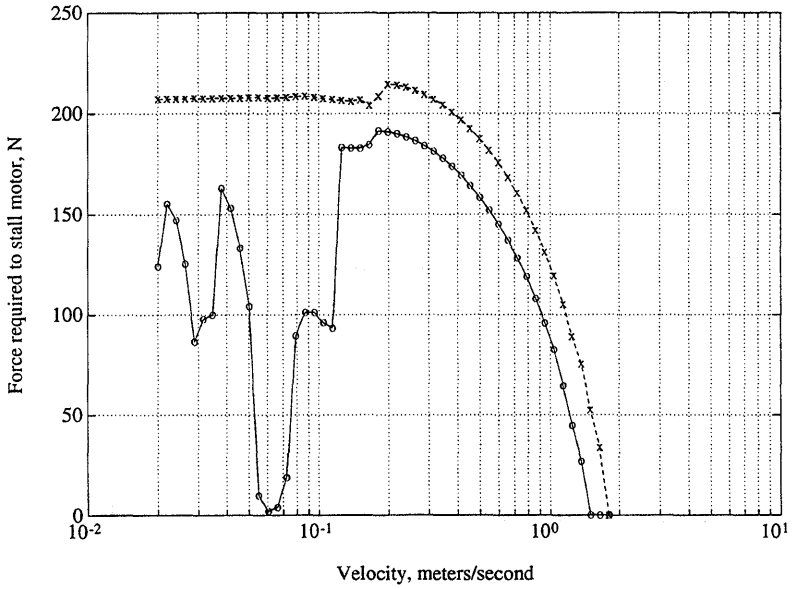

Figure 2.15. Pull-out (maximum) force versus motor velocity. Dashed line: microstepping, solid line: single stepping.

Figure 2.16 shows a plot of the voltage at the windings as a function of velocity for the microstepped acceleration of Figure 2.14. The voltage limit of 170 volts from the amplifier is evident at 0.7 m/s.

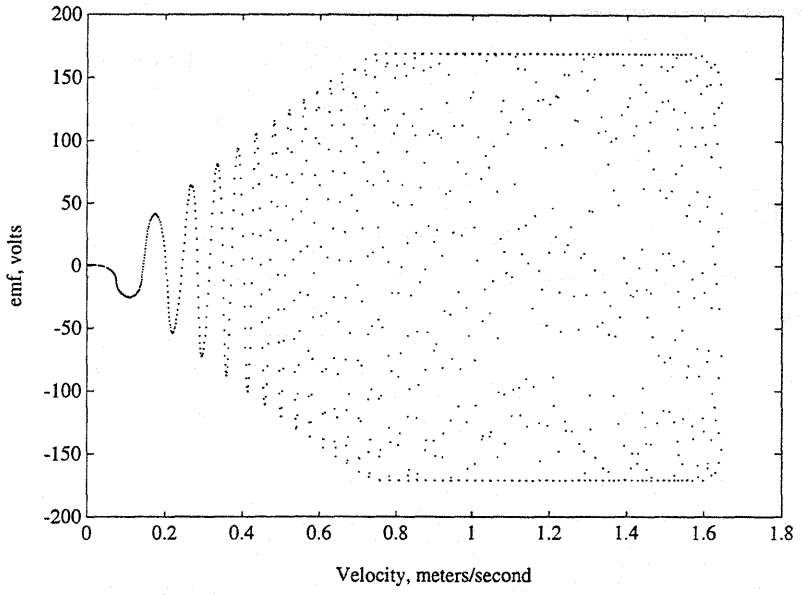

Figure 2.16. Power supply emf output during motor acceleration. (Simulation data sampled at 0.075 millisecond intervals)

In the simplified model, the motor system is highly idealized. The damping coefficient was essentially empirically determined. There was no attempt to include saturation, hysteresis, or eddy current effects. Given all of the simplifications, the simulation is remarkably accurate, and gives a good idea of how the motor behaves. Because of its simplicity, this simulation runs fast and may be useful for preliminary design analysis, particularly if correlation with a laboratory model or prototype is possible. For a more accurate simulation, and to be useful in designing a motor with little or no lab data, the losses and non-linearities must be modeled more carefully.

Chapter 3

Analysis of magnetic losses and saturation

3.1 Modeling eddy current losses

Until now, the assumption has been that eddy currents behave as simple resistive losses, modeled as viscous losses in the mechanical domain. This is an adequate first approximation, but evaluation of the detailed behavior of these losses may be important.

The Sawyer motor will typically be operated at varying speeds (frequencies), therefore it is important to understand how magnetic losses occur and how they vary with frequency and material properties. It is also desirable to separate the eddy current effects associated with each magnetic structure in the motor. With a simulation tool which will predict losses and damping, the motor designer can select materials and geometry to yield the desired performance under a variety of operating conditions.

Eddy currents have two significant characteristics which need to be considered. First, they introduce a phase shift component to the M - $d\phi/dt$ relationship as described below. Secondly, eddy currents force the flux to be concentrated in the surface of the metal. The well-known "skin-effect" is the result of the induced currents establishing a magnetic field near the surface of the material which effectively opposes the penetration of the flux into the metal.

Assume that a low level sinusoidal magnetic field is applied to a magnetic material such that the material is not near saturation. When plotted against each other, mmf and flux rate will plot an ellipse, not a straight line as with the simple viscous load resistor modeled in Chapter 2. The material has introduced a phase lag between the input field and output flux rate. Eddy currents circulate around in loops and therefore add an inductive characteristic to the system, just like a coil. This phase shift (sometimes referred to as "loss angle") , occurs in any conductive material. In fact, the phase behavior of eddy currents serves as a tool in the testing of non-ferrous metals for defects. In a magnetic material, the magnetic permeability increases the effective inductance of the eddy loops. It should be noted that the measured loss angle is partly caused by hysteresis, but the frequency-dependent portion is primarily the result of eddy currents induced by the changing flux.

Solution of the general eddy current problem is a daunting mathematical task. The non-linear properties of ferromagnetic materials, combined with the non-sinusoidal nature of the motor excitation do not yield results which are readily applied to a lumped model. Further, assumptions about the homogeneous nature of the magnetic alloys are not strictly true. The domain and crystalline structure results in so-called "excess" or "anomalous" eddy current losses which masquerade as true eddy current losses, but cannot be explained by classical theory [9]. These excess losses typically amount to 20% of the total core loss in 60 Hz machines [32] and even more in certain alloys and under high excitation. Even given all of these uncertainties, a model of the magnitude and phase of these losses and their controlling parameters is still desirable for time domain modeling of motor systems.

3.1.1 Derivation of the eddy current lumped model

We will begin by assuming a linear, hysteresis-free magnetic material with resistivity ρ, and permeability μ. Consider a magnetic flux path of n identical laminations. The return path for the flux is assumed to have zero reluctance (infinite permeability). The approach here will be to model each lamination as a non-conducting magnetic material, wound with one turn of a non-magnetic conductor. This one turn "coil" will carry the eddy current for the lamination in the model. It has a resistance, r_e and an inductance, L_e. These are the eddy current equivalent resistance and inductance. Figure 3.1 illustrates the concept.

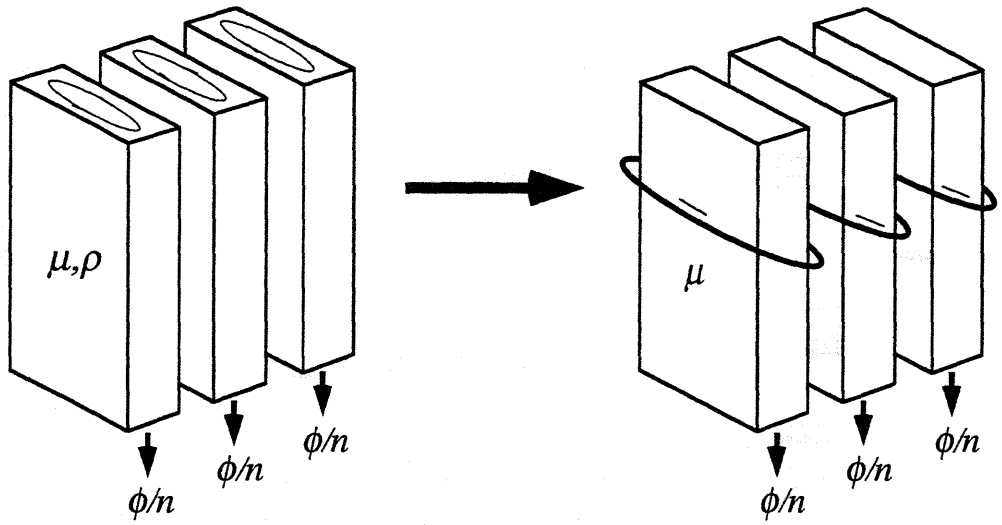

Figure 3.1. Diagram of eddy currents in ferromagnetic laminations. These are modeled as one-turn coils around permeable non-conductors.

The currents which actually flow in a lamination will flow in the same direction as the currents in the hypothetical coil as required by Faraday's law, $\nabla \times \mathbf{E} = -\partial \mathbf{B}/\partial t$. The distribution of currents in the idealized coil will obviously differ from the actual case, but the basic electromagnetic behavior is similar. The objective of this effort is to derive values for the eddy current equivalent resistance and inductance which have the same effect as the actual material. These lumped parameters then serve as the simulation elements.

Bond graph of Figure 3.2 shows the energy flow of the laminated magnetic system. Note that the laminations are magnetically in parallel. In the magnetic domain there is a capacitance (reluctance R_a) based on the flux carrying area of the lamination, its length and permeability. Through a gyrator of modulus equal to one, changing flux induces an eddy voltage which is impressed across an inductor (L_e) with series resistance (r_e). The coil is represented by a gyrator of unity modulus (one turn). Each lamination carries $1/n$ of the total flux and has the same applied mmf since they are identical. This allows a reduction of the bond graph to that shown in Figure 3.3. The equivalent eddy current resistance and inductance for the laminated system are nr_e and nL_e respectively.

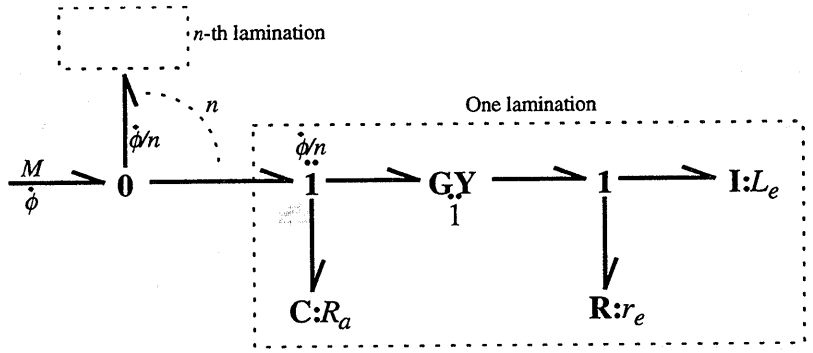

Figure 3.2. Bond graph representation of modeled n lamination magnetic system.

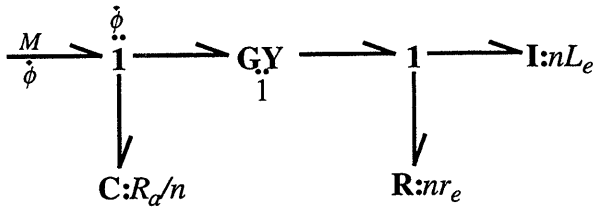

Figure 3.3. Bond graph of Figure 3.2 reduced to equivalent form for n laminations.

L_e and r_e will be selected to make the power dissipation in this system match the theoretical eddy current losses. In the electrical domain, the magnetic reluctance R_a looks like an inductor, L_a. The equivalent electrical domain system is shown in Figure 3.3.

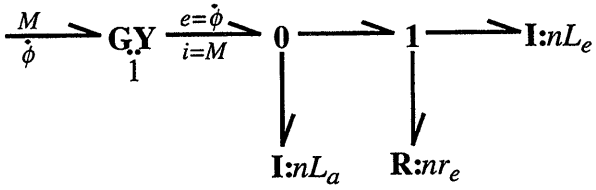

Figure 3.3. Equivalent electrical domain bond graph.

The eddy currents and magnetic field concentrate in the surface "skin" of the metal, where the skin depth, δ is defined by the characteristic depth of the skin effect in a semi-infinite plate [28]

$$\delta = \sqrt{\frac{2\rho}{\omega\mu}} = \sqrt{\frac{\rho}{\pi f\mu}}\,. \tag{3.1}$$

Thus, eddy current and field penetration are less in low resistivity, high permeability materials at high frequency. Figure 3.5 defines the geometry of a lamination, assumed much thinner than wide and long.

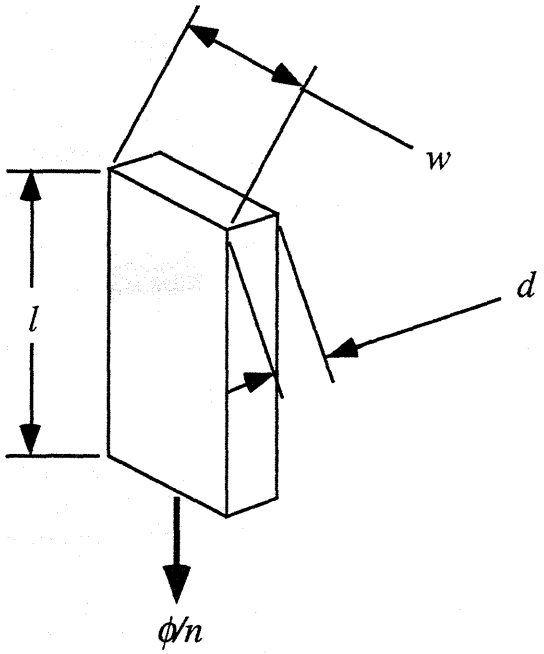

Figure 3.5. Lamination geometry and orientation.

The estimate of r_e and L_e is derived from classical eddy current theory. Consider a thin plate similar to Figure 3.5. Recall the material is assumed to be uniform and linear (i.e., no hysteresis and constant permeability). A sinusoidal mmf is applied to this plate

$$M = \hat{M}\sin(\omega t),$$

and therefore

$$H = M / l = \hat{H}\sin(\omega t).$$

Note that H is the field strength at the surface of the lamination. Eddy currents will reduce the field in the interior portions.

Assume the flux variation is sinusoidal,

$$\phi = \hat{\phi}\sin(\omega t - \theta)$$

then the flux rate

$$\dot{\phi} = \hat{\phi}\omega\cos(\omega t - \theta).$$

This is the time rate of change of the total flux in the path under consideration. Note that because of the eddy currents, the flux is out of phase with the applied field by angle θ. Solving for the phase angle θ will help define the relationship between L_e and r_e.

In the actual case, the non-linear flux-mmf relationship distorts the sinusoidal flux wave and results in significant harmonic content, especially at flux levels approaching saturation. This distortion may be expected to result in higher losses than those predicted here.

The instantaneous power supplied by the magnetic field is the product of the applied field and the total flux

$$P_e(t) = M(t)\dot{\phi}(t) = lH(t)\dot{\phi}(t).$$

The phase difference results in

$$P_e(t) = l\hat{H}\sin(\omega t)\hat{\phi}\omega\cos(\omega t - \theta) = \frac{l\hat{H}\hat{\phi}\omega}{2}[\sin\theta + \sin(2\omega t - \theta)]. \quad (3.2)$$

Then the time average power of the applied field is

$$\overline{P}_e = \frac{l\hat{H}\hat{\phi}\omega}{2}\sin\theta. \quad (3.3)$$

The time average power dissipated under these conditions resulting from eddy currents has been derived in analytical form [3] and presented here (in SI units),

$$\overline{P}_e = dlw\frac{\rho\hat{H}^2}{\delta d}\frac{\sinh(d/\delta) - \sin(d/\delta)}{\cosh(d/\delta) + \cos(d/\delta)}.$$

The trigonometric terms account for the finite thickness of the plate. For later convenience, set

$$K_1 = \frac{\sinh(d/\delta) - \sin(d/\delta)}{\cosh(d/\delta) + \cos(d/\delta)} \tag{3.4}$$

so,

$$\overline{P}_e = dlw\frac{\rho\hat{H}^2}{\delta d}K_1. \tag{3.5}$$

If the only power dissipated is caused by eddy currents, then setting (3.3) equal to (3.5) and solving for $\sin\theta$,

$$\sin\theta = 2w\frac{\rho\hat{H}}{\delta\omega\hat{\phi}}K_1. \tag{3.6}$$

Using the definition (3.1) for δ, (3.6) can be rewritten as

$$\sin\theta = \frac{\delta}{d}\frac{dw\mu\hat{H}}{\hat{\phi}}K_1. \tag{3.7}$$

The quantity $\hat{B}_{avg} = \dfrac{\hat{\phi}}{dw}$ is the average magnitude of the flux density in the lamination. If H is the field strength at the surface of the lamination, then $\hat{B}_{surf} = \mu\hat{H}$ is the magnitude of the surface flux density. Substituting these quantities in (3.7),

$$\sin\theta = \frac{\delta}{d}\frac{\hat{B}_{surf}}{\hat{B}_{avg}}K_1. \tag{3.8}$$

The eddy currents result in a time variation of B within the material that is out of phase with the applied field by some angle which varies with the distance to the surface. The overall flux, which represents the integrated flux density over the whole thickness, is phase shifted by angle θ. The solution to the (idealized) thin plate eddy current problem [7] makes it possible to determine the ratio $\frac{\hat{B}_{surf}}{\hat{B}_{avg}}$ and thus the angle. The flux density magnitude in the plate is derived from Maxwell's Equations as

$$\hat{B}(x) = \hat{B}_0 \cosh\left(\frac{x}{\delta}\right),$$

where $\hat{B}_0$ is the magnitude of the flux density in the center of the plate, and x is the distance from the center of the plate. Given this, the surface flux density and average flux density are easily found as

$$\hat{B}_{surf} = \hat{B}(d/2) = \hat{B}_0 \cosh\left(\frac{d}{2\delta}\right),$$

and

$$\hat{B}_{avg} = \frac{1}{d}\int_{-d/2}^{d/2} \hat{B}(x)dx = \frac{2\delta}{d}\hat{B}_0 \sinh\left(\frac{d}{2\delta}\right).$$

Therefore,

$$\frac{\hat{B}_{surf}}{\hat{B}_{avg}} = \frac{d}{2\delta}\frac{\cosh(d/2\delta)}{\sinh(d/2\delta)} = \frac{d}{2\delta}\coth(d/2\delta) = K_2, \tag{3.9}$$

where this ratio has been defined as K_2. Finally, from (3.8)

$$\sin\theta = \frac{\delta}{d}K_1K_2. \tag{3.10}$$

The phase angle θ between the magnetic flux and the applied field has been defined by (3.10) in terms of only the lamination thickness, d and the skin depth, δ. The same phase shift will be introduced by r_e and L_e. Instantaneous power is the product of the voltage, e and the total current, i. Because the gyrator modulus of the hypothetical one-turn coil is unity, this is exactly the same as the product of the flux rate and the mmf. To find r_e and L_e it is necessary to equate the phase and magnitude of the flow and effort variables in the electrical system with those derived from the magnetic system.

Using the relationships developed above, the magnitude of the total current (mmf) can be related to the magnitude of the voltage (flux rate)

$$\hat{i} = \hat{M} = l\hat{H} = l\frac{\hat{B}_{surf}}{\mu} = \frac{l}{\mu}\hat{B}_{avg}K_2$$

$$= \frac{l}{\mu}\frac{\hat{\phi}}{dw}K_2 = \frac{l}{\mu dw}\frac{\hat{\phi}\omega}{\omega}K_2 = \frac{l}{\mu dw}\frac{K_2}{\omega}\hat{e},$$

where $\hat{e} = \omega\hat{\phi}$ is the relationship between the voltage and the flux rate.

Evaluating the relationship between the current $i = \hat{i}\sin(\omega t)$ and the voltage

$$e = \hat{e}\cos(\omega t - \theta) = \hat{e}\sin\left(\omega t + \frac{\pi}{2} - \theta\right)$$

in terms of the circuit resistance and inductances yields

$$\hat{i} = \hat{e}\sqrt{A^2 + B^2}, \tag{3.11}$$

where

$$A = \frac{\omega L_e}{r_e^{\,2} + \omega^2 L_e^{\,2}} + \frac{1}{\omega L_a},\quad B = \frac{r_e}{r_e^{\,2} + \omega^2 L_e^{\,2}} \text{ and } \theta = \tan^{-1}\left(\frac{B}{A}\right).$$

Using the angular and magnitude relationships between current and voltage derived above

$$\sqrt{A^2+B^2}=\frac{l}{\mu dw}\frac{K_2}{\omega}, \text{ and } \frac{B}{\sqrt{A^2+B^2}}=\sin(\theta).$$

Solving for A and B,

$$B=\frac{l}{\mu dw}\frac{K_2}{\omega}\sin(\theta) \text{ and } A=\frac{l}{\mu dw}\frac{K_2}{\omega}\cos(\theta). \tag{3.12}$$

Let

$$A'=A-\frac{1}{\omega L_a}=\frac{\omega L_e}{r_e{}^2+\omega^2 L_e{}^2}.$$

Then

$$\frac{A'}{B}=\frac{\omega L_e}{r_e} \text{ and } A'^2+B^2=\frac{1}{r_e{}^2+\omega^2 L_e{}^2}.$$

Solving for r_e and L_e yields

$$L_e=\frac{A'}{\omega\left(A'^2+B^2\right)}, \text{ and } r_e=\frac{B}{A'^2+B^2} \tag{3.13}$$

which depend on the value of L_a, the linearized anhysteretic inductance. Continuing to assume that the core permeability is constant under a given excitation, L_a for a single lamination can be approximated by

$$L_a \approx \mu dw / l. \tag{3.14}$$

Two key assumptions are made here which deserve some discussion. The constant permeability, μ used here may differ from that used in the calculation of skin thickness, δ. For simplicity, I have chosen to use only one value for the two calculations. A constant permeability is a liberal approximation to the very non-linear B-H characteristic. It is a parameter which should be adjusted somewhat to match the simulated losses to actual losses. The classical eddy current theory predicts the general behavior of eddy current losses quite well, if not the exact magnitude. The use of a constant L_a for a ferromagnetic material is also justified by the necessary simplification of the simulation, and validated if the results bear some resemblance to experience. (Although assumed constant to calculate the eddy current response, elsewhere in the simulation a non-linear table look-up value represents the actual capacitance of this element. See the section on the anhysteretic magnetization curve.)

The other assumption made here is that the effective flux carrying section area of this element equals the physical area. The actual case is that the flux carrying area is reduced by the skin effect and that the effective thickness of the lamination is reduced at high frequencies. Again, the choice of an approximation should be adjusted to make the simulated power dissipation and the shape of the synthetic B-H loops match the material test data.

Proceeding with those assumptions, substituting L_a into equations (3.12) yields

$$B = \frac{K_2}{\omega L_a}\sin(\theta) \text{ and } A = \frac{K_2}{\omega L_a}\cos(\theta).$$

Then

$$A' = A - \frac{1}{\omega L_a} = \frac{K_2\cos\theta - 1}{\omega L_a}.$$

Making these substitutions into (3.13) produces the results

$$L_e = L_a\left(\frac{K_2\cos\theta - 1}{K_2{}^2 - 2K_2\cos\theta + 1}\right), \tag{3.15}$$

and

$$r_e = \omega L_a \left(\frac{K_2 \sin\theta}{K_2{}^2 - 2K_2 \cos\theta + 1} \right). \tag{3.16}$$

3.1.2 Summary of eddy current simulation equations

Calculation of the eddy current equivalent resistance and inductance reduces to evaluating the following equations:

$$\delta = \sqrt{\frac{2\rho}{\omega\mu}} = \sqrt{\frac{\rho}{\pi f \mu}}, \tag{3.1}$$

$$K_1 = \frac{\sinh(d/\delta) - \sin(d/\delta)}{\cosh(d/\delta) + \cos(d/\delta)}, \tag{3.4}$$

$$K_2 = \frac{d}{2\delta} \coth(d/2\delta), \tag{3.9}$$

$$\sin\theta = \frac{\delta}{d} K_1 K_2, \tag{3.10}$$

$$L_a \approx \mu dw / l, \tag{3.14}$$

$$L_e = L_a \left(\frac{K_2 \cos\theta - 1}{K_2{}^2 - 2K_2 \cos\theta + 1} \right), \tag{3.15}$$

and

$$r_e = \omega L_a \left(\frac{K_2 \sin\theta}{K_2{}^2 - 2K_2 \cos\theta + 1} \right). \tag{3.16}$$

The preceding relations are coded in the MATLAB® function '`lerea.m`' (Appendix E).

3.1.3 Model of a lamination with eddy current loss

In modeling a system, it is desirable to model the elements based on their intensive material properties and then subsequently scale them by geometric size factors. This approach will facilitate the block modeling of more complex systems. To make the preceding equations consistent with this intent, it is necessary to factor out the area and length of the magnetic path.

First, transfer the eddy current elements L_e and r_e to the magnetic domain. This transformation of Figure 3.3 is shown in Figure 3.6. Next, assign the preferred integral causality for ease in casting the equations. (This assignment of causality will turn out to be valid, as will be seen later in this chapter.) Also, the electrical element nomenclature has been maintained, but converted into equivalent magnetic domain form.

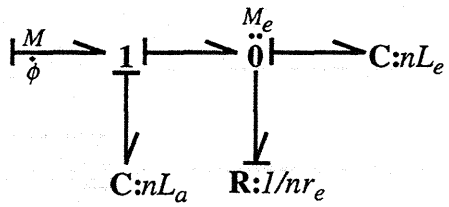

Figure 3.6. Equivalent magnetic domain bond graph (refer to Figure 3.3)

The input to the magnetic system is flux rate and the output is mmf. Again, all of the eddy current model elements are assumed linear. Thus the equation for M_e, the mmf output of the R-C parallel combination becomes

$$M_e = \frac{1}{nL_e}\int\left(\dot{\phi} - M_e n r_e\right)dt.$$

At the -1- junction, this mmf will be added to the mmf from the capacitance nL_a

$$M = M_e + \frac{1}{nL_a}\int \dot{\phi}dt.$$

Remove the geometric factors from M_e by letting $M_e = H_e l$, and $\dot{\phi} = B/A = B/ndw$. Then

$$H_e = \frac{1}{nL_e}\left(\frac{Bndw}{l} - \int nr_e H_e dt\right)$$

is the magnetic field strength in terms of the flux density. Now substitute the expressions for L_e and r_e, equations 3.15 and 3.16. The result is

$$H_e = \frac{1}{nL_a C_1}\left(\frac{Bndw}{l} - \int n\omega L_a C_2 H_e dt\right),$$

where

$$C_1 = \frac{K_2 \cos\theta - 1}{K_2{}^2 - 2K_2 \cos\theta + 1} \text{ and } C_2 = \frac{K_2 \sin\theta}{K_2{}^2 - 2K_2 \cos\theta + 1}. \quad (3.17)$$

(Relations 3.17 are also coded in the MATLAB® function "`lerea.m`" in Appendix E.)

Replacing L_a with $\mu dw/l$ and removing the geometric factors n, d, w and l;

$$H_e = \frac{1}{C_1}\left(\frac{B}{\mu} - \omega C_2 \int H_e dt\right). \quad (3.18)$$

In addition to the eddy current loss, there are the anomalous losses which behave like eddy currents but are not predicted by the classical theory. The anomalous loss varies with alloy, material form, and grain size but always increases the total loss. These losses will be accounted for by the use of a "calibration" factor, k_e. This factor multiplies the eddy current mmf to effectively scale the losses directly.

Using equation 3.18, the laminated system consisting of a single linear magnetic element (Figure 3.6) is modeled in SIMULINK®. Figure 3.7 shows the simulation block diagram of the eddy current model. A voltage source and N-turn gyrator have been added to excite the magnetic system. The model was tested with the following values typical of a silicon motor lamination steel: $\mu_r = 4000$ (constant), $\rho = 400 \times 10^{-9}$ Ω-m, $\gamma = 7650$ kg/m^3

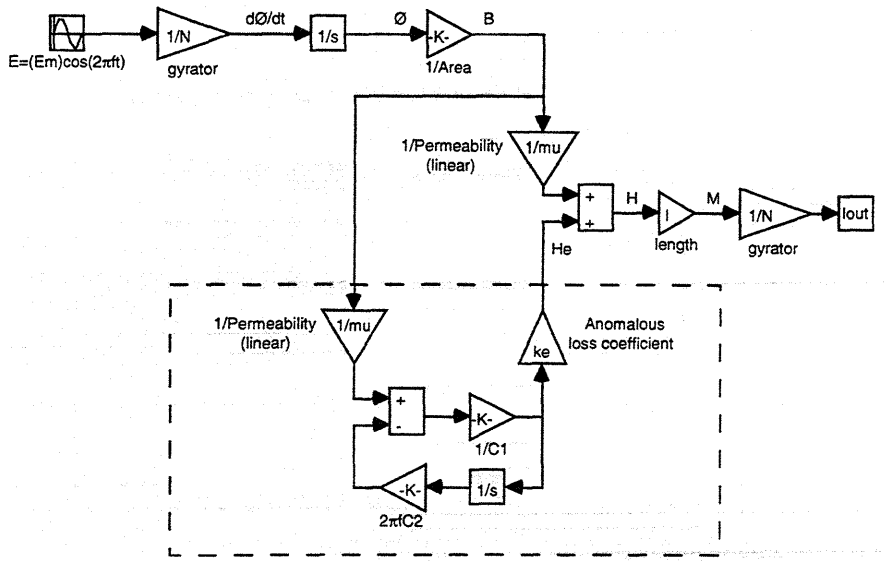

Figure 3.7. SIMULINK® model of a ferromagnetic element. Eddy currents are modeled by means of the subsystem enclosed in dashed lines. No hysteresis of saturation effects.

During the simulation, flux input and mmf output data are collected for each time step. At the completion of the simulation, the mean power consumption over time T is calculated over the interval t_1 to t_N using the flux and mmf data according to

$$P = \frac{1}{T}\int_{t_1}^{t_N = t_1 + T} M\left(\frac{d\phi}{dt}\right)dt.$$

This power can be numerically approximated for small time steps as

$$P \cong \frac{1}{T}\sum_{k=1}^{N} M(t_k)\left(\frac{\phi_{k+1} - \phi_{k-1}}{t_{k+1} - t_{k-1}}\right)\left(\frac{t_{k+1} - t_{k-1}}{2}\right) = \frac{1}{2T}\sum_{k=1}^{N} M(t_k)\left(\phi_{k+1} - \phi_{k-1}\right).$$

This power calculation is implemented as a MATLAB® function shown in Appendix E.

Figure 3.8 is a plot of the power dissipated versus frequency and lamination thickness. It demonstrates the specific power loss attributed to eddy currents in accordance with the classical eddy current theory ($k_e = 1$).

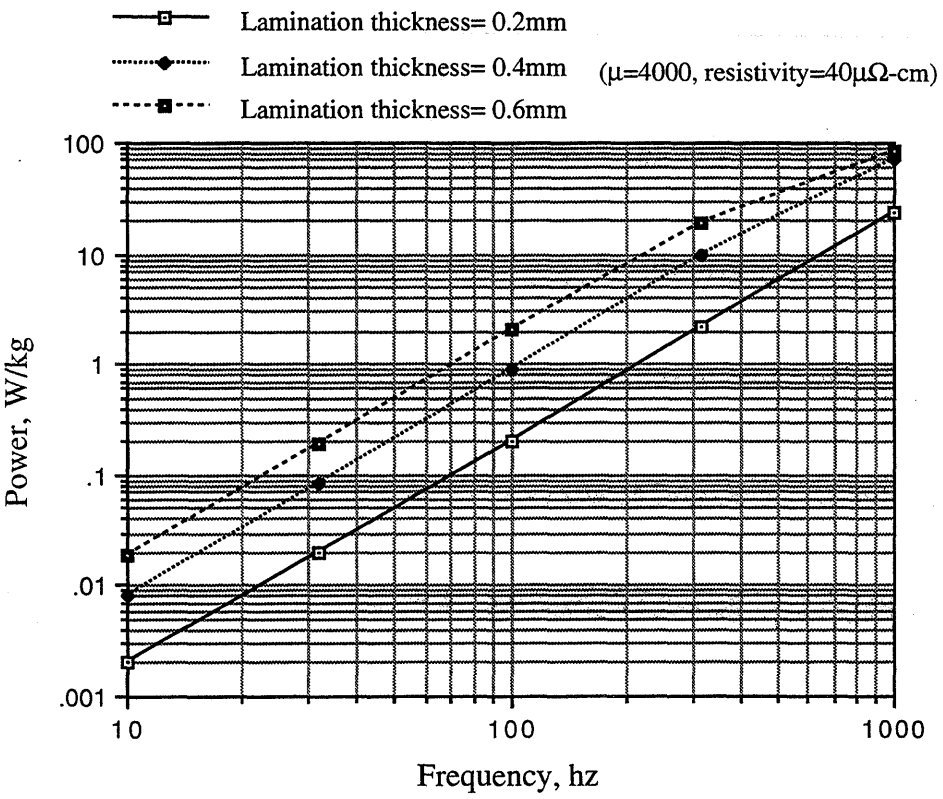

Figure 3.8. Eddy current losses, linear model of a single lamination. 1.0 T excitation.

The elliptical loops in the B-H plot (Figure 3.9) are the result of the simulation for three frequencies. The effect of increasing frequency (reducing skin depth) on the phase angle between effort (field strength) and displacement (flux density) is to increase the area within the ellipse (power dissipated). As frequency increases, the major axis of the ellipse rotates clockwise. This is explained by skin depth decreasing proportional to the square root of frequency (equation 3.1). At very high frequency, r_e increases approximately as the square root of frequency while the flux rate increases directly proportional to frequency. The result is that M_e will increase roughly as the square root of frequency to maintain constant flux amplitude.

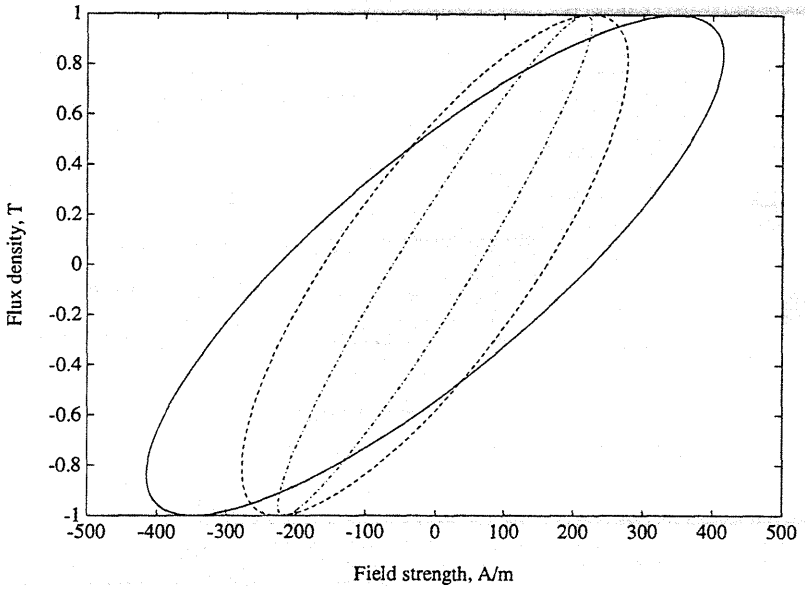

Figure 3.9. Plot of magnetic response with eddy current effects modeled.
(..... 316 Hz, - - - - 1000 Hz, —— 3160 Hz, 0.36 mm thick lamination)

3.2 The anhysteretic magnetization curve and saturation

The hysteresis-free, ideal or "anhysteretic" magnetization curve represents the magnetization response with the effect of hysteresis removed. This was represented in the bond graph nomenclature (Figure 3.6) as a simple linear capacitive element. Potential energy is stored in this element represented by the integral of the effort (M) with respect to displacement (ϕ). The constitutive relation is of the form $M = f(\phi) = R_a\phi$. In reality, of course, this function is quite non-linear.

The non-linearity is the result of the nature of the magnetization process within a ferromagnetic material. Classically, the physical microstructure of an isotropic ferromagnetic material consists of a large number of randomly oriented polarized elements called magnetic domains. Simply put, some of these domains are more susceptible to magnetization than others. These domains also interact magnetically, as the magnetic polarization vector of each domain varies and influences that of its neighbors. There is a statistical distribution of domain susceptibility and interaction which results in an overall bulk response to a magnetic field. The loss-free part of this response is called the "anhysteretic" and the part caused by energy loss is hysteresis. Hysteresis will be addressed in the next section.

Each form of ferromagnetic material has a unique anhysteretic magnetization curve resulting from properties specific to the pure material, modified by structural changes caused by impurities, mechanical processing and heat treatment, etc. The anhysteretic response of a sample can be obtained experimentally by superposing on a static field (H) a slowly alternating component (ΔH) which is initially much greater than the static field. By gradually reducing the magnitude of the alternating component to zero, a single flux density value (B) results. This test is repeated for many values of H. The experimental result (see Appendix H) for a sample toroid of AISI 1018 carbon steel is indicated in Figure 3.10.

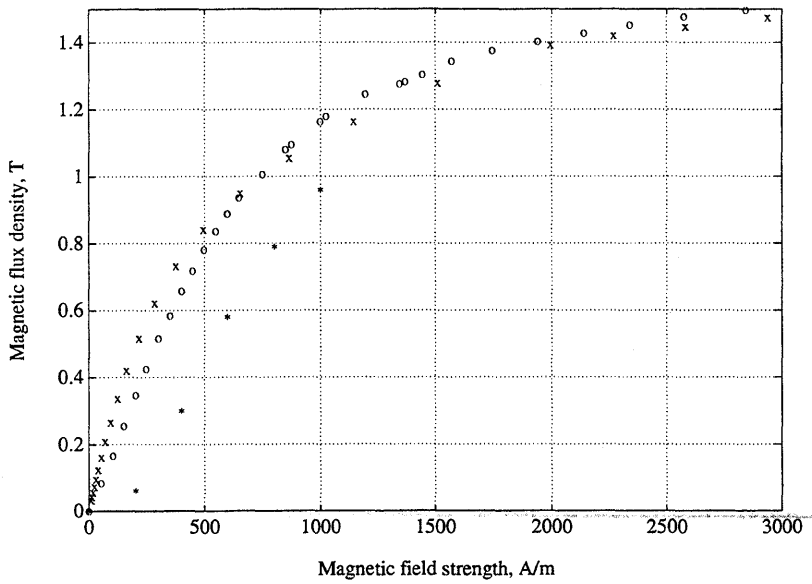

Figure 3.10. Plot of anhysteretic magnetization (x), initial magnetization (*) and average field strength of increasing and decreasing hysteresis loops (o) for AISI 1018 hot-rolled steel. (see Appendix H)

For some materials, the anhysteretic curve can also be approximated by averaging the field strength, H of the left limb of the hysteresis loop with the H of the right limb for each value of flux density, B. This is convenient because the hysteresis loops are much more readily obtained from the literature than anhysteresis data. The graph (Figure 3.10) shows the difference between the two curves for the sample of low carbon steel.

The initial magnetization curve serves as another check of the approximated anhysteretic curve. Jiles and Atherton [10] explain that the initial magnetization curve is always below the anhysteretic curve on a standard B-H diagram. This is because the initial magnetization begins at zero excitation and the internal "friction" which causes hysteresis also causes the magnetic response to lag behind the excitation. For this reason, the initial magnetization curve (which is published for many materials) is less suitable as an estimate of the anhysteretic.

At high values of magnetic field strength, the magnetization (flux) approaches a saturation value dependent on the material. This saturation value applies to polarization of the ferromagnetic material only (the "intrinsic saturation induction", $B_{i,sat}$). If field strength is further increased, the flux will continue to increase, although at a slope essentially determined by the permeability of free space. In the limit, at very high field strengths $dB / dH = \mu_0$. Compared to even modest permeability, this is a very small value, but it is non-zero. A non-zero slope is important to include in the model to help preclude instability at very high simulated fluxes.

The anhysteretic energy storage element could alternatively be represented by a mathematical formula; for example, [11] suggest a relation of the form

$$B = \left(B_{i,sat}\right)\left(\coth\left(\frac{H(1-\alpha)+\alpha\left(B/\mu_0\right)}{a}\right)-\frac{a}{H(1-\alpha)+\alpha\left(B/\mu_0\right)}\right)+\mu_0 H.$$

This function has three parameters (α [dimensionless], a [H units], $B_{i,sat}$) which can be tuned to fit a known anhysteretic characteristic. This function approximates the actual curve and must be evaluated recursively for B as it is not an explicit function of the applied field. This may be a usable approach if the values of the parameters are approximately known and good data does not exist. In practice it is preferable to fit a curve to the experimental data and use a table look-up function in the simulation. If the function above is used, a look-up table should still be generated to accelerate the simulation.

3.3 Modeling hysteresis losses

3.3.1 The nature of hysteresis

The nature of hysteresis makes it the most difficult magnetic phenomena to model. When a magnetic material is subjected to cyclic magnetic excitation, the well-known magnetic hysteresis loop is formed in the B-H (or ϕ-M) plane. The hysteresis loop is usually very similar in shape to the anhysteretic response and for many soft magnetic materials the magnetization curve has the classic "S" shape.

The area of the hysteresis loop represents the energy lost in one cycle. Because of the energy loss, magnetic hysteresis describes a dissipative (or resistive) process. Modeling this phenomena accurately requires some knowledge of the loss mechanisms as well as the magnetic response of some different materials.

The general nature of the relationship between B and H is that it is a repeatable characteristic, but difficult to predict because of a property called "non-local memory" [20]. This means that the future state, $H(t>t_0)$ trajectory of a given specimen is uniquely determined by its future input trajectory, $B(t>t_0)$, its present state, $H(t_0)$ *and its input history* $B(t<t_0)$. The dependence on the prior magnetic history of the specimen is largely limited to the history of input extrema (magnitude at input reversals). Not all extrema are relevant. More recent maxima (or minima) which exceed in absolute value preceding maxima (or minima) will erase the effect of those earlier input reversals. For example, if a sample's excitation is cycled from zero to some positive value, B_+ and back to zero, all previous positive extrema less than B_+ are rendered irrelevant. Thus, various loops in the B-H plane can be traced through the same point depending on the history of the extrema.

This "memory" feature of ferromagnetism is due to the microscopic structure of the material. A basic physical explanation for magnetic hysteresis lies in the motion of a large number of domain walls within the material. Under the influence of an applied field, the growth of domains with favorable magnetic orientation and the corresponding shrinkage of domains with opposing orientation results in a net magnetization of the material. For soft magnetic materials, domain growth is the principal mechanism of magnetization in the range of useful flux densities. If these domain walls were to move without restriction, the change in polarization (flux) would be loss free. However, there are crystal lattice imperfections and impurities which resist the passage of the domain walls. As the walls move, these "pinning sites" are broken and reform in a process which is irreversible (entropy increasing). Hysteresis losses can be measured by detecting the temperature change in a crystal undergoing magnetization [9].

A mechanical analogy to the motion of magnetic domain walls is the mechanical case of a long chain constructed of coil springs alternately connected in series with masses which drag along a surface with static and dynamic friction. The overall length (displacement) of the chain will reach some maximum (saturation) which will not increase once all of the links are stretched to an equilibrium condition with the friction force. If the applied force reverses direction, the distribution of friction attachments changes, but the exact displacement of the object will depend on the history of the force. Predicting the configuration of the chain after a series of moves will require knowing the number of masses, the friction coefficients for each, and the spring constants. Similarly, overall observed magnetic behavior is the result of the density and distribution of domain walls and pinning sites, the statistical variation in pinning energy, and the orientation of domains relative to the applied field.

3.3.2 Approaches to modeling magnetic hysteresis

Several different approaches to modeling the hysteresis phenomena have been proposed. Prominent among these are the approaches devised by Preisach, Karnopp and Jiles and Atherton.

The Preisach [26] model works by modeling the statistical distribution of domain magnetization vectors. The magnetic characteristics of the material must be measured by recording the slopes of the B-H response immediately after magnetization reversal points all along the major loop. These slopes are used to build a distribution function and make it available in tabular form for computer use. Its implementation requires a computer algorithm capable of storing the magnetic history of the element. Each independently magnetized element of the modeled system requires arrays of the local minima and maxima of its magnetization history. The Preisach model has an intuitive basis which is very satisfying, but requires a very specific magnetic database to realize. This has been done with some success [5, 21]. Its practicality is limited in cases where the needed data is not available.

Karnopp [13] proposes an elementary model of hysteretic behavior which consists of a series combination of a coulomb (dry) friction (mmf limited) R - element and a saturating (flux limited) C - element. In series, these elementary models have a basic hysteretic behavior forming a square loop. By connecting a number of these simple R - C models together in parallel, their flux contributions add (similar to the physical case of domains). Each of these R and C elements has its mmf and flux parameters selected such that the overall shape of the system curves approximates the desired hysteresis loops. This approach is intuitive and physically reasonable; however, simulation fidelity is dependent on the number of additional states (R - C elements) added. If a small number of states is used, an arbitrary transition from one magnetic condition to another (minor loops) may not be simulated accurately. In general, the simulated loops are not smooth and "step" from one quantized magnetization condition to another. This will cause high frequency ripple on the simulated current, which can slow down the simulation and affect the eddy current model. Additional states can be added, but at the expense of additional computation effort. Also, as in the Preisach model, a method for specifying the elementary parameters to model an arbitrary magnetic specimen is required. Magnetic data beyond that ordinarily available will be needed for an accurate model.

Jiles and Atherton [10] use energy considerations to derive a differential equation which closely approximates the hysteretic behavior. This differential equation gives fairly good results for simulating hysteresis, but is time consuming to simulate because of its non-linear and implicit nature. A well-defined method for obtaining the parameters for the equations is documented in [11]. Given fairly ordinary magnetic data, plus the anhysteretic curve, a simulation is relatively easy to undertake. Unfortunately, certain conditions near saturation cause the simulated B-H relation to develop a negative slope, a physically unrealistic situation. For these reasons, the Jiles and Atherton approach was not selected for this motor simulation which must operate realistically at high flux levels.

The approach taken here is similar to the Karnopp model. Instead of multiple sets of elementary R - C models, a single, more accurate R - C combination is used. The C - element has a non-linear relationship based on the anhysteretic measurements. The previous section discussed the anhysteretic curve in more detail. A basic description of the proposed hysteretic R - element follows.

The new hysteresis R - element is empirically designed to add an additional mmf loss to that from the anhysteretic element. This mmf addition is positive for increasing flux and negative for decreasing flux, thereby defining a hysteresis. If a fixed mmf were added as soon as the flux changed direction, this would be analogous to a coulomb friction and result in a very square loop with constant width. Although a passable model of the major loop results, such an approach would be grossly inaccurate for minor loops which are always narrower than the major loop. In order to smooth the transition and generate reasonable minor loops, a function is proposed which adds mmf gradually as a function of the flux change from the last magnetization reversal.

The shape of the simulated hysteresis loop is determined by the anhysteretic response and modified by the rate ($dM/d\phi$) at which mmf is added to the anhysteretic. This additional mmf is added as an exponential function of the flux change since the last reversal, asymptotically approaching a maximum value. On decreasing magnetization, the effect is reversed, i.e. mmf is subtracted. The maximum additional mmf is typically 2 times the maximum coercive force, H_c. The total displacement from the anhysteretic will then be $\pm H_c$, yielding the correct limiting (or major) hysteresis loop.

Finally, in order to ensure that no discontinuity results when reversing the flux rate, the increasing and decreasing exponential functions are forced to match at the transition point.

The resulting R - element has a characteristic which is shown in Figure 3.11 for cycling flux at two different flux densities. The limiting H (mmf per unit length) differs slightly for the two different flux densities; i.e., the width of minor loops will vary as the magnitude of the flux excursion. This is a refinement which will be explained in the next section.

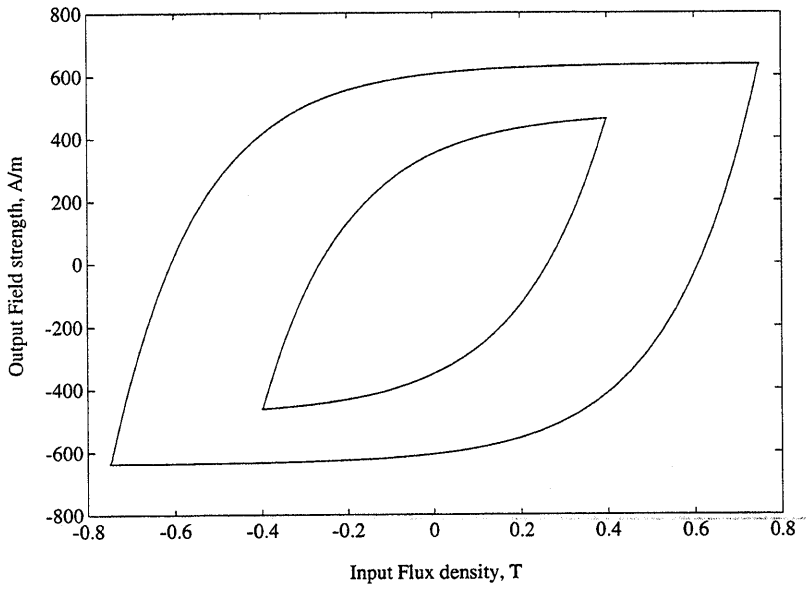

Figure 3.11. Output vs. Input of the Hysteresis R - element at two different peak flux densities. Clockwise around the loop is in the direction of increasing time.

The direction that the loop is traced defines an element that always dissipates energy equal to the area of the loop, which is the desired result. The result of this synthetic relation is a quasi-resistive element. It can store a limited amount of energy, but in going around a loop, or after sustained flux change, must dissipate energy. The hysteresis element is described in more detail below.

3.3.3 Simulation of the hysteresis loss

As discussed in the last section, the hysteresis simulation relies on the observation that the hysteresis resistance is principally a coulomb friction, except that the effort changes gradually (rather than suddenly) at the point where the displacement changes direction. Its design is also motivated by the observation that a fixed maximum hysteresis (loop width) exists for a given specimen, regardless of the magnitude of magnetic excitation. This is a crucial point. The overall magnetic specimen is flux limited and thus would seem to accept only an effort (mmf) input. However, the hysteresis element by itself can only accept a displacement input because its mmf range is limited Since the displacement cannot be defined for arbitrary effort, the causality of the hysteresis element must be based on a displacement causing an effort. This causality can also be interpreted in terms of flow ($d\phi/dt$) changing sign. This is the same causality as a coulomb friction. The flux limited behavior of a ferromagnetic material is introduced by the anhysteretic capacitance, whose mmf rises very steeply for flux density exceeding the saturation induction.

The effort (H) resulting from a change in displacement (ΔB) is always a ΔH from the anhysteretic in the direction of opposing the change. This ΔH is denoted H_R. By observation, the magnitude of H_R approaches a maximum of approximately H_c, but is also somewhat dependent on the magnitude of the peak flux density. This approach is modeled as an exponential

$$H_R = f(\Delta B) = k\left(k_f |B_-| + 1\right)\left(1 - 2e^{\frac{-(B-B_u)}{b}}\right), \tag{3.19}$$

for B increasing with time. For decreasing B, a similar expression is assumed:

$$H_R = f(\Delta B) = -k\left(k_f |B_+| + 1\right)\left(1 - 2e^{\frac{-(B_d-B)}{b}}\right). \tag{3.20}$$

Sample and hold blocks "remember" the last maximum and minimum values of the flux density (B_- and B_+ respectively). These maxima and minima are used to define the trajectory starting point functions B_u and B_d. Since the displacement may reverse direction at any flux level, the B_u and B_d functions must be offset to smoothly connect the increasing and decreasing trajectories of the loop. These functions are therefore defined by the interception of the increasing and decreasing trajectories,

$$B_u = B_+ + b\ln\left(1 - e^{\frac{-(B_d - B_+)}{b}}\right),$$

and

$$B_d = B_- - b\ln\left(1 - e^{\frac{-(B_- - B_u)}{b}}\right).$$

The simulation always calculates B_u and B_d from the most recent values of the maxima and minima.

The coercive force H_c is usually measured as the field strength required to return the flux density to zero. The factor k primarily determines the width of the loops and is thus related to the coercive field strength, H_c. The factor k_f is used to compensate for the fact that the width (deviation from anhysteretic curve in A/m) of the hysteresis loop is not constant in general. For some materials including silicon steels, the loop is wider at high flux density. The k_f factor adds to the width of the hysteresis loop an amount proportional to the magnitude of the most recent flux extrema (B_+ or B_-). This extra width is added at a limited rate to avoid sudden changes when the flux maxima are not constant. Here again, the synthesis of a relationship between loop width and flux extrema is based on observation of actual hysteresis loops. This relationship can be tailored to the needs of the problem under study. The adjustment of k and k_f requires knowledge of the shape of the hysteresis curve, or the area of the loop under different flux densities.

The flux constant, b determines the rate of field strength change resulting when changing the flux density by a single power of e. The value of b determines how closely the loop reversals mirror the anhysteretic curve, or the relative "roundness". A very small value of b will result in a very sharp, nearly coulomb friction, characteristic. The value of b has its strongest effect on loop shape when the flux excursion is relatively small; i.e. minor loops.

The simulation of hysteresis is accomplished with a sub-system block in the SIMULINK® environment (Figure 3.12). The block's input is flux density and the output is field strength. Using these specific quantities permit the simulation to be scaled for any size columnar magnetic element. Knowing the cross section area and the length of the element enables the hysteresis block to interface with the rest of the system.

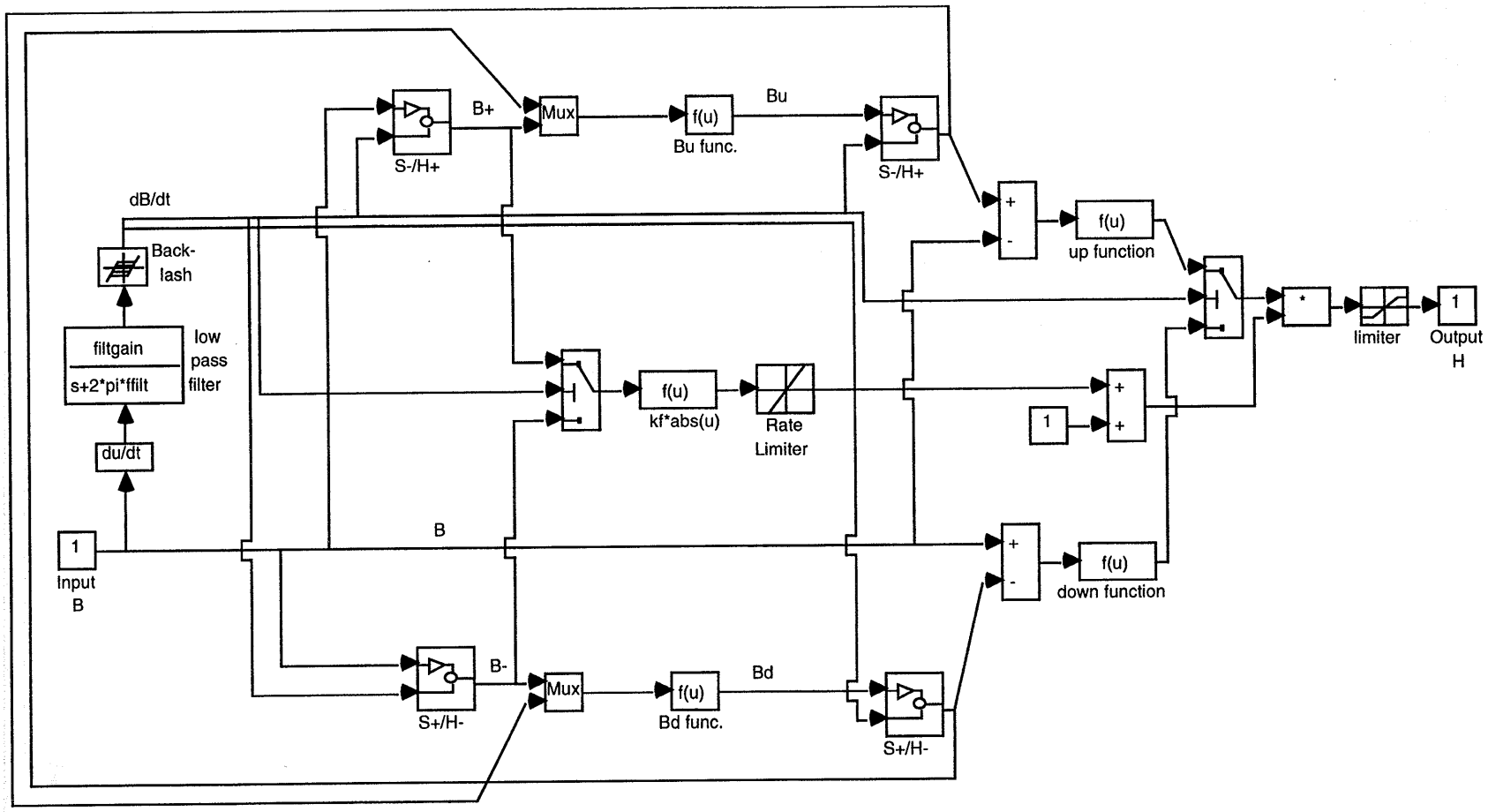

Figure 3.12. SIMULINK™ block diagram of the hysteresis resistance element.

Use of this model depends on knowing when the flux rate changes sign. The "switch" blocks that select between increasing and decreasing functions as well as the sample and hold function are triggered by a change in the sign of the derivative of the flux density. Derivatives in a simulation can be noisy and induce erratic simulation and instability. Therefore, the derivative output is filtered by a low pass filter with deadband. The flux derivative low pass filter frequency and gain are adapted to the frequency of the fundamental excitation to avoid any loss of fidelity.

Figure 3.13 shows the SIMULINK® block diagram of a model using hysteresis simulation based on the anhysteretic curve of a mild steel. The effort, H out of the hysteresis and anhysteresis blocks is summed, as in a -1- junction.

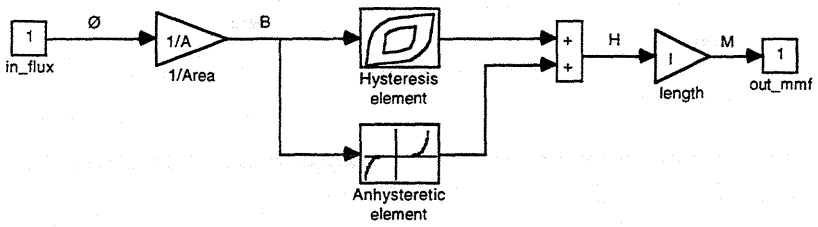

Figure 3.13. Block diagram of hysteresis simulation. The block labeled "Hysteresis element" is shown in Figure 3.12. The "Anhysteretic element" is a SIMULINK® Look Up Table linear interpolation block.

Figure 3.14 shows B-H loops generated using the simulation. This simulation demonstrates the capability to model minor loops. The fit of the simulation to measured data requires manipulating the k, k_f, and b parameters in the simulation to match available data. Fortunately, the behavior of the simulation is not excessively sensitive to any of these parameters. It is relatively easy to select a single set of parameter values giving reasonable accuracy for both the major and minor loops.

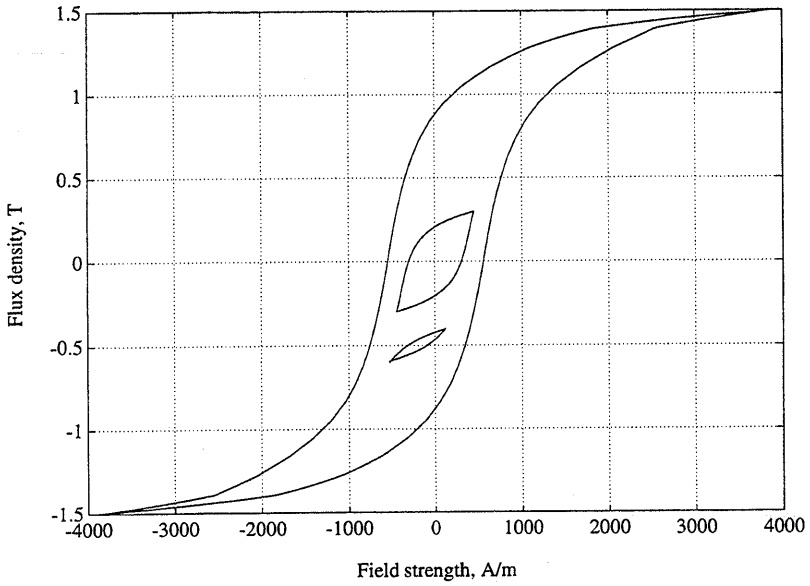

Figure 3.14. Hysteresis simulation of 1018 steel showing minor loops.

Figures 3.15 and 3.16 compare the simulation with hysteresis loops measured on a specimen of AISI 1018 mild steel.

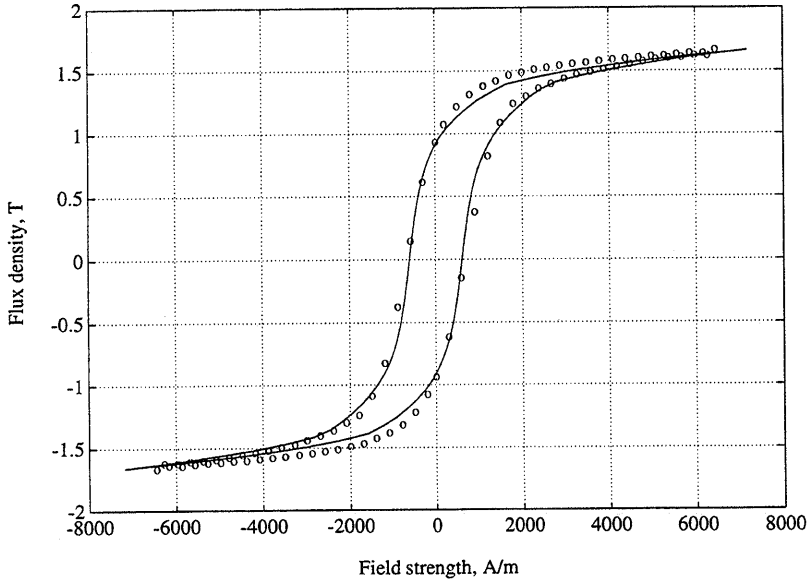

Figure 3.15. Magnetic hysteresis loops for AISI 1018 solid toroid. Data (ooo) and simulated hysteresis loop (solid line)

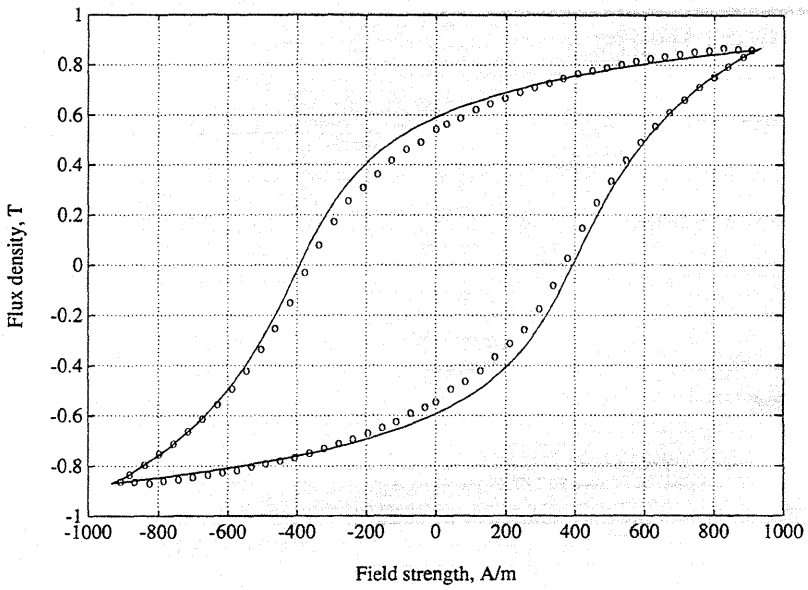

Figure 3.16. Magnetic hysteresis loops for AISI 1018 solid toroid. Experimental data (ooo) and simulated hysteresis loop (solid line)

3.4 Magnetic simulation with hysteresis, eddy currents and saturation effects

The hysteresis model above can now be combined with the eddy current model. A simple magnetic circuit consisting of a closed, single material, ferromagnetic path and an N-turn coil is simulated by the block diagram in Figure 3.17. The voltage source is considered ideal and the coil resistance is neglected.

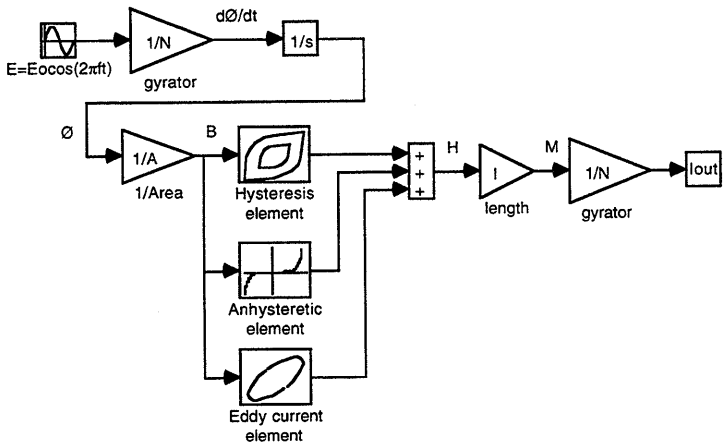

Figure 3.17. SIMULINK® block diagram of a ferromagnetic system including saturation, hysteresis and eddy current losses. The block labeled "Hysteresis element" is shown in Figure 3.12. The block labeled "Eddy current element" is shown in Figure 3.7. The "Anhysteretic element" is a SIMULINK® Look Up Table linear interpolation block.

This simulation has incorporated the hysteresis and eddy current models described previously into the appropriately labeled sub-system blocks. Each sub-system block requires the input of all the various material-dependent data. In addition, the eddy current and hysteresis blocks need to know the excitation frequency.

In order to evaluate the fidelity of the simulation, it is necessary to have a database from testing for comparison. Magnetic loss data for a grain-oriented silicon-iron material, Trafoperm N2, is published [4] for the frequency range of 50 Hz to 10 kHz at excitations from 0.01 Tesla to over 1.5 Tesla for a variety of thicknesses. A set of low frequency hysteresis loops is also given in this reference. With this data, it should be possible to extract an approximate anhysteretic curve, develop a reasonable model, and assess the simulation accuracy.

An approximation to the anhysteretic curve is obtained, as discussed above, by averaging the left and right sides of the major hysteresis loop. The other parameters for simulation are derived by adjusting for a reasonable fit to the published data at the extreme conditions of concern. At low frequencies hysteresis losses tend to dominate, so a reasonable hysteresis simulation (b, k) should give a fair approximation of total losses. At high frequencies, eddy current losses become more important (k_e). The simulation will hopefully track the data at intermediate frequencies reasonably well. The variation of the shape of the hysteresis loop with flux density magnitude can be introduced by the k_f factor.

Note that in the calculation of the skin depth $\delta = \sqrt{\rho/(\pi f \mu)}$, the permeability has the same influence as the frequency. As the material begins to saturate, the effective permeability must drop, somewhat increasing the skin depth and reducing the eddy current losses. At the same time, the anomalous losses (not modeled accurately) will increase. Thus, the assumption of constant permeability will somewhat compensate for the lack of accurate modeling of the anomalous losses. It will be necessary to select an effective permeability which gives total losses similar to test results at various frequencies. In these simulations, a value of μ_r = 4000 has been used for the Trafoperm N2 simulation.

For the simulation of 0.30 mm thick N2 lamination, the material data is set up in a MATLAB® script file which is called by the simulation program. This script file, 'N2data.m' is shown in Appendix E, along with similar files for other materials. The parameters in this file were established by a simply matching the published N2 data.

First, the low frequency (50 Hz) hysteresis loop is simulated. b is chosen to roughly match the shape of the loop, here a fairly rectangular shape. To estimate k and k_f, the width of the loop is to be matched. In this particular case, the variation of loop width as a function of maximum flux density is given in the reference. Computing the values of k and k_f is done using a simple linear regression for the relationship of loop width to $|B|$ (equations 3.19 and 3.20) after subtracting the effect of eddy current losses. The relevant parameter values are $b = 0.03$, $k_f = 3.41$, $k = 3.05$. The result at a flux density of 1.6 T is shown in Figure 3.18.

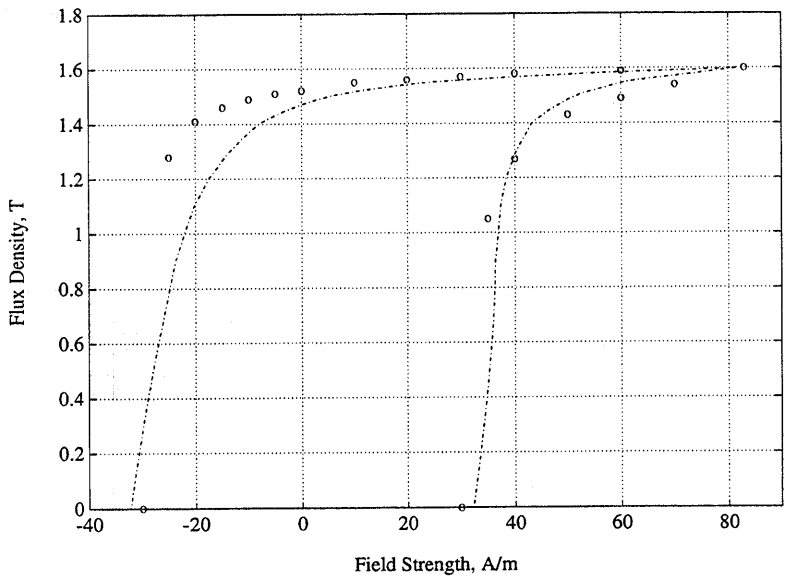

Figure 3.18. Simulated 50 Hz hysteresis loop for Silicon-iron 0.30 mm thick.
o - published data point for Trafoperm N2 [4]

The simulation of the N2 hysteresis loop does not match published data quite as closely as the previous example using AISI 1018 steel. The measured power loss in traversing the Figure 3.18 loop at 50 Hz is 1.28 W/kg. This is to be compared with the simulated power loss of 1.22 W/kg. However, other data from the same source [4] records a power loss under the same conditions of 1.10 W/kg. This data variation is typical of magnetic loss measurements made on different specimens or with different test setups. Unless simulating the exact shape of the loop is critical, this simulation could be considered quite reasonable for both measurements.

Now the fidelity of the simulation can be confirmed by comparing data at other excitations and frequencies. Figure 3.19 compares the simulated total loss of 0.3 mm Trafoperm N2 to the published loss data. Matching high frequency data is assisted by choosing a value for the anomalous loss coefficient. In this case, $k_e = 1.3$ seems to give good results to 400 Hz.

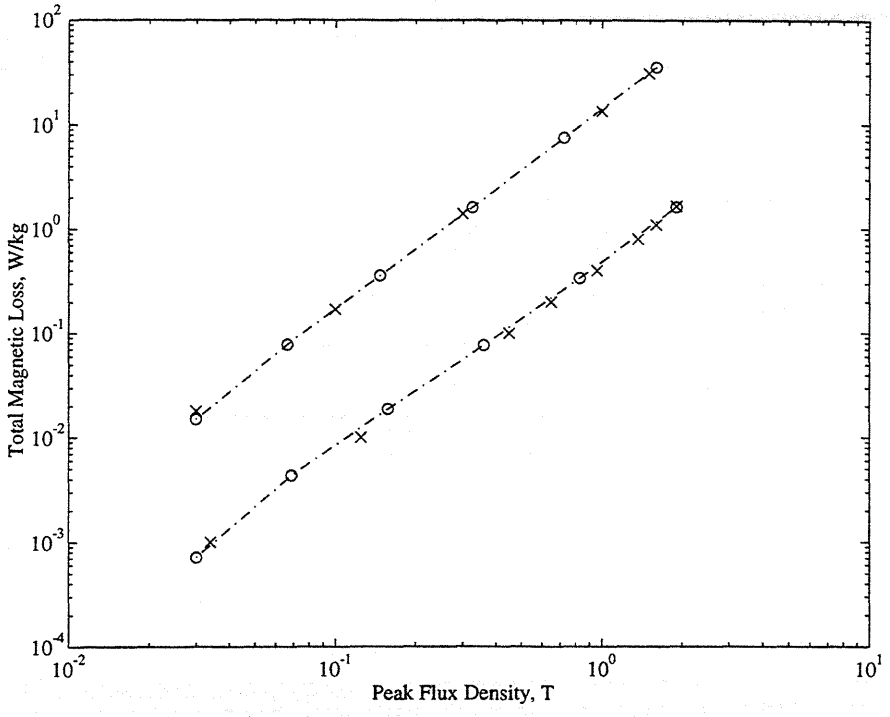

Figure 3.19. Total magnetic losses for 0.30 mm Trafoperm N2 at 400 Hz (upper curve) and 50 Hz (lower curve). o - Simulated x - published data point for Trafoperm N2 [4]

Figure 3.19 shows how well results correlate when matching both the 50 Hz dynamic hysteresis curves and the power loss measurements provided by the reference. When the dynamic curves are not available, a good prediction of total losses can still be made based on approximately representing the static hysteresis loop.

For example, a simulation of 0.1 mm thick Trafoperm N2 material over the frequency range of 400 Hz to 5 kHz was run. For this simulation, the parameters from the previous simulation are adjusted to match the published power loss characteristics of the thinner material. Generally, material thickness will have some small effect on hysteresis loop shape and the anomalous loss coefficient because of different processing.

In determining the various parameters, it is important to remember that low frequency losses are principally a function of the hysteresis loop; as the frequency increases, the relative importance of the eddy currents becomes dominant. Figure 3.20 presents the results of the simulation optimized to match the published power loss data [4]. The material data parameters ('N2dat1.m' in Appendix E) are $b = 0.03$, $k_f = 3.4$, $k = 4$, and $k_e = 1.5$.

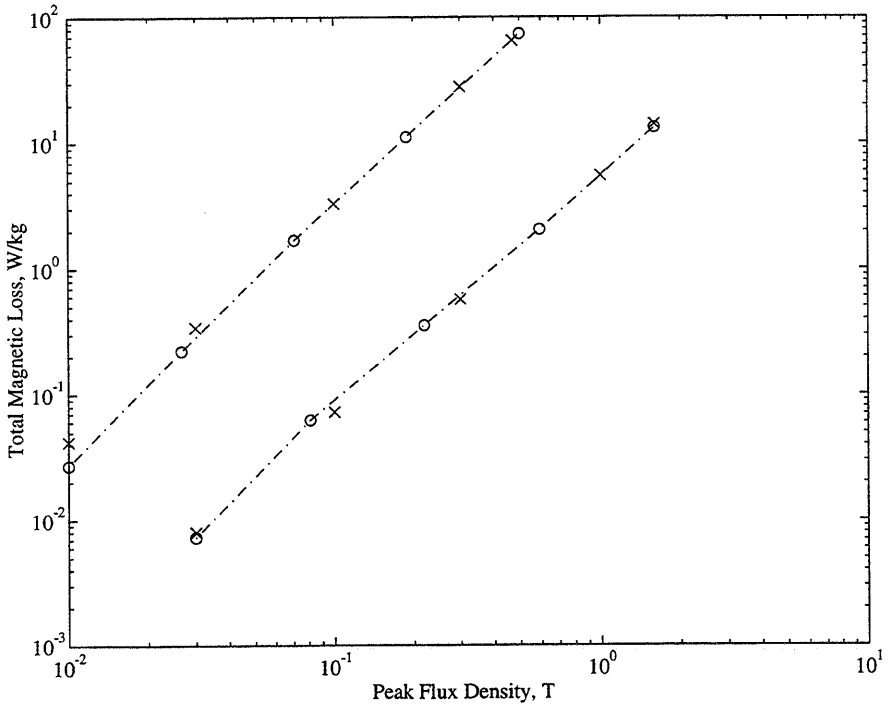

Figure 3.20. Total magnetic losses for 0.10 mm Trafoperm N2 at 5000 Hz (upper curve) and 400 Hz (lower curve). o - Simulated x - published data for Trafoperm N2 [4]

A reasonable model of a magnetic element has been demonstrated. In the next chapter, the magnetic element model will be applied to the model of the Sawyer linear motor.

Chapter 4

A model of the Sawyer motor with non-linear magnetic elements.

In Chapter 2, a model of the Sawyer motor was developed which neglected ferromagnetic path reluctance and non-linearities. Applying the ferromagnetic element models developed in Chapter 3 to every flux path in the motor is possible, but would entail a large computing burden. The approach in this chapter is to make a rough assessment of where magnetic losses occur in the system, then use this information to decide which ferromagnetic elements to add to the motor model. Next, the non-linear ferromagnetic elements are added to the simple motor model. Finally, the enhanced motor simulation is run and the simulation data presented.

4.1 Estimating magnetic path losses

A spreadsheet analysis was used to roughly calculate which ferromagnetic elements to include in a more detailed motor model and which elements might be neglected. The spreadsheet uses traditional "handbook" methods to estimate losses from hysteresis and eddy currents in the principal flux path parts of the motor.

The classical eddy current power loss in a ferromagnetic lamination [6, 8, 22] is

$$P_e = \frac{(\pi f d B_m)^2}{6\rho} V. \tag{4.1}$$

In this formula, V is the volume of flux carrying element, d is the thickness, B_m is the flux density amplitude, f is the frequency and ρ is the conductivity of the ferromagnetic material. The effects of frequency, thickness, and maximum flux density are to the second power.

To estimate the hysteresis loss, the Steinmetz law [9] is applied. In SI units the hysteresis power loss in the volume V is

$$P_h = 2.51 \cdot 10^5 \, \eta f \left(B_m\right)^{1.6} V. \tag{4.2}$$

The Steinmetz coefficient, η is tabulated [17] for the various materials. For a low loss laminated electrical steel $\eta \approx .0005$, and for low carbon steel, $\eta \approx .009$.

These two relationships are applied to the four major structures of the motor:

(1) Platen
(2) Platen teeth
(3) Forcer pole
(4) Forcer teeth

Losses in each flux-carrying part can be estimated on a per pole basis and the relative magnitudes compared. For the platen, the loss estimates were modified due to the extreme thickness of the material, relative to the skin depth. The effect of eddy currents in such a thick part at high frequency is to effectively shield the interior of the part from the magnetic field. Equation 4.1 suggests that for a given flux density and frequency, the eddy current power loss will increase indefinitely as the cube of the thickness. Intuitively, it appears that this will not be the case. At high frequency (skin depth small relative to the thickness) total power loss should not change as the part thickness increases. One of the key assumptions made in the derivation of equation 4.1 [3, 9] is that the flux is uniform throughout the thickness of the material, thus some modification is appropriate.

The alternate power estimate for the platen was obtained by calculating losses assuming a part only 6 skin depths (= 6δ) thick. Six skin depths includes approximately 95% of the flux carrying layers (top and bottom) in the classical eddy current model (constant permeability). The skin effect flux concentration increases the relative magnitude of the flux density, and reduces the effective flux path volume. The net effect is to increase the hysteresis loss estimate and reduce the eddy current loss estimate.

The spreadsheet calculation was performed using an arbitrarily assumed peak flux density in the motor of 1.4 Tesla. The spreadsheet is shown in Appendix F. The results (in watts) are summarized in Table 4.1 for two frequencies. The relative value of the losses, not the absolute magnitude, is of significance.

	100 Hz		1 kHz	
Flux path element	Total Loss (W)	Hysteresis loss (% of total)	Total Loss (W)	Hysteresis loss (% of total)
Platen structure	4.0	6	40.6	5
Platen teeth	0.03	86	0.3	43
Forcer structure	0.05	74	0.5	27
Forcer teeth	0.002	69	0.03	22

Table 4.1. Estimated losses in motor flux path elements, per pole.

The same spreadsheet was used to estimate the magnitude of mmf "drop" across the same elements. These mmf values (in amperes) have been tabulated in Table 4.2.

	100 Hz	1 kHz
Flux path element	mmf drop (A)	mmf drop (A)
Platen structure	4.87	15.23
Platen teeth	1.27	0.41
Forcer structure	0.73	0.49
Forcer teeth	0.12	0.02

Table 4.2. Estimated mmf in motor flux path elements, per pole.

It is clear from this analysis that the magnetic losses and mmf drop occur predominantly in the platen structure. Also evident is that the losses in the platen are principally a result of eddy currents as opposed to hysteresis. Even relatively large errors in this calculation would not affect these conclusions.

4.2 Adding magnetic losses to the motor model

The preceding section showed that it is most important to add the platen structure magnetic losses to the motor model. Referring to the motor diagram, Figure 1.1, three segments of the platen are active in the flux path. The active platen flux path includes a segment connecting pole 1 to pole 2 (denoted RC_{12}), a segment connecting pole 2 to pole 3 (RC_{23}), and a segment connecting pole 3 to pole 4 (RC_{34}). The notation RC indicates an R - C field which includes the eddy current, hysteresis and saturation effects discussed in the previous chapter. A bond graph segment combining the three effects is shown in Figure 4.1.

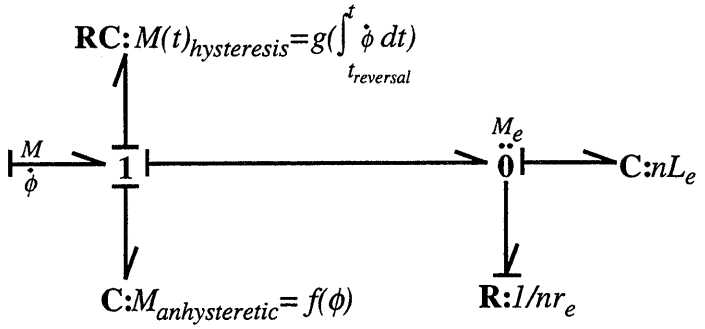

Figure 4.1. Bond graph segment representing a ferromagnetic R - C element.

In this bond graph segment, there are three components contributing to the mmf at a ferromagnetic element. $M_{hysteresis}$ is the hysteresis mmf described by equations 3.19 and 3.20. M_e is the mmf resulting from eddy currents. The eddy current mmf per unit length is expressed by equations 3.17 and 3.18. That portion of the mmf which is conservative is called $M_{anhysteretic}$. This mmf defines the saturation characteristic and, as described in Section 3.2, will be defined by a look-up table or function fitted to the actual (or estimated) anhysteretic curve.

Consider the motor model developed in Section 2.7. The bond graph of Figure 2.10 incorporated air gap reluctances at each pole. To modify this model, non-linear ferromagnetic elements of the type developed in Chapter 3 will be added. By inspection, the ferromagnetic segments connecting to pole 1 (RC_{12}) and pole 4 (RC_{34}) carry the same flux as those poles. Therefore, these can be incorporated at the same -1- junctions as the air gap reluctances, R_1 and R_4. All flux passing through the ferromagnetic segment, RC_{23} must also pass through the permanent magnet. Thus, RC_{23} should be inserted at the -1- junction with permanent magnet reluctance R_m. These additions do not alter the causality. The modified bond graph is shown in Figure 4.2.

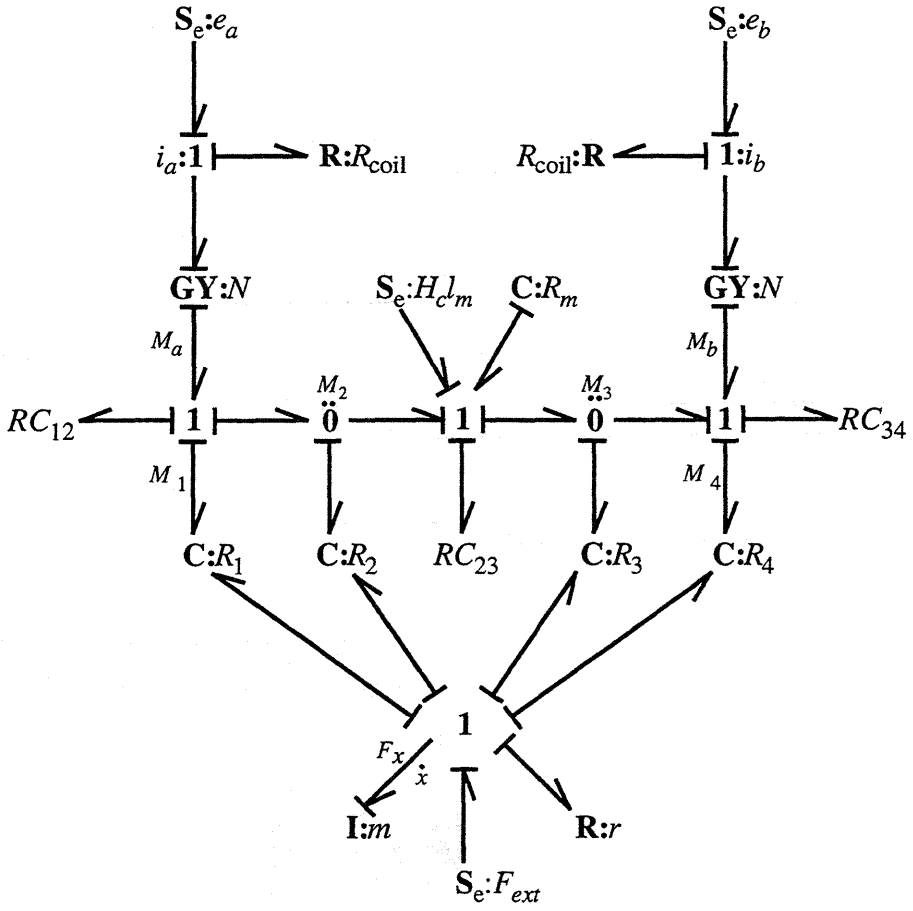

Figure 4.2. Motor system bond graph with voltage driven causality and platen ferromagnetic loss elements.

4.3 Equations for the motor model with magnetic losses

The basic structure of the model shown in Figure 4.2 is the same as the model shown in Figure 2.10. It follows, therefore, that the equations for the motor will be similar to those in Section 2. Equations 2.12, 2.26, and 2.33 through 2.38 can be modified to add the loss model elements.

The mmf at each coil is determined from the junction structure and the fluxes; therefore,

$$M_a = (R_1 + R_2)\phi_1 + M_{RC}(\phi_1) - R_2\phi_m, \tag{4.3}$$

$$M_b = (R_3 + R_4)\phi_4 + M_{RC}(\phi_4) - R_3\phi_m, \tag{4.4}$$

where $M_{RC}(\phi_n)$ is the mmf resulting from the ferromagnetic R - C element model with flux ϕ_n.

The permanent magnet flux cannot be determined algebraically. This is because there is no closed form expression for the inverse of the $M_{RC}(\phi_n)$ relation. The permanent magnet flux is expressed implicitly as

$$\phi_m = \frac{R_2\phi_1 + R_3\phi_4 + H_c l_m - M_{RC}(\phi_m)}{R_m + R_2 + R_3}. \tag{4.5}$$

As before, the rates of flux change in the coils are equal to the coil voltage divided by the number of turns, where the coil voltage has been reduced by a loss across the coil resistance.

$$\dot{\phi}_1 = \frac{e_a - R_{coil} i_a}{N} = \frac{e_a}{N} - R_{coil}\frac{M_a}{N^2}, \tag{2.36}$$

$$\dot{\phi}_4 = \frac{e_b - R_{coil} i_b}{N} = \frac{e_b}{N} - R_{coil}\frac{M_b}{N^2}. \tag{2.37}$$

Equations (2.36) and (2.37), together with (4.3), (4.4), and (4.5), form the state equations for ϕ_1 and ϕ_4. The fluxes at the other two poles remain dependent;

$$\phi_2 = \phi_1 - \phi_m, \ \phi_3 = \phi_m - \phi_4. \tag{2.38}$$

The other state equations are also exactly as before, with the fluxes determined from equations (2.36-2.38).

$$\dot{p} = -\frac{1}{2}\Phi^T \frac{\partial}{\partial x}\mathbf{R}(x)\Phi - r\frac{p}{m} + F_{ext}, \tag{2.26}$$

$$\dot{x} = \frac{p}{m}, \tag{2.12}$$

Although it would appear from the preceding equations that the system order is unchanged at 4 state variables (identical state equations as in Section 2.7), these equations have been modified by equations 4.3, 4.4, and 4.5. Each of those equations contains a relation $M_{RC}(\phi_n)$ which adds states because of the hysteresis memory and the eddy current model. It is also important to recognize that the model itself varies somewhat with excitation frequency, as discussed in Chapter 3.

There is still a need to calculate the initial conditions on the fluxes to avoid a transient at the start of the simulation. These initial conditions are a function of pole reluctance at the initial motor position, $x(t_0)$, and the permanent magnet mmf. However, because the permanent magnet flux cannot be explicitly calculated, an alternative way of establishing the initial conditions must be established. This will be accomplished with the simulation.

4.4 Simulation of the motor with platen magnetic losses

Equation 4.5 expresses the permanent magnet flux as a function of the mmf resulting from this same flux passing through a ferromagnetic element model. Solving for this flux cannot be done in closed form. Attempts to resolve this situation using simple iteration usually end in frustration because the effect of hysteresis does not permit going backward in time without reversing the flux and modifying the "memory" of hysteresis. Another approach might be to use a "shooting" type of trial and error method. This would involve assuming a new permanent magnet flux, calculating the fluxes and comparing the resulting permanent magnet flux to the assumed flux. Each trial would require resetting all of the conditions to the initial state prior to the iteration, until the required accuracy is met. This type of method could significantly slow down a simulation.

The approach chosen here is to simply use the permanent magnet flux from the previous time step. Thus, the error is simply determined by the size of simulation time steps. The disadvantage of this method is that the errors may accumulate and grow larger with time, giving inaccurate results. In addition, large time steps relative to the rate of change of the system states can result in an unstable simulation.

To calculate the initial conditions on the fluxes, the permanent magnet's mmf (Hclm) will be ramped from zero to its steady state value. This is done prior to the beginning of the simulation proper, i.e., before any of the other inputs are varied. When the permanent magnet mmf has reached its steady state value, the simulation may begin without risk of a large startup transient.

Figure 4.3a shows the SIMULINK® block diagram construction of the problem described by the above equations. The blocks "Air gap reluctance", "Magnetic Force" remain as shown in Figure 2.3. The blocks "Sine drive" remain as shown in Figure 2.11.

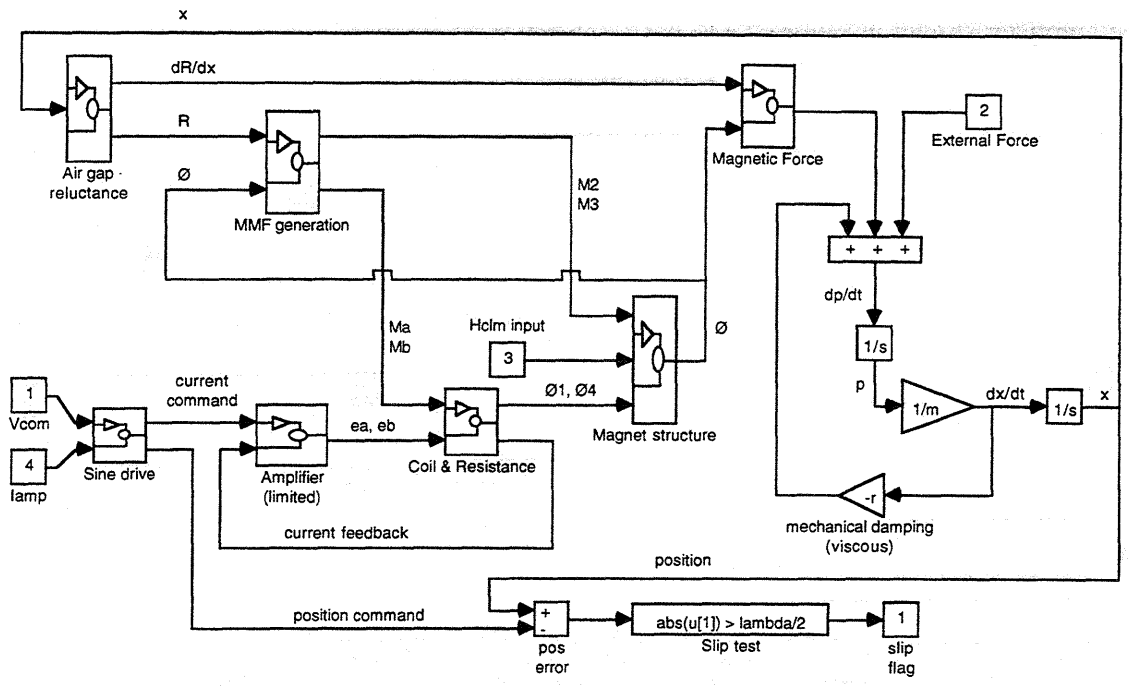

Figure 4.3a. SIMULINK® block diagram of the motor with magnetic loss elements.

For simplification of the overall diagram, the flux rate integrators have been grouped together with the gyrator and coil resistance. The revised block is shown in Figure 4.3b.

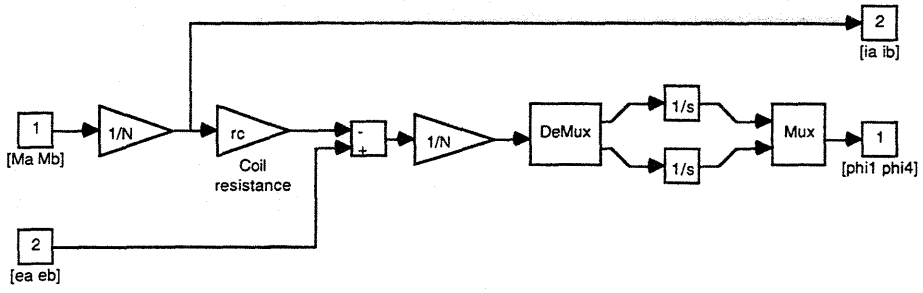

Figure 4.3b. "Coil & Resistance" block diagram includes coil gyrator plus flux rate integration.

The amplifier shown in Figure 2.11b has a saturation block which limits the output voltage. This "hard stop" on the output is not entirely realistic and does not provide current limiting. Simply stated, the output impedance was modeled as zero right up to the voltage limit. In reality, an amplifier can only maintain voltage if current output is within its capacity. The block diagram of Figure 4.3c adds a "variable saturation" feature which reduces the maximum output voltage as the current rises beyond a specified limit. Here the voltage is always limited to 170 volts by the saturation blocks labeled VsatA and VsatB. The current is limited by setting another voltage limit ("variable saturation") which varies as the current approaches the limit of 3.5 amps. In this case, when the current exceeds 3.0 amps, the voltage limit is reduced below 170 volts. At 3.5 amps and above, the voltage limit is zero. This "soft" current limiting feature makes the amplifier response more realistic and helps to stabilize the simulation when operating near these limits.

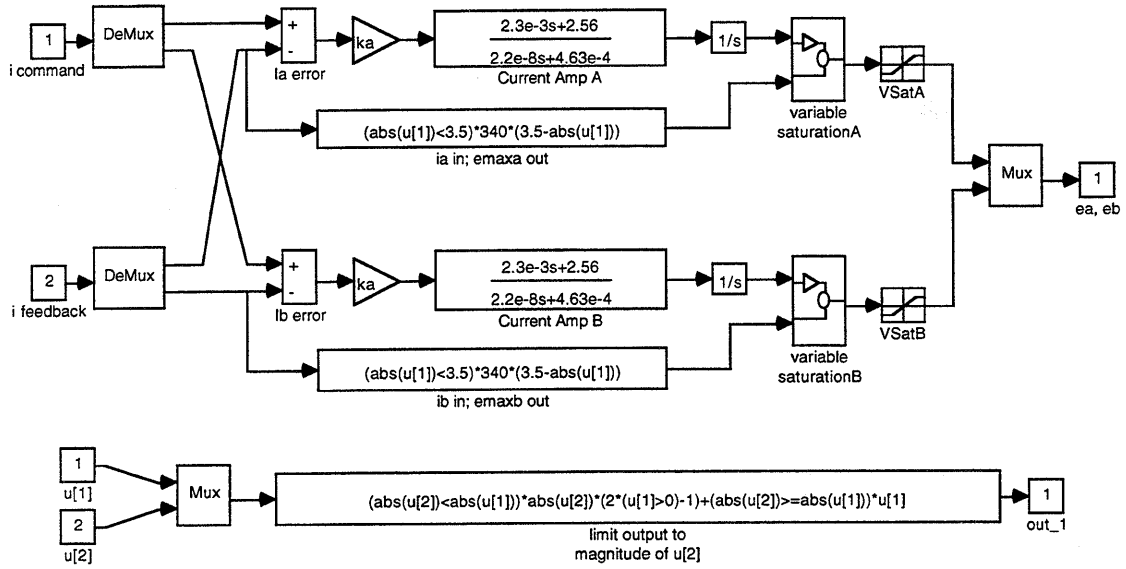

Variable Saturation

Figure 4.3c. Details of "Amplifier (limited)" block. "Variable saturation" block detail shown at bottom of figure.

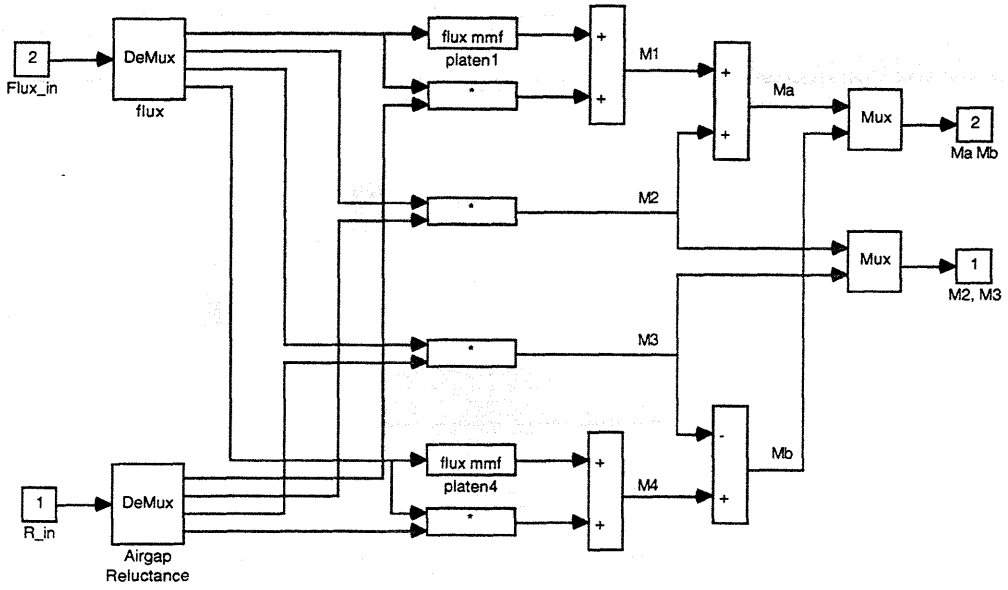

Figure 4.3d. "MMF generation" block. This block calculates system mmf from the flux and reluctance inputs. The subsystem blocks labeled "platen" are the ferromagnetic element models.

The software program offers a "memory" function, shown as a transport delay block in Figure 4.3e. This function is set to delay the input by one time step; i.e., the output is equal to the previous input. Inserting one of these blocks into the path feeding the permanent magnet flux to the system effectively forces the program to ignore the algebraic loop which would otherwise invoke the undesired iterative solution.

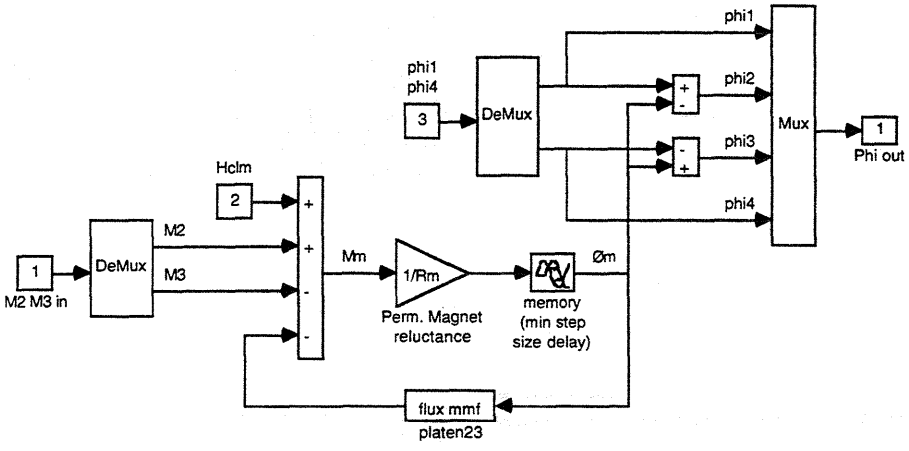

Figure 4.3e. Details of "Magnet structure" subsystem block. The subsystem block labeled "platen23" represents a ferromagnetic element model.

In Figure 4.3, the ferromagnetic element subsystems are labeled as "platen". Figure 4.4 shows the detail of this element. The details of the sub-elements within this block are described in Chapter 3.

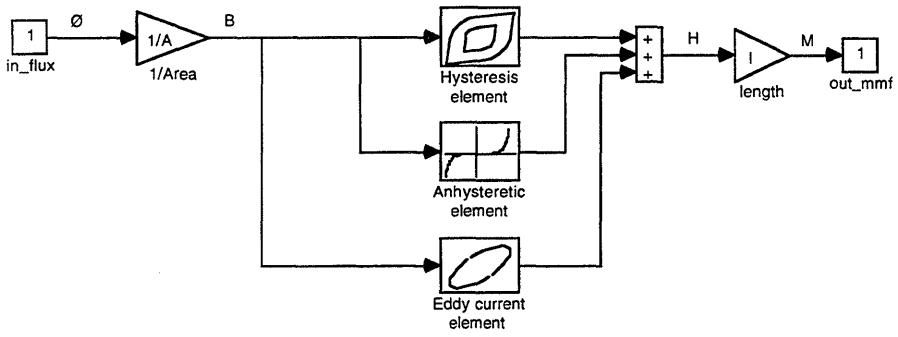

Figure 4.4. Ferromagnetic element subsystem block diagram "platen".

A MATLAB® script file controls the simulation, setting the inputs, the initial conditions, and the simulation parameters. The script file, '`rmrun4`', is shown in Appendix E.

4.4.1 Simulation Results: Power dissipation

The motor simulation was run at 100 and 1000 Hz to check against the hand calculations done in Section 4.1. In each case the motor was simulated to accelerate to the commanded velocity without a load (no external force). Once the steady state velocity was reached, the power consumption of the motor during constant speed running was calculated from the simulation output. The total power in each of the magnetic elements and the hysteresis loss were determined separately. For completeness, the power dissipated in the winding resistance and the friction loss were also calculated. All of the power calculations were done post-simulation using the '`power`' function described in Appendix E.4. The results are shown in Table 4.3.

	100 Hz (0.1 m/sec)	100 Hz no hysteresis	1 kHz (1.0 m/sec)	1 kHz no hysteresis
Loss element	Power (W)	Power (W)	Power (W)	Power (W)
Platen (RC_{12})	8.95	8.92	32.3	32.7
% Hysteresis loss	1.4%	0	0.6%	0
Platen (RC_{23})	0.01	0.01	0.18	0.17
Coil Windings (each)	7.4	7.4	6.4	6.4
Friction	0.001	0.001	0.1	0.1
Total motor power (all elements)	32.7	32.6	77.7	78.2
Simulation time (sec)	23	16	50	22

Table 4.3. Simulated losses in various elements during motor simulation of constant velocity operation. Power values shown are mean power. (Note that platen elements at poles 1 and 4 will be the same.)

For the platen, the simulated power is the same order of magnitude as the spreadsheet calculation shown in Table 4.1. The hysteresis loss as simulated is about one-half as much at 100 Hz and one-tenth at 1000 Hz. This is partially explained by the fact that the Steinmetz calculation assumes a traditional bipolar magnetic excitation. In the Sawyer motor flux is biased by the permanent magnet. Thus, flux excursions are not bipolar and the area swept in the hysteresis loop is somewhat less than half. Another explanation for the reduced hysteresis loss in simulation is that the simulation resulted in a lower peak flux density (0.6 T at 1 kHz) than that assumed in the hand calculation (1.4 T).

The above results suggest that in this case the inclusion of the hysteresis loss does little to enhance the simulation. By eliminating the hysteresis loss in the simulation, the computational effort is reduced. The data from simulations when the hysteresis loss element is removed from the computer model support this conclusion. Table 4.3 shows that the results obtained are very similar. Figure 4.5 is a plot of a motor acceleration to 1.0 m/sec with and without hysteresis simulation. The two curves are indistinguishable at this resolution. In the next section, the simulation will be run without hysteresis to produce force versus velocity plots.

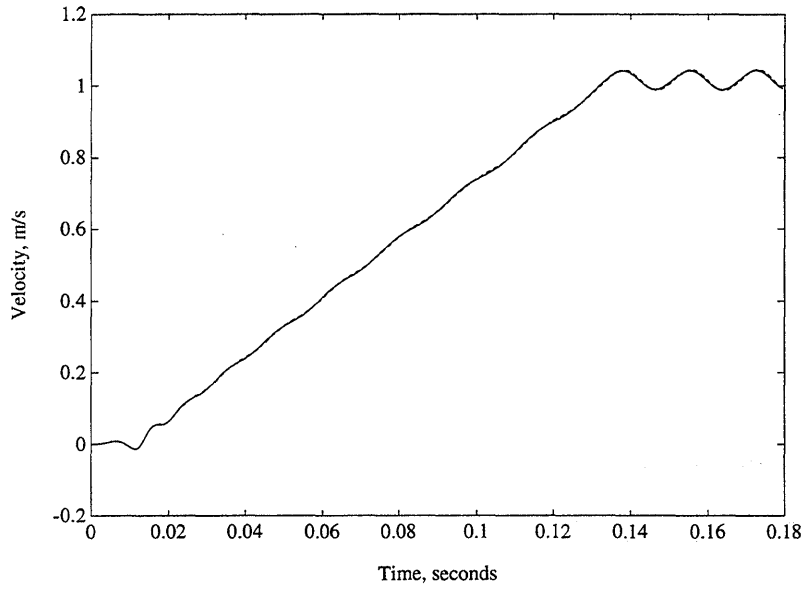

Figure 4.5. Simulated motor accelerations from 0 to 1 m/sec. Curves with and without hysteresis are superposed.

4.4.2 Simulation results: motor force production

Figure 4.6 shows the system response to an initial displacement of $\lambda/4$.

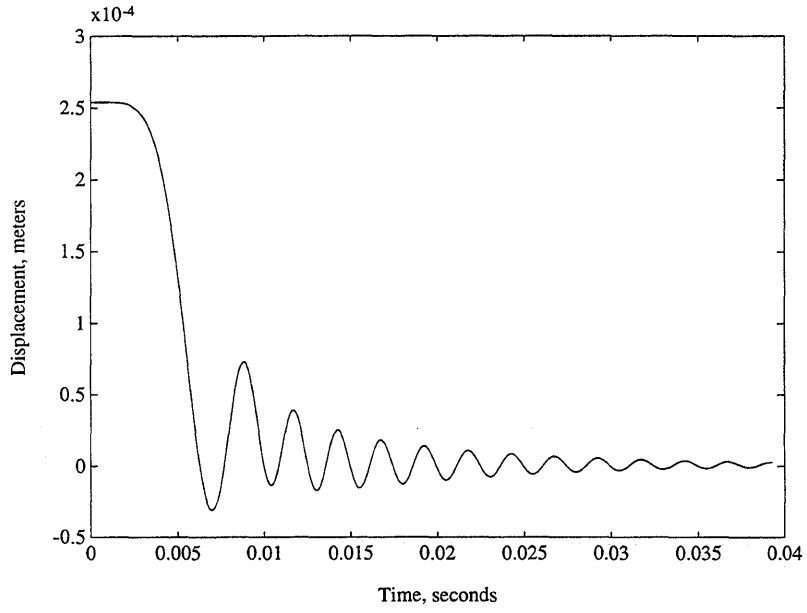

Figure 4.6. Response to initial displacement of motor with a commanded velocity of zero.

Figure 4.7 is the shows the force production of the motor as a function of velocity, the 'pull-out' curve.

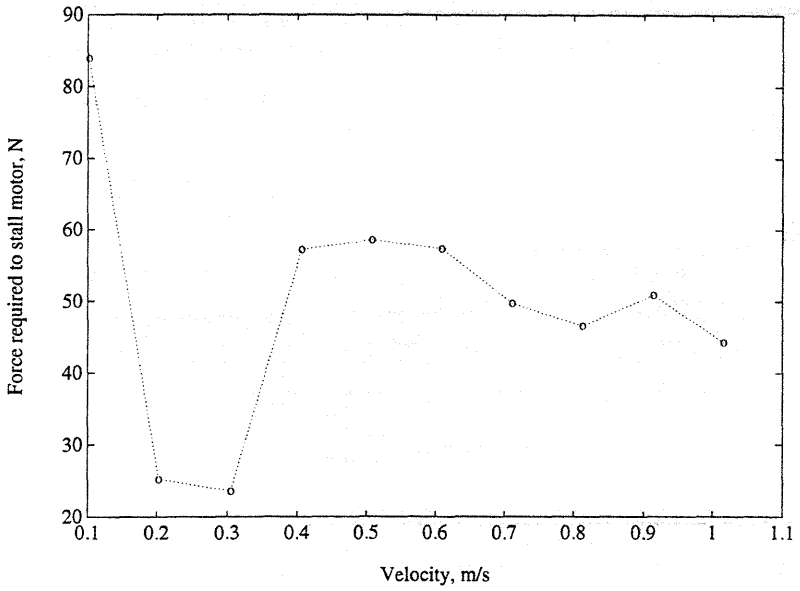

Figure 4.7. Dynamic (pull-out) force versus velocity with a 2 kg forcer mass.

This model indicates motor instability for some combinations of motor mass and velocity. Oscillations in motor velocity will increase to the point where the motor slips out of synchronization, even without external force. This unstable behavior is characteristic of a stepper motor and is similar to that seen with the simple model of Chapter 2. In the present model, however, the phase shifts associated with the eddy current dynamics and/or the delay element (needed to eliminate the algebraic loop) appear to significantly reduce the stability of the system. Leenhouts [18] describes this as "negative damping", i.e. an increase in velocity results in a decrease in drag force. It was found that a mass payload of about 2 kg stabilizes the model for the velocity range shown in Figure 4.7. Even with the stabilizing mass, the motor force output is poor at low speeds.

In order to stabilize the motor for general load conditions, the approach recommended by Leenhouts [18], and Compumotor [24] is taken. The idea is to increase the effective positive damping by using the velocity error of the motor to shift the phase of the winding currents. A negative velocity error indicates that the motor needs to accelerate. To increase the force applied, the position command is phase delayed by an amount proportional to the velocity error. A modified model, shown in Figure 4.8, adds this feedback feature.

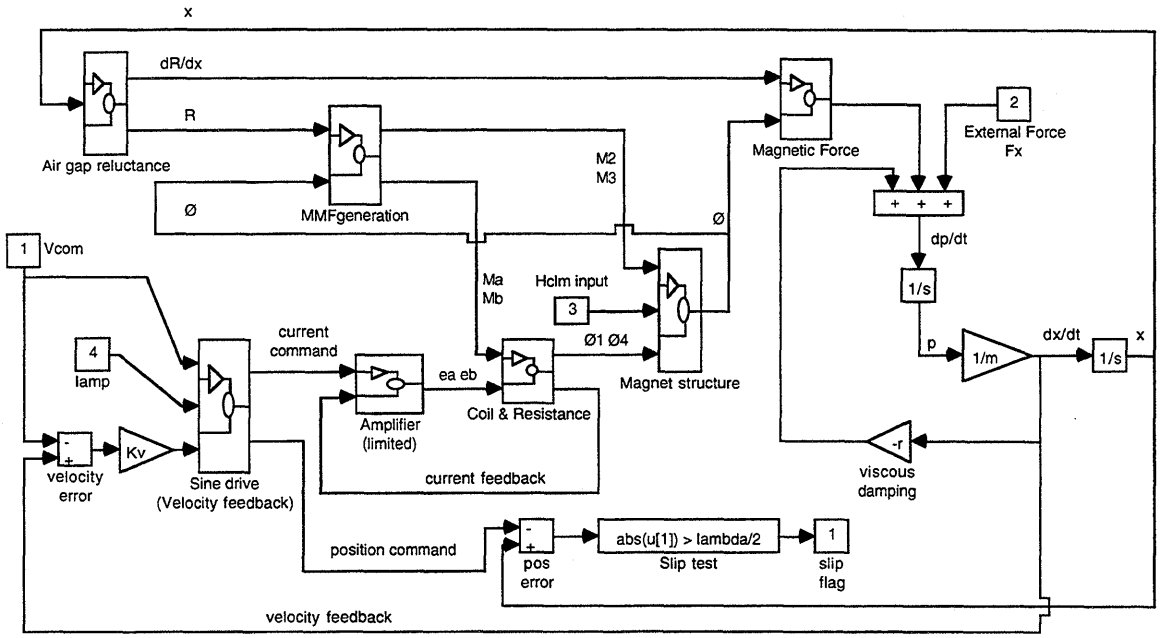

Figure 4.8a. Computer model of system with magnetic losses, modified to include velocity feedback.

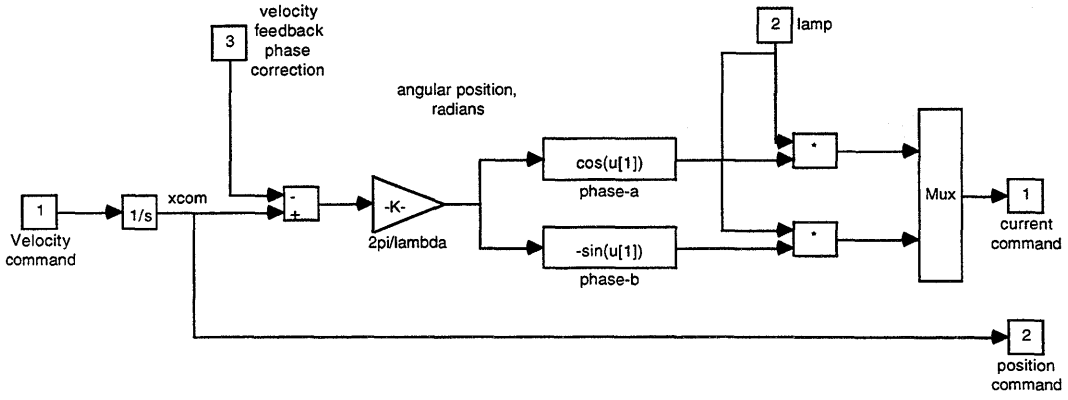

Figure 4.8b. Modified 'Sine drive' block incorporating velocity feedback.

Trial and error was used to determine a value of the proportionality constant, K_v=0.002 that gave good results over a reasonably wide range of velocities. Figure 4.9 shows accelerations to 1.0 m/s with and without velocity feedback damping.

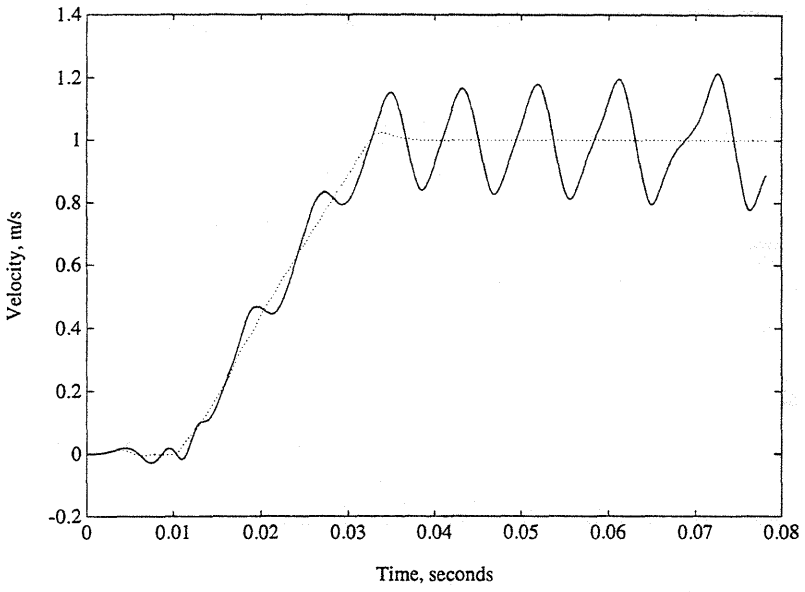

Figure 4.9. Comparison of acceleration transients to 1.0 m/s with velocity feedback damping of K_v=0.002 (dotted line) and without damping (solid line) .

Figure 4.10 shows the pull-out force curve for the motor with damping. Above 1.7 m/s the motor simulation stalls before reaching the target velocity. It is possible that some force could be developed at higher velocity by judicious "tuning" of the damping constant, and a slower acceleration to the target velocity.

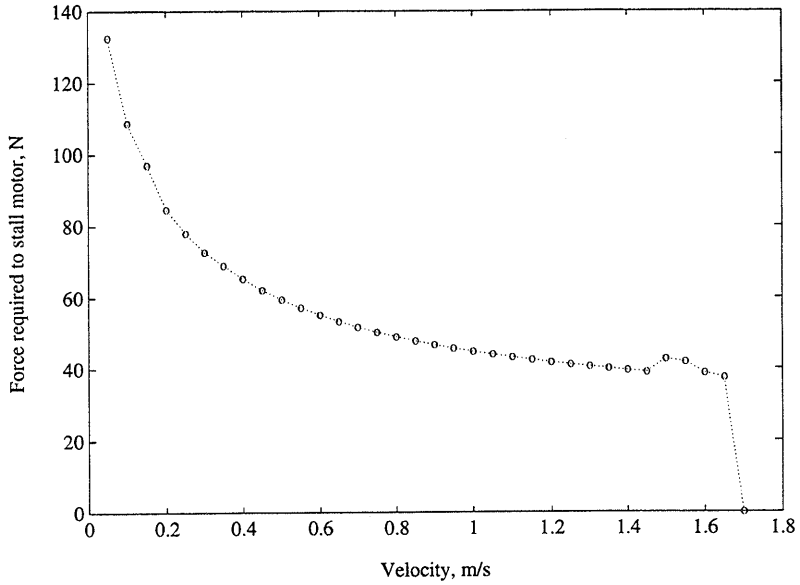

Figure 4.10. Dynamic (pull-out) force versus velocity with velocity feedback damping of K_v=0.002.

Chapter 5

Conclusions and Recommendations

In the preceding chapters, the design of a model for the Sawyer motor has been described. An energy-based method (the bond graph) was used to analyze the motor system and extract the operative equations. The equations were coded for computer simulation in the SIMULINK® block diagram format. The magnetic loss mechanisms, hysteresis and eddy currents, were analyzed and modeled using a combination of theory and empirical methods. The models of hysteresis and eddy currents were validated against published data. Finally, the relevant losses were identified and added to the motor system model and a simulation of the system was run. The simulation was used to predict such system parameters as force output, power consumption, and system instability.

In the course of these investigations, a number of issues arise which may warrant further investigation:

- Magnetic data is scarce on many general structural materials, such as the steel used for the platen in the commercial Sawyer motor. In this thesis, nominal or assumed values based on one test part were used for the simulations. In the manufacture of such materials there is little or no control of the magnetic properties. It may be worthwhile to see how the variation of the material could affect motor design and operation.

- Testing thick materials for losses could be useful to validate the eddy current model of Chapter 3 (no data was found to demonstrate the effectiveness of the model where the skin depth is much less than the material thickness). Further, in Chapter 4 it was assumed that the eddy current losses in thick materials was confined to the surface layers to a thickness limit of 6 times the skin depth. On this basis, the classical eddy current formula was used to make an estimate of the losses. This sort of estimating procedure was not encountered in the literature, although it seems reasonable and should be evaluated. Improvements to the model, particularly in the way that eddy currents concentrate the mmf in the surface of the material under test, may be identified.

- In Chapter 4, the hysteresis losses were estimated by classical methods and simulation to be insignificant. Because of this assessment, the hysteresis loss could be removed, and the motor model simplified. It would be very useful to develop simple calculations or guidelines which can enable the user to rapidly determine when to include hysteresis losses in a model. Such a method could involve input of parameters for estimating hysteresis and eddy current losses and operating frequency. A method developed to do this should somehow be validated against published data or by laboratory test.

- In some problems, it seems likely that neither hysteresis nor eddy current losses may be significant or important to the dynamic response. However, using the anhysteretic saturation model alone may still be of value to improve the accuracy of the mmf prediction. This is important because the mmf developed will determine the magnetizing current in the windings. Copper losses (i^2R) in the windings can become the dominant loss element in some motors. Design of an appropriate power source is also affected.

- Although the simulations described run for many conditions, the mathematical stability of these models varies with simulation parameters. Under some conditions, the models will not run, will run very slowly, or will generate enormous data output files. The parameters which affect the simulation include type of integrator, step size, error control, and noise filter time constants. The more recent versions (releases 1.3 and 2.0) of the SIMULINK® software were found to be progressively more efficient and reliable. Some amount of work could be done to determine the optimum parameter selection for fast and accurate simulation.

- In this model, a sinusoidal reluctance variation was assumed which gave reasonable results. It is not true that this will hold for motors in general, however. In cases where the magnetic path is very efficient, high levels of saturation can occur locally in the teeth at each pole. This saturation will modify the reluctance relationship. Instead of being a simple function of motor position, reluctance will vary with the magnetic flux and the position. Qishan and Jimin [27] have developed a tabulated approach to this problem which could possibly be integrated with the type of model presented here.

- Amplifier output was modeled as a controlled current or voltage. In reality, many of these drives are excited by high frequency (~15-100 kHz) pulse width modulated sources. The high frequency harmonic content of the output has not been accounted for. Also, the modeled amplifier was assumed to produce a "clean" sine wave output. In cost-sensitive applications a modified sine output (trapezoidal) or square wave may be desirable. The effects of these distortions should be added to the modeled response.

- Finally, complete motor response testing in any intended application will indicate additional improvements that could be made to this model. It may be possible to simplify the model for an intended application such that a very fast model can be run in real time. Such a model could be useful to developing an more effective motor control and monitoring system for improved performance.

Appendix A

The L20 linear motor

A.1 Description of the L20 motor [24, 25]

The L20 is a commercially available, 1-axis, 2-phase permanent magnet hybrid stepper motor. The forcer is supported over the platen on air bearings. Roller type bearings ensure axial alignment with the platen and provide some side load capability. The forcer itself consists of a pair of Sawyer type assemblies similar to Figure 2.1. The forcer assemblies are mechanically linked by the same structure, so that their forces add. In-phase windings of each element are series connected. The specifications apply to the dual forcer assembly.

A.2 Specification data for the L20 motor [24, 25]

The following parameters relevant to the simulations were extracted from catalog literature provided by Parker Compumotor of Rohnert Park, California:

Parameter	Value
Static Force	89.0 N
Static normal force	801 N
Current per phase	2.7 Amperes
Maximum forcer case temperature	75°C
Air gap (typical)	0.0005 in (12.5 microns)
Forcer weight (dual assembly)	0.8 kg
Platen material	AISI 1018 steel
Tooth pitch	0.040 in (1.02 mm)
Amplifier type	20 kHz fixed frequency, pulse width modulated; current controlled, bipolar type
Maximum resolution	12,500 steps/inch (125 microsteps/full step)

A.2.1 Performance curve

Parker Compumotor provides the following performance curve for the L20 motor system:

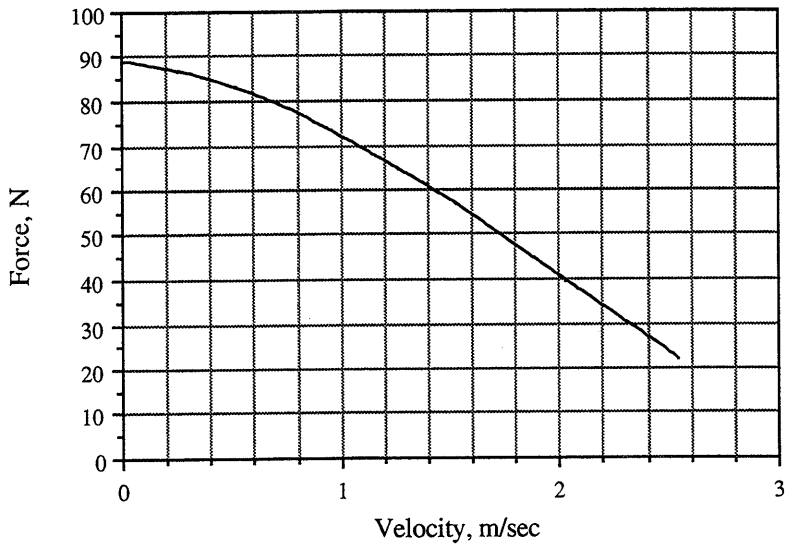

Figure A.1. Parker Compumotor L20 Force vs. Velocity Characteristic.

Appendix B

Air gap reluctance function

The variation of reluctance as a function of motor translation is a key determining factor of the force available at any given position of the forcer. The smoothness of motion will also be determined by the reluctance function. A common assumption is that the forcer reluctance variation can be approximated by a sinusoid. This assumption was evaluated experimentally. The actual magnitude of the air gap reluctance could not be obtained in this test. Instead, a method proposed and validated by Ward [1977] was used to calculate the air gap reluctance in the aligned and unaligned tooth positions.

B.1 Measured data

Air gap reluctance variation was determined by measuring the inductance of a coil placed in a magnetic circuit which included the toothed structure air gap. Segments of the L20 forcer and its platen were connected with the steel pole pieces to form a closed magnetic path. The space between the forcer and platen teeth was maintained at a fixed gap of approximately 0.0005 inches with a plastic shim. All other air gaps in the fixture were held to a minimum by bolting or clamping flat ground steel faces to each other.

The forcer part of the fixture was moved incrementally across the platen while the inductance of the magnetic circuit was monitored. A General Radio impedance bridge was used with a 1kHz sine wave to measure inductance. The position of the forcer was set with a micrometer and verified by dial indicator to within ±0.0002 inches. The results of the measurements are plotted in Figure B.1. A sinusoidal approximation to the data shows a fairly good fit.

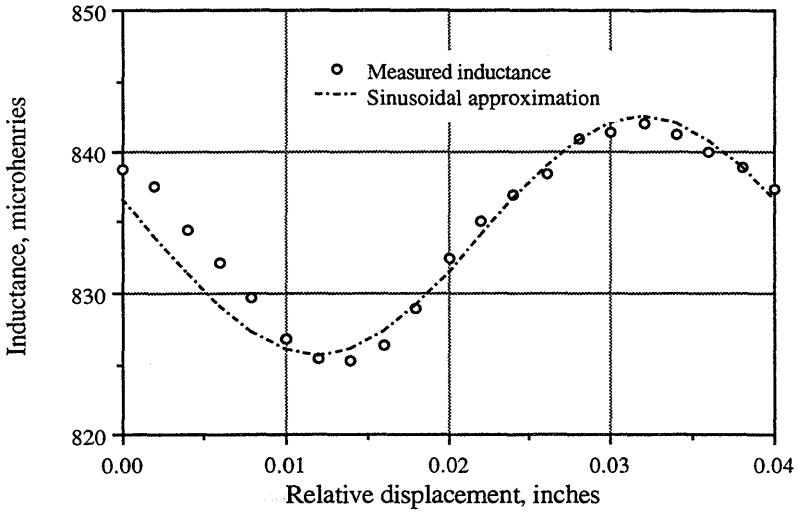

Figure B.1. Inductance of test magnetic circuit which includes air gap at motor poles. Also plotted is a sinusoid fitted to the data.

There are a few limitations to this result which should be mentioned. The data has some scatter due to the very low "quality factor" Q, of this magnetic circuit. ("Q" is a measure of the losses, or damping in the system. A low Q results in more difficult determination of the precise inductance.) Repeatability of the measurements is relatively poor because the measurement is sensitive to the precise alignment of the fixture and the variation of inductance is small.

The absolute value of the inductances measured here has no meaning. This is because the reluctance of the ordinary steel used in the magnetic path was large relative to the reluctance of the small air gap. What is important is that the variation of the reluctance is reasonably approximated by a sine curve.

For future work, it is recommended that a high permeability nickel alloy (preferably laminated) be used in the magnetic path. Also, a reference reading with zero gap could be used to remove the effect of the pole pieces in the path. Greatly improved resolution and accuracy should thus be attained.

B.2 Calculation of air gap reluctance

Using the method presented by Ward [1977], the minimum and maximum air gap reluctance can be calculated. The minimum reluctance will correspond to alignment of the forcer and platen teeth and the maximum reluctance will occur when the teeth are completely misaligned. Ward defines dimensionless parameters which, with the figures provided in his paper, allow the calculation of the reluctance at the two conditions. The variation of reluctance in-between the aligned and misaligned positions is assumed sinusoidal.

B.3 MATLAB® function to calculate reluctance

```
function [Rmax, Rmin] = rmaxmin (y, np, lambda, l)

% Function [Rmax, Rmin] = rmaxmin (y, np, lambda, l)
% rmaxmin is a function which returns the values of
% maximum and minimum gap reluctance given the gap, y;
% the number of teeth/pole, np; the pitch length, lambda;
% and motor length, l.
% The table is valid for t/lambda= 0.475 only.
% The method and the table are derived from the paper:
% "Magnetic Permeance of doubly-salient airgaps"
% by P.A. Ward et.al., Proc IEE. Vol 124, No. 6, June 1977
% Two significant figures only because the table was
% interpolated from a graph.

mu0 = pi*4e-7; % Permeability of free space (air)

Rg = y/(mu0*np*lambda*l); % Unslotted airgap reluctance, A/Wb

% kitab(:,1) is the value of pitch/gap = lambda/y
% kitab(:,2) is the value of ki, where Rmin=Rg/ki
kitab = ...
  [20.0000    0.5807
   25.0000    0.5642
   30.0000    0.5523
   40.0000    0.5376
   50.0000    0.5276
   60.0000    0.5212
   70.0000    0.5147
   90.0000    0.5074
  120.0000    0.5010
  150.0000    0.4973
  200.0000    0.4918];

% kotab(:,1)is the value of pitch/gap = lambda/y
% kotab(:,2) is the value of ko, where Rmax=Rg/ko
kotab = ...
  [20.0000    0.3023
   25.0000    0.2551
```

```
   30.0000    0.2214
   40.0000    0.1764
   50.0000    0.1472
   60.0000    0.1247
   70.0000    0.1101
   90.0000    0.0876
  120.0000    0.0663
  150.0000    0.0539
  200.0000    0.0404];

% Use Matlab's interpolation function to determine ko and ki
ko = table1(kotab, lambda/y);
ki = table1(kitab, lambda/y);
Rmax = Rg/ko;
Rmin = Rg/ki;
```

Appendix C

MATLAB® listings (simple motor)

C.1 Simple motor simulation script (smotl20.m)

```
% smotl20 is a Matlab program to run a simulation of the L20 linear
% stepper motor, with an ideal current source drive,
% neglecting the air bearing.  The program keeps track of motor
% position tracking and sets a flag if the motor slips out of sync.
% External force applied to the motor when it slips plotted vs
% commanded velocity (Fslip) is the motor's "pull-out" curve.
% X is the state vector
% X = [x p]' where x is postion and p is linear momentum
clear, format compact

% This section establishes the initial conditions,
% the physical constants and L20 motor parameters

  lambda = .040*.0254; % tooth pitch, m
  y = 0.0005*0.0254; % airgap at pole, m
  np = 6; % number of teeth/pole
  l = 1.965*0.0254; % length of motor, m
  N = 58; % number of turns on coils

  mf = 0.3; % approximate mass of single forcer, kg
  mp = 0; % mass of payload, kg
  m = mf + mp  % moving system mass, kg
  r = 66.5 ; %estimated system damping kg/s
  g = 9.80665; % acceleration due to gravity, m/s^2

% Permanent magnet (type NdFeB 30)
  Hc = 8.4e+05; % permanent magnet coercive force, A/m
  lm = 0.1*.0254; % permanent magnet length, m
  Br = 1.1; % permanent magnet residual induction, T
  Am = 1.95*0.5*0.0254^2; % permanent magnet area, m^2
  Hclm = Hc*lm; % permanent magnet mmf, A
  Rm = Hclm/Br/Am; % permanent magnet reluctance, A/wb

% Pole reluctance calculated per Ward [1977] gap of 'y' in.
  [Rmax, Rmin] = rmaxmin (y, np, lambda, l);  % A/wb
  delR = Rmax - Rmin;

% Set initial conditions
    t0 = 0;
    xcom0 = 0.0*0.0254; % initial command displacement
    x0 = xcom0; % initial displacement, m
    p0 = 0; % initial momentum, kg*m/sec
```

```
Iamp = 2.7 % amplitude of phase currents, Amps
Ns = 125 % For stepping drive, number of ministeps/cardinal state

Vmax = 0.05 % Max velocity command, m/s (reminder: Vmax will be limited
% by accel force which is a function of tf, m and the accel profile)
Vincr = 0.05 % Velocity increment, m/s
Nv = ceil(Vmax/Vincr); % Number of runs to make
Fmax = -0 % Initial external force, N
Fslip = zeros(Nv,2); % pre-allocate memory for results

checkstate = 0; % set to 1 to see state ordering
if checkstate ==1, 'checkstate',
   [sizes X0 str] = motsinfn % call function parameters.
   return
end

% Simulation loop
it = 1;  % Initialize increment
while it <= Nv,
    % Simulation adapts to results (slip force)
    Vcom = Vincr*it; % Velocity command for this increment
    tf = 12*lambda/Vcom;  % Simulation stop time, seconds

    % Inputs: Vcom-Velocity command, m/s
    %         Fx-External force, N (negative = resistance)
    % Ramp up external force at each increment of velocity.
    % Acceleration profile defined:
      ta = tf/10; % accel time before force is applied
      ut = [0 0 0; ta Vcom 0; tf Vcom Fx]; % Input matrix
            % [time velocity force]

    options = [1e-3 tf/10000 tf/500 0 0 2]; % simulation parameters
            % [error control, min step, max step,...]

    % Call to Simulink model, motsfun (step drive)
      [t,X,Y] = rk45('motsfun', [t0 tf], [], options, ut);
    % Output Y(:,1) goes to 1 when the motor slips by lambda/2.
    % Output Y(:,2) is the flux in pole 4.
    % Output Y(:,3) is the derivative of the flux in pole 4 (winding B)

    % This logic determines when slip occurs and at what applied force.
    % If slip does not occur, then the increment is repeated with higher
    % force.
    km = min(find(t>ta)); % index where force is applied.
    if max(Y(km:length(Y),1)) == 1, % If slip is found after ta
       i = min(find(Y(km:length(Y),1)))+km-1; % index where slip occurs
       tslip = t(i); % time when slip occurs
       Fslip(it,:) = table1(ut, tslip); % looks up [Vcom Fslip] pair
       Fmax = Fslip(it,2) - 20; % gets Fmax close to Fslip
       it = it + 1
    else
       Fmax = Fmax - 20; % Try more force to get slip
    end
end
```

C.2 Simple motor with non-ideal drive simulation script (emotl20.m)

```
% emotl20 is a Matlab program to simulate the motion of the L20 linear
% stepper motor, neglecting the air bearing, with a voltage input.
% X is the state vector containing momentum p,
% position x, fluxes [phi1 phi4] and xcom, the commanded position
% (integral of the velocity command)
% (other states are generated by the transfer function of the power amp)
% This program will generate the data required for the "pull-out" curve.
% The pull-out data will be in matrix Fslip.
% See below for ordering of states
clear, format compact

% This section establishes the initial conditions,
% the physical constants and L20 motor parameters

  lambda = .040*.0254; % tooth pitch, m
  y = 0.0005*0.0254; % airgap at pole, m
  np = 6; % number of teeth/pole
  l = 1.965*0.0254; % length of motor, m
  N = 58; % number of turns on coils
  Rc = 2;% coil resistance, ohms

  mf = 0.3; % approximate mass of single forcer, kg
  mp = 0; % mass of payload, kg
  m = mf + mp  % moving system mass, kg
  r = 66.5; %estimated system damping kg/s
  g = 9.80665; % acceleration due to gravity, m/s^2

% Permanent magnet (type NdFeB 30)
  Hc = 8.4e+05; % permanent magnet coercive force, A/m
  lm = 0.1*.0254; % permanent magnet length, m
  Br = 1.1; % permanent magnet residual induction, T
  Am = 1.95*0.5*0.0254^2; % permanent magnet area, m^2
  Hclm = Hc*lm; % permanent magnet mmf, A
  Rm = Hclm/Br/Am; % permanent magnet reluctance, A/wb

% Pole reluctance calculated per Ward [1977] gap of 'y' in.
  [Rmax, Rmin] = rmaxmin (y, np, lambda, l);  % A/wb
  delR = Rmax - Rmin;

% Need to calculate the initial fluxes at x0, with no power applied
% First, calculate reluctances at x0, then fluxes.

  x0 = 0.0*0.0254; % initial displacement, m
  radang = 2*pi*x0/p; % angular position, radians
  a = cos(radang); b = sin(radang); % quadrature components
  R10 = Rmax/2*(1-a)+Rmin/2*(1+a); % Reluctance at pole 1
  R20 = Rmax/2*(1+a)+Rmin/2*(1-a);
  R30 = Rmax/2*(1-b)+Rmin/2*(1+b);
  R40 = Rmax/2*(1+b)+Rmin/2*(1-b);
  Rgap = 1/(1/R10+1/R20)+1/(1/R30+1/R40); % total gap reluctance, as
    % seen by the permanent magnet.
  phi10 = Br*Am/((1+Rgap/Rm)*(1+R10/R20)); % initial flux in coil A
  phi40 = Br*Am/((1+Rgap/Rm)*(1+R40/R30)); % initial flux in coil B
```

```
% Set initial conditions:
  % initial fluxes from above
  % x0 is set above
  t0 = 0; % initial time
  pm0 = 0; % initial momentum, kg*m/sec
  xcom0 = 0.0*0.0254; % initial command displacement

Iamp = 2.7 % commanded amplitude of phase currents, Amps
ka = 100 % amplifier gain constant
Ns = 1 % For stepping drive,
       % number of ministeps/card. position (lambda/4)
Vmax = 0.2 % Max velocity command, m/s
Vincr = 0.2 % Velocity increment, m/s
Nv = ceil(Vmax/Vincr); % Number of runs to make
Fmax = -370 % Initial external force, N
            %(must be negative to oppose +x motion)
Fslip = zeros(Nv,2); % pre-allocate memory for results

checkstate = 0; % set to 1 to see state ordering
  if checkstate == 1, disp('checkstate'),
     [sizes, X0, str] = emotsin % call function parameters.
     return
  end

it = 1; % Initialize increment
while it <= Nv,
    clear t X Y % remove previous results to conserve memory
    % Simulation adapts to results (slip force)
    Vcom = Vincr*it; % Velocity command for this increment
    tf = 1.2*p/Vcom  % Simulation time, seconds

    % Inputs: Vcom-Velocity command, m/s
    %         Fx-External force, N (neg. is resistance)
    % Ramp up external force at each increment of velocity
      ta = Vcom/50; % time at which force is applied
      ut = [0 0 0; ta Vcom 0; tf Vcom Fmax;];  % [t Vcom Fx]

    options = [1e-3 tf/10000 tf/1500 0 0 2]; % simulation parameters

    % Call to Simulink model, emotstep (step drive)
    [t,X,Y] = rk45('emotstep', [t0 tf], [], options, ut);
    % Output Y(:,1) goes to 1 when the motor slips by lambda/2.
    % This logic determines when slip occurs and at what applied force.
    % If no slip, the increment is repeated with higher force.
    km = min(find(t>ta)); % index where force is applied.
    if max(Y(km:length(Y),1)) == 1,
       i = min(find(Y(km:length(Y),1)))+km-1; % index where slip occurs
       tslip = t(i); % time when slip occurs
       Fslip(it,:) = table1(ut, tslip); % looks up [Vcom Fslip] pair
       Fmax = Fslip(it,2)-2.0; % gets Fmax closer to Fslip
       it = it + 1
    else
       Fmax = Fmax - 5.0; % Try more force to get slip
    end
end
```

Appendix D

Estimate of damping coefficient

Some estimate of motor damping was required to run the simple motor simulations which do not model losses, and thus would otherwise be undamped. The L20 motor was set up without power and the forcer was accelerated along the platen by a constant force. The force was applied by hanging a fixed mass from a cord attached to the forcer through a low-friction pulley. The mass was released and the time required to move a fixed distance was measured. This time measurement was used to roughly calculate a damping coefficient. (During this test it was noted that there was some friction due to intermittent contact between the forcer and the platen. Therefore, it should be assumed that these measurements constitute an upper limit on the actually damping present.)

It was observed that the unpowered motor rapidly accelerates to the point where the velocity is constant. Under these conditions the force of the weight w pulling the motor must equal the drag coefficient times the velocity (assuming purely viscous drag)

$$w = r\frac{dx}{dt}.$$

Using this relation, the viscous drag coefficient r (kg/s) can be roughly calculated from the time t (seconds) and distance traversed d (meters) with a given weight w (lbf)

$$r = \frac{4.448w}{d}t.$$

A typical measurement with w=0.25 lbf, d=0.5 m, and t=11.5 s yields a result of r=66.5 kg/s. The measurements were quite repeatable as different accelerating masses were used or different loads were placed on the forcer.

Appendix E

MATLAB® listings (magnetic loss models)

E.1 Eddy current parameter calculation function (lerea.m)

```
function [C1,C2,K2] = lerea(f,rho,mur,d)
% function [C1,C2,K2] = lerea(f,rho,mur,d) calculates
% the intensive eddy current effective inductance and
% resistance factors C1 and C2 respectively, and
% the flux concentration factor K2.
% Reference equations 4.1, 4.4, 4.9, 4.10, 4.17
mu0 = 4*pi*1e-7;
mu = mu0*mur;
de = sqrt(rho/(pi*f*mu)); % skin depth, m
K1 = ((sinh(d/de)-sin(d/de))/(cosh(d/de)+cos(d/de)));
K2 = (d/de/2)*coth(d/de/2);
theta = asin(K1*K2*de/d); % phase angle between mmf and flux
C1 = (K2*cos(theta)-1)/(K2*K2-2*K2*cos(theta)+1);
C2 = K2*sin(theta)/(K2*K2-2*K2*cos(theta)+1);
```

E.2 Ferromagnetic element simulation parameters

E.2.1 Trafoperm material 0.3 mm thick (N2data.m)

```
% Script contains the simulation parameters for grain-oriented
% Trafoperm N2 electrical steel 0.30 mm thickness.  Note that
% other thicknesses will have similar, but perhaps not identical
% parameters.

mi = 7;  %Material index.

% Anhysteretic magnetic response (B vs H without hysteresis)
% Do not simulate a "hard" saturation (zero slope)
% Estimated from manufacturers hysteresis loop data:
HB=[
-115   -1.65
-56   -1.60
-32.5  -1.55
-22   -1.50
-16.5  -1.45
-12.3  -1.40
-8.5   -1.3
```

```
-6      -1.2
-4.5    -1.1
-3      -0.9
-2.5    -0.7
 0       0
 2.5   0.7
 3       0.9
 4.5   1.1
 6       1.2
 8.5   1.3
 12.3    1.40
 16.5    1.45
 22     1.50
 32.5    1.55
 56     1.60
 115   1.65];

eval(['HBan' int2str(mi) '=HB;']); % measured anhysteretic response

      rho = 400e-9; % resistivity, ohm-m (from literature)
      gamma(mi) = 7650; % density, kg/m3 (from literature)

% b, k and kf are selected to match the static hysteresis loops.
% Minor loops (low B amplitude) are most sensitive to b.
      b = 0.03; % hysteresis constant(ref Br)
      kf = 3.41; %loop widening as a function of Bmax parameter.
      k = 3.05; % hysteresis constant. ref Hc/(1+Bsat*kf)

% mur is a permeability which is used to calculate the eddy
% current modeling parameters.  This factor should be adjusted
% such that the simulated eddy current loss is close to the
% actual (core loss) - (hysteresis loss), and the shape of the loop
% is similar to test data.  For many materials, the classical eddy
% current calculation results are close to the actual results within
% a scale factor, so that this parameter has little effect on the
% simulated power loss.
% For best results, match data in the frequency range of interest.
      mur = 4000; % assumed constant relative permeability

% ke is selected to match high frequency core loss
% It accounts for deviation from classical eddy current loss
% prediction.  Its choice is not critical if the skin depth approaches
% the material thickness.  (i.e. low frequency, thin laminations)
      ke = 1.3; % anomalous loss factor, typically 1.0 to 2.0

mag_prop(mi,:) = [k, b, rho, mur, ke, kf];
clear HB mi k b rho mur ke kf
```

E.2.2 Trafoperm material 0.1 mm thick (N2dat1.m)

```
% Script contains the simulation parameters for grain-oriented
% Trafoperm N2 electrical steel 0.10 mm thickness.  Note that
% other thicknesses will have similar, but perhaps not identical
% parameters.
mi = 8;  %Material index.
```

```
% Anhysteretic magnetic response (B vs H without hysteresis)
% Do not simulate a "hard" saturation (zero slope)
% Estimated from manufacturers hysteresis loop data:
HB=[
-115   -1.65
-56    -1.60
-32.5  -1.55
-22    -1.50
-16.5  -1.45
-12.3  -1.40
-8.5   -1.3
-6     -1.2
-4.5   -1.1
-3     -0.9
-2.5   -0.7
 0      0
 2.5  0.7
 3      0.9
 4.5  1.1
 6      1.2
 8.5  1.3
 12.3   1.40
 16.5   1.45
 22    1.50
 32.5   1.55
 56    1.60
 115  1.65];

eval(['HBan' int2str(mi) '=HB;']); % measured anhysteretic response

      rho = 400e-9; % resistivity, ohm-m (from literature)
      gamma(mi) = 7650; % density, kg/m3 (from literature)

% b, k and kf are selected to match the static hysteresis loops.
% Minor loops (low B amplitude) are most sensitive to b.
      b = 0.03; % hysteresis constant(ref Br)
      kf = 4.4; %loop widening as a function of Bmax parameter.
      k = 4.0; % hysteresis constant. ref Hc/(1+Bsat*kf)

% mur is a permeability which is used to calculate the eddy
% current modeling parameters.  This factor should be adjusted
% such that the simulated eddy current loss is close to the
% actual (core loss) - (hysteresis loss), and the shape of the loop
% is similar to test data.  For many materials, the classical eddy
% current calculation results are close to the actual results within
% a scale factor, so that this parameter has little effect on the
% simulated power loss.
% For best results, match data in the frequency range of interest.
      mur = 4000; % assumed constant relative permeability

% ke is selected to match high frequency core loss
% It accounts for deviation from classical eddy current loss
% prediction.  Its choice is not critical if the skin depth approaches
% the material thickness.  (i.e. low frequency, thin laminations)
      ke = 1.5; % anomalous loss factor, typically 1.0 to 2.0

mag_prop(mi,:) = [k, b, rho, mur, ke, kf];
```

```
clear HB mi k b rho mur ke kf
```

E.2.2 Hot rolled, low carbon steel, type AISI 1018 (S1018dat.m)

```
% Script contains the material constants and simulation parameters
% for bar form 1018 Hot rolled steel.

mi = 1; % Material index

% Intrinsic anhysteretic magnetic response (Bi vs H without hysteresis)
% Calculated from measured data on L20 motor platen specimen:
HJneg = 1.0e+04 *[
  -2.50  -0.000200
  -2.31  -0.000199
  -2.032 -0.000196
  -1.79  -0.000192
  -1.57  -0.000189
  -1.38  -0.000186
  -1.21  -0.000182
  -1.07  -0.000178
  -0.938  -0.000175
  -0.824  -0.000172
  -0.724  -0.000168
  -0.637  -0.000165
  -0.560  -0.000162
  -0.492  -0.000159
  -0.433  -0.000156
  -0.380  -0.000153
  -0.334  -0.000150
  -0.294  -0.000147
  -0.258  -0.000145
  -0.227  -0.000142
  -0.200  -0.000139
  -0.151  -0.000128
  -0.114  -0.000116
  -0.0865 -0.000105
  -0.0654 -0.000095
  -0.0495 -0.000084
  -0.0375 -0.000073
  -0.0284 -0.000062
  -0.0216 -0.000051
  -0.0162 -0.000042
  -0.0123 -0.000033
  -0.0093 -0.000026
  -0.0070 -0.000021
  -0.0053 -0.000016
  -0.0040 -0.000012
  -0.0030 -0.000009
  -0.0023 -0.000007
  -0.0017 -0.0000055
  -0.0013 -0.000004
  -0.0010 -0.000003];

Han = [HJneg(:,1);-flipud(HJneg(:,1))];
Jan = [HJneg(:,2);-flipud(HJneg(:,2))];
```

```
Ban = Jan + 4*pi*1e-7*Han; % Calculate normal induction

HB  = [Han Ban];

eval(['HBan' int2str(mi) '=HB;']); % measured anhysteretic response

      rho = 130e-9; % resistivity, Ω-m (from literature)
      gamma(mi) = 7860; % density, kg/m3 (from literature)

% b, k and kf are selected to match the static hysteresis loop.
% Minor loops (low B amplitude) are most sensitive to b.
      b  = 0.1; % hysteresis constant
      kf = 8.4; %loop widening as a function of Bmax.
      k  = 46.3; % hysteresis constant. ref Hc/(1+Bsat*kf)

% mur is a permeability which is used to calculate the eddy
% current modeling parameters.  This factor should be adjusted
% such that the simulated eddy current loss is close to the
% actual (core loss) - (hysteresis loss), and the shape of the loop
% is similar to test data.  For many materials, the classical eddy
% current calculation results are close to the actual results within
% a scale factor, so that this parameter has little effect on the
% simulated power loss.
% For best results, match data in the frequency range of interest.
      mur = 400; % assumed constant relative permeability

% ke is selected to match high frequency core loss
% It accounts for deviation from classical eddy current loss
% prediction.  Its choice is not critical if the skin depth approaches
% the material thickness.  (i.e. low frequency, thin laminations)
      ke = 1.5; % guess anomalous loss factor (typically 1-2)

mag_prop(mi,:) = [k, b, rho, mur, ke, kf];

clear BH Han Ban Jan HB mi k b rho mur ke kf HJneg
```

E.3 Simulation script for the motor model with ferromagnetic platen losses included (rmrun4.m)

```
% rmrun4 is a Matlab program to simulate the motion of the L20 linear
% stepper motor, neglecting the air bearing, with a voltage input.
% The called simulation routine includes iron losses in the platen.
% The simulation will not be valid for extremely low frequency.
% X is the state vector of momentum p, position x, fluxes [Ø1 Ø4]
% and xcom, the commanded position (integral of the velocity command)
% Other states are generated by the transfer function of the power amp,
% the hysteresis and eddy current models.
clear, format compact

t0 = 0;

% This section establishes the initial conditions,
% the physical constants and L20 motor parameters

  lambda = .040*.0254; % tooth pitch, m
  y = 0.0005*0.0254; % airgap at pole, m
```

```
  np = 6; % number of teeth/pole
  l = 1.965*0.0254; % length of motor across the axis of motion, m
  N = 58; % number of turns on coils
  rc = 2;% coil resistance, ohms

  mf = 0.45; % approximate mass of single forcer w/cable, kg
  mpl = 0; % mass of payload, kg
  m = mf + mpl;  % moving system mass, kg
  r = .1; % negligible system mechanical damping kg/s
  g = 9.80665; % acceleration due to gravity, m/s^2

% Permanent magnet (type NdFeB 30)
  Hc = 8.4e+05; % permanent magnet coercive force, A/m
  lm = 0.1*.0254; % permanent magnet length, m
  Br = 1.1; % permanent magnet residual induction, T
  Am = 1.95*0.5*0.0254^2; % permanent magnet area, m^2
  Hclm = Hc*lm; % permanent magnet mmf, A
  Rm = Hclm/Br/Am; % permanent magnet reluctance, A/wb

% Airgap reluctance calculated per Ward [1977] gap of 'y'.
  [Rmax, Rmin] = rmaxmin (y, np, lambda, l);  % A/wb
  delR = Rmax - Rmin;

% Loss parameters of modeled ferromagnetic elements

  % Call to appropriate material data script(s)

      S1018dat

  % Platen:
  % The platen is a relatively thick material and should be modeled
  % to include the sides to account for the fact that flux will be
  % carried on all four outside surfaces.  At high frequency, where
  % thickness > 6*(skin thickness), the effective flux carrying area is
  % approximately independent of the actual thickness and depends on the
  % surface area only.
  % This model is adjusted by adding the thickness of the platen to
  % the width.  The area, and the effect of corners are compensated
  % by reducing the thickness proportionately.
      lp = 0.24*0.0254; % mean magnetic path length between poles, m
      w  = 1.96*0.0254; % platen physical width, m
      d  = 0.718*0.0254; % platen physical thickness, m
      wp = w + d; % effective platen width, m
      dp = w*d/wp; % effective platen thickness, m
      Ap = dp*wp; % Static flux carrying area, m^2
      mp = 1; % material identifier code

% The initial fluxes at x0 are not directly calculable, thus initial
% conditions are set to zero with no current and permanent magnet
% strength set to zero.  Then the permanent magnet strength is
% 'ramped up' to its steady state value, Hclm.  At this point the
% current is applied and the simulation begins.

% Set initial conditions:
  p0 = 0; % initial momentum, kg*m/sec
  xcom0 = 0.0; % initial command displacement
  x0 = 0; % initial displacement, m
```

```
Iamp = 2.7 % commanded amplitude of phase currents, Amps
ka = 20 % amplifier gain constant
Vmax = 1.016 % Max velocity command, m/s
Vincr = 1.016 % Velocity increment, m/s
Nv = ceil(Vmax/Vincr); % Number of runs to make
Fmax = -25 % Initial external force, N
          % (must be negative to oppose +x motion)
Fslip = zeros(Nv,4); % pre-allocate memory

checkstate = 0; % set to 1 to see state ordering
  if checkstate == 1, disp('checkstate'),
       f = Vmax/lambda;
       [sizes, X0, str] = rmstep4 % call function parameters.
       return
  end

it = 1;
while it <= Nv,
      clear t X Y
      % Simulation adapts to results (slip force)
      Vcom = Vincr*it; % Velocity command for this increment, m/s
      f = Vcom/lambda; % nominal frequency for this increment, hz

      % Inputs: Vcom-Velocity command, m/s
      %            Fx-External force, N (neg. is resistance)
      %            Hclm-Permanent Magnet mmf, A
      %            Iamp-Amplitude of phase current, A
      % Ramp up velocity, external force, magnet, and current:
        tz = 0.01 % time at which acceleration begins, sec
        ta = m*Vcom/20 % accel time (limits accel force to 20N), sec
        td = 5*lambda/Vcom % dwell time at Vcom (5 cycles), sec
        tr = 20*lambda/Vcom % ramp to apply force Fmax (20 cycles), sec
        tf = tz + ta + td + tr % total simulation time, sec
      % Input table: [t Vcom Fx Hclm Iamp]:
        ut = [0 0 0 0 0; tz 0 0 Hclm Iamp; ta+tz Vcom 0 Hclm Iamp;
                  ta+tz+td Vcom 0 Hclm Iamp; tf Vcom 0 Hclm Iamp];

      % simulink integrator parameters
      options(1) = 1e-2;  % error tolerance
      options(2) = 0.01/f; % min step, sec
      options(3) = 0.1/f; % max step, sec
      options(4) = 0;
      options(5) = 0;
      options(6) = 2;

      % Call to Simulink model, using 'gear' integration
      [t,X,Y] = gear('rmstep4', [t0 tf], [], options, ut);
      % Output Y(:,1) goes to 1 when the motor slips by lambda/2.

      km = min(find(t>ta)); % index where force is applied.
      if max(Y(km:length(Y),1)) == 1,
         i = min(find(Y(km:length(Y),1)))+km-1; % index at motor slip
         tslip = t(i); % time when slip occurs
         Fslip(it,:) = table1(ut, tslip); % looks up [Vcom Fslip] pair
         Fmax = Fslip(it,2)-2.0 % gets Fmax closer to Fslip
         it = it + 1
```

```
      else
         Fmax = Fmax - 10.0; % Try more force to get slip
         it = it +1  % advances the loop when not looking for slip.
      end
end
```

E.4 Power calculation algorithm

```
function [P] = power(e, q, t, ni, nf)
% function "power" calculates the cycle average power expended
% by effort e over displacement q in time interval t(ni,nf).
% The "power" function calculates the incremental energy
% ΔE=eΔq over each data interval t(k-1) to t(k+1).
% The sum of all such elements is twice the total energy.
% The average power is then one-half the total energy divided
% by the total time.

% ni-1 and nf+1 elements must exist in the e and q variables.
E2 = 0;
for k = ni : nf,
    E2 = E2 + e(k)*(q(k+1)-q(k-1));
end

P = E2/2/(t(nf)-t(ni));
```

E.5 Simulation script for the motor model with eddy current platen losses included (rmrun7.m)

```
% rmrun7 is a Matlab program to simulate the motion of the L20 linear
% stepper motor, neglecting the air bearing, with a voltage input.
% Velocity feedback can been added for damping (rmstep7.m)
% The called simulation routine includes eddy losses in the platen.
% **Hysteresis is not included**
% The simulation will not be valid for extremely low frequency.
% X is the state vector containing momentum p, position x,
% fluxes [phi1 phi4]
% and xcom, the commanded position (integral of the velocity command)
% There are also states generated by the transfer function
% of the power amp and the eddy current system.
clear, format compact

t0 = 0;

% This section establishes the initial conditions,
% the physical constants and L20 motor parameters

  lambda = .040*.0254; % tooth pitch, m
  y = 0.0005*0.0254; % airgap at pole, m
  np = 6; % number of teeth/pole
  l = 1.965*0.0254; % length of motor across the axis of motion, m
  N = 58; % number of turns on coils
  rc = 2;% coil resistance, ohms

  mf = 0.45; % approximate mass of single forcer w/cable, kg
  mpl = 0 % mass of payload, kg
```

```
  m = mf + mpl;  % moving system mass, kg
  r = 0.1; % negligible system mechanical damping kg/s
  g = 9.80665; % acceleration due to gravity, m/s^2

% Permanent magnet (type NdFeB 30)
  Hc = 8.4e+05; % permanent magnet coercive force, A/m
  lm = 0.1*.0254; % permanent magnet length, m
  Br = 1.1; % permanent magnet residual induction, T
  Am = 1.95*0.5*0.0254^2; % permanent magnet area, m^2
  Hclm = Hc*lm; % permanent magnet mmf, A
  Rm = Hclm/Br/Am; % permanent magnet reluctance, A/wb

% Airgap reluctance calculated per Ward [1977] gap of 'y'.
  [Rmax, Rmin] = rmaxmin (y, np, lambda, l);  % A/wb
  delR = Rmax - Rmin;

% Loss parameters of modeled ferromagnetic elements

  % Call to appropriate material data scripts

      S1018dat

  % Platen:
  % The platen is a relatively thick material and should be modeled
  % to include the sides to account for the fact that flux will be
  % carried on all four outside surfaces.  At high frequency,
  % where thickness > 4*(skin thickness),
  % the effective flux carrying area is
  % approximately independent of the actual thickness and depends on the
  % surface area only.
  % This model is adjusted by adding the thickness of the platen to
  % the width.  The area, and the effect of corners are compensated
  % by reducing the thickness proportionately.
      lp = 0.24*0.0254; % mean magnetic path length between poles, m
      w  = 1.96*0.0254; % platen physical width, m
      d  = .718*0.0254; % platen physical thickness, m
      wp = w + d; % effective platen width, m
      dp = w*d/wp; % effective platen thickness, m
      Ap = dp*wp; % Static flux carrying area, m^2
      mp = 1; % material identifier code

% The initial fluxes at x0 are not directly calculable, thus initial
% conditions are set to zero with no current and permanent magnet
% strength set to zero.  Then the permanent magnet strength is
% 'ramped up' to its steady state value, Hclm.  At this point the
% current is applied and the simulation begins.

% Set initial conditions:
  p0 = 0; % initial momentum, kg*m/sec
  xcom0 = 0; % initial command displacement
  x0 = 0.0; % initial displacement, m

Iamp = 2.7; % commanded amplitude of phase currents, Amps
ka = 20; % amplifier gain constant
Kv = 0.002 % velocity feedback gain
Vmax = 1.8 % Max velocity command, m/s
Vincr = .05 % Velocity increment, m/s
```

```
Nv = ceil(Vmax/Vincr); % Number of runs to make
Fmax = -0 % Initial external force, N
          % (must be negative to oppose +x motion)
Fslip = zeros(Nv,4); % pre-allocate memory

it = 1;
while it <= Nv,
      clear t Y
      % Simulation adapts to results (slip force)
      Vcom = Vincr*it; % Velocity command for this increment, m/s
      f = Vcom/lambda; % nominal frequency for this increment, hz

      % Inputs: Vcom-Velocity command, m/s
      %            Fx-External force, N (neg. is resistance)
      %            Hclm-Permanent Magnet mmf, A
      %            Iamp-Amplitude of phase current, A
      % Ramp up velocity, external force, magnet, and current:
        tz = 0.01; % time at which acceleration begins, sec
        ta = m*Vcom/20; % accel time (limits accel force to 20N), sec
        td = 5*lambda/Vcom; % dwell time at Vcom (5 cycles), sec
        tr = 40*lambda/Vcom; % ramp time to apply force Fmax
                             %(40 cycles), sec
        tf = tz + ta + td + tr; % total simulation time, sec
        ut = [0 0 0 0 0; tz 0 0 Hclm Iamp; ta+tz Vcom 0 Hclm Iamp;
                  ta+tz+td Vcom 0 Hclm Iamp; tf Vcom Fmax Hclm Iamp];
                  % [t Vcom Fx Hclm Iamp]

  options(1) = 1e-3;  % error tolerance
  options(2) = 0.005/f; % min step
  options(3) = 0.025/f; % max step
  options(4) = 0;
  options(5) = 0;
  options(6) = 2;

      % Call to Simulink model, rmstep7
      % (velocity feedback, no hysteresis) or
      % rmstep5 (no hysteresis, no velocity feedback)
      % rk45 integrator best accuracy, reasonable speed.
      % linsim integrator can be very fast, but may become unstable.
      [t,X,Y] = rk45('rmstep7', [t0 tf], [], options, ut);
      clear X
      % Output Y(:,1) goes to 1 when the motor slips by lambda/2.

      km = min(find(t>ta+tz+td)); % index where force is applied.
      if max(Y(km:length(Y),1)) == 1,
         i = min(find(Y(km:length(Y),1)))+km-1;
            % index where slip occurs
         tslip = t(i); % time when slip occurs
         Fslip(it,:) = table1(ut, tslip); % looks up [Vcom Fslip] pair
         Fslip(it,2)
         Fmax = Fslip(it,2)-2.0; % gets Fmax closer to Fslip
         it = it + 1
      else
         Fmax = Fmax - 20.0; % Try more force to get slip
         it = it +1  % advances the loop when not looking for slip.
      end
end
```

Appendix F

Spreadsheet analysis of magnetic losses.

An estimate of magnetic losses is desirable to help identify those aspects of the system which may be negligible and therefore omitted from the system model and simulation. A spreadsheet calculation (shown below) was performed for the major elements of the modeled Sawyer motor.

Line by line discussion of spreadsheet entries:

laminations:	The number of laminations n in the physical structure. The platen is a solid piece of steel. The platen teeth are considered "laminated" by virtue of there being 6 per pole. The forcer is a stack of 145 laminations.
thickness:	Refers to the thinnest dimension across the flux path, per lamination. (Refer to dimension d in Figure 3.5)
width:	Refers to the dimension perpendicular to thickness. (Refer to dimension w in Figure 3.5)
physical area:	The flux path cross section area, defined as $A=ndw$.
resistivity:	Material resistivity, ρ. From tabulated sources (see Appendix G)
relative permeability:	Roughly estimated for typical operating flux density. Principal value of this estimate is to establish that the forcer has about ten times the relative permeability of the platen.
Characteristic frequency:	Refer to equation 3.1. Defined as the frequency where $3\delta=d/2$. The intent is to determine at approximately what frequency the classical eddy current assumption of uniform flux penetration loses validity.

skin depth:	Calculated from equation 3.1.
Effective flux section area:	The flux path cross section area, calculated as $A_e=ndw$ or $A_e=n6\delta w$, whichever is less. Compenstates for flux concentration due to skin effect.
flux path length:	Refers to the dimension in the direction magnetic flux; l in Figure 3.5.
flux with min area at 1.4 T	Calculated value, assuming that maximum flux density occuring in the minimum effective flux section area of the four elements is 1.4 T. $\phi=1.4\min(A_e)$
flux density calculated over effective area	Flux density in the element. $B_m=\phi/A_e$.
MMF across element at flux density using curves	Estimated mmf across the element at flux density B_m. Calculated by looking up field strength, H corresponding to B_m on B-H curve for material. Approximated value ignoring hysteresis. mmf=Hl.
Steinmetz coeffecient	Value of η from reference [17].
Hysteresis loss (Steinmetz)	Hysteresis power loss P_h calculated from equation 4.2.
Eddy current loss (classical)	Eddy current power loss P_e calculated from equation 4.1.
Total (per pole) estimated loss	$P_{t=}P_h+P_e$.
% loss attributed to hysteresis	% total=$100P_h/P_t$.

Spreadsheet to evaluate relative loss magnitudes. Calculations are approximate per pole values.

	Nomenclature	Platen			Forcer		Units
Material		AISI 1018 steel			Silicon Steel M-43		
Function		platen structure		platen teeth	forcer pole	forcer teeth	
		Strict classical calculation	modified for skin depth				
laminations	n	1	1	6	145	145	
thickness	d	1.8E-02	1.8E-02	5.1E-04	3.4E-04	3.4E-04	m
width	w	5.0E-02	5.0E-02	5.0E-02	5.6E-03	3.0E-03	m
physical area	A	9.2E-04	9.2E-04	1.5E-04	2.8E-04	1.5E-04	m^2
resistivity	rho	1.3E-07	1.3E-07	1.3E-07	4.0E-07	4.0E-07	ohm-m
relative permeability*	mur	N/A	400	400	4000	4000	
Characteristic frequency*		N/A	8.8E+00	1.2E+04	7.8E+03	7.8E+03	Hz
skin depth	delta @ 100 Hz	N/A	9.1E-04	9.1E-04	5.0E-04	5.0E-04	m
	delta @ 1 kHz	N/A	2.9E-04	2.9E-04	1.6E-04	1.6E-04	m
Effective flux section area**	Ae @ 100 Hz	9.2E-04	2.7E-04	1.5E-04	2.8E-04	1.5E-04	m^2
	Ae @ 1kHz	9.2E-04	8.6E-05	1.5E-04	2.8E-04	1.5E-04	m^2
flux path length	l	6.1E-03	6.1E-03	5.1E-04	1.5E-02	5.1E-04	m
flux with min area at 1.4 T	phi @ 100 Hz	2.1E-04	2.1E-04	2.1E-04	2.1E-04	2.1E-04	Wb
	phi @ 1 kHz	2.1E-04	1.2E-04	1.2E-04	1.2E-04	1.2E-04	Wb
flux density calculated over	Bm @ 100 Hz	2.3E-01	7.8E-01	1.4E+00	7.6E-01	1.4E+00	T
effective area	Bm @ 1 kHz	2.3E-01	1.4E+00	7.9E-01	4.3E-01	8.0E-01	T
MMF across element at	at 100 Hz	7.1E+00	4.9E+00	1.3E+00	7.3E-01	1.2E-01	A
flux density using curves	at 1 kHz	7.1E+00	1.5E+01	4.1E-01	4.9E-01	2.4E-02	A
Steinmetz coefficient	eta	9.0E-03	9.0E-03	9.0E-03	5.0E-04	5.0E-04	
Hysteresis loss (Steinmetz)	Ph @ 100 Hz	0.121	0.251	0.030	0.034	0.002	W
	Ph @ 1 kHz	1.208	2.029	0.120	0.140	0.007	W
Eddy current loss (classical)	Pe @ 100 Hz	12.730	3.766	0.005	0.012	0.001	W
	Pe @ 1 kHz	1273.002	38.538	0.158	0.385	0.024	W
Total (per pole) estimated loss	Pt @ 100 Hz	12.851	4.017	0.034	0.046	0.002	W
	Pt @ 1 kHz	1274.210	40.567	0.278	0.525	0.030	W
% Loss attributed to hysteresis	% total @100 Hz	0.9%	6.2%	85.9%	74.3%	69.4%	
	% total @1 kHz	0.1%	5.0%	43.2%	26.6%	22.2%	

* Frequency where 3*skin depth is equal to the one-half the thickness dimension. Assumed relative permeability.
** Using minimum of (6*skin depth or thickness)

pi	3.1415927
mu0	1.25664E-06

Appendix G

Magnetic material summary

Reference tabulation of magnetic properties.

To facilitate comparison, all loss properties are calculated from published values for common geometry, unless otherwise noted.
Preference given to manufacturers data and industry specifications, where available.
Estimates from data are "e". Interpolated from published data are "i". Measured "m".

Material Name [1]	Material Specification	Density (kg/m^3)	Resistivity (ohm-m)	Curie Temp (°C)	Core Loss (W/kg)	Max. Relative Permeability	Sat Flux Density (T) @H (kA/m)	Residual Induction (T), from 1T	Coercive Force (A/m), from 1T
Laminations 0.36mm thick									
Silicon Iron (2.8% Si)	ASTM A677 [2]	7700	454E-9 i	768 i	3.97 (max,60hz,1.5T)	18000	1.7@8	0.55	5.2
Silicon Iron (3.5% Si)	ASTM A677 [2]	7650	521E-9 i	766 i	3.20 (max,60hz,1.5T)	18500e	1.7@8	–	–
Nickel-Iron (48% Ni)	ASTM A753 [7]	8250	470E-9	482	3.88 (typ,400hz,0.8T)	140000	1.5 @8	0.9	2.4
Cobalt-Iron (49% Co, 2% V)	ASTM A801 [5]	8120	400E-9	940	41.8 (typ,400hz,1.5T)	6750	2.10@.8 2.36@8	1.45	71.6
Solid material >2mm thick									
Carbon steel 0.2%C	AISI 1018 [11]	7850	130E-9	770	–	1100 m	1.65@8 m	0.6 e	400 e
Silicon Iron (1.1% Si)	ASTM A867	7750	300E-9	785	–	11250	1.45@.8 1.75@8	0.85	71.6 (max)
Silicon Iron (2.3% Si)	ASTM A867	7650	400E-9	770	–	11500	1.4@.8 1.7@8	0.86	59.7 (max)
Silicon Iron (4.0% Si)	ASTM A867	7600	580E-9	765	–	9000	1.3@.8 1.65@8	0.7	43.8 (max)
Nickel-Iron (48% Ni)	ASTM A753 [7]	8250	470E-9	482	–	120000	1.5@8	0.9	3.6
Cobalt-Iron (49% Co, 2% V)	ASTM A801	8120	400E-9	940	–	2000e [8]	2.00@.8 i [8]	1.3 i [8]	100 i [8]
Sintered Iron powder	ASTM A811 [9]	7200	137E-9 i	770e	–	4200	1.3@1.2	1.1	120
Phosphorous-Iron powder	ASTM A 839 [6]	7280	230e-9 i	770e	–	4640	1.3@1.2	1.2	112
MnZn Ferrite	3C80[10]	4800	100E-2	210	3.1 (typ,1000hz,0.3T)	5000	0.4@1.2		6.3

Notes: numbers in brackets []

Properties are typical, unless otherwise specified.

1. Nominal Composition
2. Silicon-Iron laminations are non-oriented, fully processed (heat treated).
5. Alloy 1, heat treated 845C
6. 0.80% Phosphorous, sintered at 685MPa
7. Alloy 2, Grade B
8. Thick material properties vary due to use of bar tests rather than ring tests. Assumed product form is thick strip. Properties interpolated.
9. Grade 1 material sintered to 7.2 g/cc. (high temperature/high pressure process)
10. Philips/Ferroxcube MnZn-Ferrite
11. Test ring cut from motor platen (1018 hot rolled steel)
12. The Earth's magnetic field: ~56 A/m

Appendix H

Magnetic test data (AISI 1018 steel).

In order to provide a basis for setting the modeling parameters for the platen, magnetic hysteresis test data was required. Since this data was unavailable, a sample of steel was cut from the L20 platen and subjected to laboratory tests in accordance with ASTM practice [2].

H.1 Test specimen

The test part was machined to a toroidal shape with a rectangular cross section. The following dimensions (inches) were obtained:

Inside diameter (ID):	1.5840
Outside diameter (OD):	1.8935
Width:	0.2645

Two coils were wound on the toroid, evenly spaced around the circumference. The "B" coil (inner winding) was 191 turns of #29 AWG magnet wire. The "H" coil (outer winding)was 323 turns of #22 AWG copper wire.

H.2 Test setup

The recommended approach [2, 3] to magnetic testing is to apply controlled current to the "H" winding. This will establish a controlled mmf in the toroid. The magnetic response is determined by measuring the open circuit voltage at the "B" coil. The voltage is integrated to determine the flux in the toroid. If the "H" coil current is changed very slowly, there will be no significant effect of inductance on the circuit, and eddy currents will be negligible.

A block diagram showing the equipment used is shown in Figure H.1.

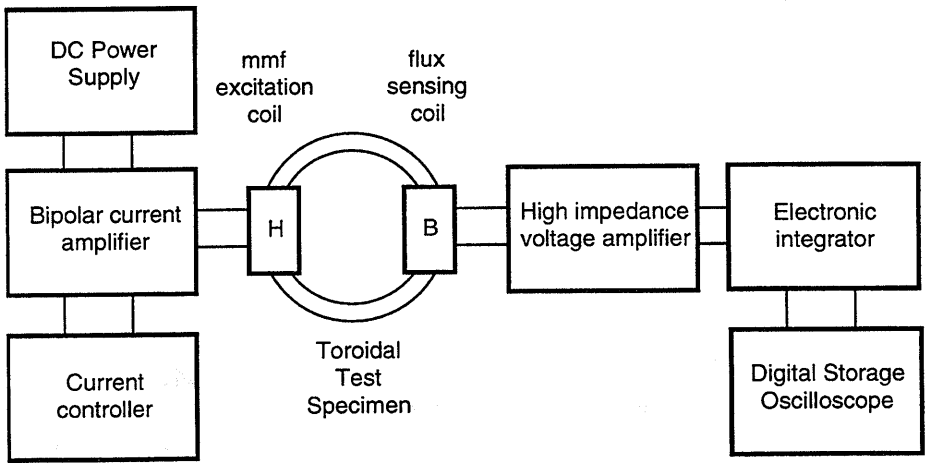

Figure H.1. Magnetic specimen test diagram.

H.3 Test procedures

Three types of data were obtained by the following general procedures. Detailed guidance was taken from [2, 3]

H.3.1 Initial magnetization curve

The initial magnetization curve is a plot of flux versus mmf that results when an demagnetized specimen is subjected to a steadily increasing mmf. The specimen is first demagnetized by applying an alternating mmf which starts at a high amplitude and is very slowly reduced to a zero amplitude. At this condition the output of the integrator is zeroed. Then a current is applied to the mmf coil and slowly increased. Integrator output and current input are stored in the oscilloscope.

H.3.2 Hysteresis loops

The procedure for obtaining the hysteresis loops begins with the procedure for the initial magnetization curve. After attaining the desired maximum value, the current to the mmf coil is then decreased to the desired level (which may be negative), then increased again. This ramping up and down of the current (accomplished manually or with a triangle wave generator) is repeated to the same limits until a repeatable loop is obtained. Again, the current is changed very slowly. Care must be taken to assure that integrator drift does not add a significant error to the result. The process of demagnetization need not be repeated if the hysteresis loop is repeated to a known state of magnetization.

H.3.3 Anhysteretic data

The procedure for obtaining the anhysteretic data is the same as demagnetization, except that the alternating mmf is applied to cycle around the desired mmf input point, instead of zero. For example, to obtain the anhysteretic flux for an mmf of X, the mmf is cycled between $X+A$ and $X-A$ and back, where amplitude A is initially great enough to magnetically saturate the specimen on both positive and negative excursions. Amplitude A is then slowly decreased, while continuing to cycle around X until $A=0$. The resulting flux measurement is the anhysteretic data point. The more slowly the amplitude is decreased relative to the number of cycles, the more accurate the measurement. Of course, effects such as integrator drift may interfere with achieving very high accuracy.

H.4 Calculations

Given a set of voltage readings at the output of the integrator, and current readings from the input winding calculations must be done to extract the results in terms of magnetic units.

Calculation of the imposed field strength is accomplished by determining the mmf per unit length of toroid. The equation to calculate the field strength, H given "H" coil current i is

$$H = \frac{Ni}{l},$$

where N is the number of turns on the coil, and l is the mean flux path length computed from the mean diameter

$$l \cong \pi \frac{ID + OD}{2}.$$

Calculation of the flux density from the voltage output V of the integrator begins with Faraday's law applied over the section area, A of the toroid

$$e = -N\frac{d\phi}{dt} = -NA\frac{dB}{dt}.$$

Solving for the flux density

$$B = \frac{-1}{NA}\int e \cdot dt,$$

where e is the voltage at the "B" coil. The electronic integrator integrates the voltage e according to its time constant RC,

$$V = \frac{-1}{RC}\int e \cdot dt.$$

Combining the previous two equations, the result,

$$B = \frac{RCV}{NA}$$

expresses the flux density directly from the integrator output.

H.5 Results

Results are presented in graphical form in Figures 3.10, 3.15 and 3.16

Bibliography

[1] J. Abraham. *Modeling the Sawyer Linear Stepper Motor*. Course 2.141 term project. MIT, Cambridge, MA, 1992.

[2] American Society for Testing and Materials. Section 3, Metals Test Methods and Analytical Procedures, Volume 03.04, Magnetic Properties; Materials for Thermostats, Electrical Heating and Resistance, Contacts and Connectors. *1993 Annual Book of ASTM Standards*. Philadelphia, PA, 1993.

[3] N.F. Astbury. *Industrial Magnetic Testing*. The Institute of Physics, London, UK, 1952.

[4] Richard Boll, Editor. *Soft Magnetic Materials: Fundamentals, Alloys, Properties, Products, Applications*. Heyden & Son Ltd, London, UK, 1979.

[5] M.A. Coulson, R.D. Slater, and R.R.S. Simpson. Representation of magnetic characteristic, including hysteresis, using Preisach's theory. In the *Proc IEE*, 124:895-898.

[6] J. D. Edwards. *Electrical Machines*. 2nd ed. Macmillan Publishing Co., New York, NY, 1986.

[7] Robert M. Fano, Lan Jen Chu, and Richard B. Adler. *Electromagnetic Fields, Energy, and Forces*. John Wiley and Sons, Inc., New York, NY, 1960.

[8] C.B. Gray. *Electrical Machines and Drive Systems*. Longman Scientific & Technical, New York, NY, 1989.

[9] Carl Heck, Dr-Ing. *Magnetic Materials and their Applications*. Butterworth and Co. (Publishers) Ltd, 1974.

[10] D.C. Jiles and D.L. Atherton. Theory of Ferromagnetic Hysteresis. In the *Journal of Magnetism and Magnetic Materials*, 61:48-60, 1986.

[11] David C. Jiles, and J.B. Thoelke, and M.K. Devine. Numerical Determination of Hysteresis Parameters for the Modeling of Magnetic Properties Using the Theory of Ferromagnetic Hysteresis. In the *IEEE Transactions on Magnetics*, 28:27-35, 1992.

[12] Dean C. Karnopp, Donald L. Margolis and Ronald C. Rosenberg. *System Dynamics: A Unified Approach*. 2nd ed. John Wiley and Sons, New York, NY, 1990.

[13] Dean Karnopp. Computer Models of Hysteresis in Mechanical and Magnetic Components. In the *Journal of the Franklin Institute*, 316:405-415, 1983.

[14] Takashi Kenjo. *Stepping motors and their microprocessor controls*. Oxford University Press, New York, NY, 1984.

[15] B.C. Kuo, Editor. *Step Motors and Control Systems*. SRL Publishing Co., Champaign, Ill., 1979.

[16] B.C. Kuo. *Theory and Applications of Step Motors*. West Publishing Co., St. Paul, MN, 1973.

[17] Walter A. La Pierre. Electrical Engineering. In Mark's *Standard Handbook for Mechanical Engineers*, 8th edition, T. Baumeister, ed., ch. 15, 1978.

[18] Albert C. Leenhouts. *The Art and Practice of Step Motor Control*. Intertec Communications, Ventura, CA, 1987.

[19] The MathWorks, Inc. SIMULINK® 1.3 *Release Notes*. April 1994. SIMULINK® and MATLAB® are registered trademarks of The MathWorks, Inc.

[20] I.D. Mayergoyz. *Mathematical Models of Hysteresis*. Springer Verlag, New York, NY, 1991.

[21] S.R. Naidu. Simulation of the hysteresis phenomenon using Preisach's theory. In the *IEE Proceedings-A*, 137:73-79, 1990.

[22] S.A. Nasar and L.E. Unnewehr. *Electromechanics and Electric Machines*. John Wiley and Sons, New York, NY, 1979.

[23] Hermann K.P. Neubert. *Instrument Transducers, An Introduction to their Performance and Design*, 2nd ed. Clarendon Press, Oxford, UK, 1975.

[24] Parker Hannifin Corporation. Engineering Reference and Application Solutions. In Online *Catalogs*, http://www.compumotor.com, 1996.

[25] Parker Hannifin Corporation. Packaged Systems and Components, Stepper Systems. In Online *Catalogs*, http://www.compumotor.com, 1996.

[26] F. Preisach. On magnetic after-effect. *Z. Physics,* 94, p. 277, 1935.

[27] G. Qishan, and Z. Jimin. Saturated permeance of identically, doubly-slotted magnetic structures. In *IEE Proceedings-B* 140:323-328.

[28] Simon Ramo, John R. Whinnery, and Theodore Van Duzer. *Fields and Waves in Communication Electronics* 2nd ed. John Wiley and Sons, New York, NY, 1984.

[29] Pablo Rodriguez. *Development of a Linear Motor Model for Computer Simulation.* Master's thesis. MIT, Cambridge, MA, 1993.

[30] Henning Schulze-Lauen. *Development of an Enhanced Linear Motor Drive for a High Speed Flexible Automation System.* Research project at MIT, Cambridge, MA. Diplom-Ingenieur thesis. Aachen University of Technology, Aachen, Germany, 1993.

[31] P. A. Ward and P. J. Lawrenson. Magnetic permeance of doubly-salient airgaps. In *Proc. of the IEE*, 124:542-544, 1977.

[32] F.E. Werner and R.I. Jaffee. Energy-Efficient Steels for Motor Laminations. In *Journal of Materials Engineering and Performance*, 1:227-234, 1992.

[33] K. Youcef-Toumi and P. Gjeltema, *A Preliminary Study of a Sawyer Linear Motor.* Pedigree Report No. 1. MIT, Cambridge, MA, 1992.